2Mit

FINAL REPORT

NASA Grant NGR-11-002-146

DIAGNOSTICS OF SEEDED RF PLASMAS—
AN EXPERIMENTAL STUDY RELATED TO THE GASEOUS
CORE NUCLEAR REACTOR

S. D. Thompson, J. D. Clement, and J. R. Williams

Prepared for the

National Aeronautics and Space Administration
Lewis Research Center
Cleveland, Ohio 44135

by the

School of Nuclear Engineering
Georgia Institute of Technology
Atlanta, Georgia 30332

Preceding pages blank

TABLE OF CONTENTS

TABLE OF CONTENTS (Concluded)

LIST OF TABLES

LIST OF ILLUSTRATIONS

LIST OF ILLUSTRATIONS (Continued)

LIST OF ILLUSTRATIONS (Concluded)

SUMMARY

The recent interest in radiofrequency (rf) induction heating as a
means of producing a plasma has prompted work on theoretical techniques
that can adequately model the physical processes occurring in the plasma.
Efforts to solve the rf induction plasma problem have been hampered by a
lack of complete input data reported by the experimenters, most notably
the work coil geometry and the magnetic field intensity at the plasma
radius.

The numerical techniques and approximate analytical closed form
solutions of the energy balance equation and Maxwell's equations used to
describe the plasma require a knowledge of the electric and magnetic field
values at the plasma radius and the coil geometry. The only comparisons
of theoretical solutions with experimental results to date have been in-
direct comparisons based on reported power requirements.

Measurements of the temperature profiles in an rf argon plasma
were made over magnetic field intensities ranging from 20 amp turns/cm to
80 amp turns/cm. The results were compared with a one-dimensional numeri-
cal treatment of the governing equations and with an approximate closed
form analytical solution that neglected radiation losses.

The average measured temperatures in the plasma compared well with
the numerical treatment, though the experimental profile showed less of an
off center temperature peak than predicted by theory. This may be a re-
sult of the complex turbulent flow pattern present in the experimental

torch and not modeled in the numerical treatment. The radiation term cannot be neglected for argon at the power levels investigated. The closed form analytical approximation that neglected radiation led to temperature predictions on the order of 1000°K to 2000°K higher than measured or predicted by the numerical treatment which considered radiation losses.

The governing equations are highly coupled to the electrical conductivity of the working fluid. An aerosol of submicron tungsten particles was added to the argon to effect a significant increase in the electron number density and temperature measurements were taken and compared with the theory. The temperatures were of the order of 1000°K lower than for the cases of pure argon, and compared well with the theory at tungsten partial pressures of 4.3×10^{-3} atm and 6.1×10^{-3} atm. A tungsten partial pressure of 3.6×10^{-2} atm led to a divergence between the theory and the experiment as the tungsten atom number density reached the point that electron-tungsten collisions could no longer be neglected in the theoretical treatment of the electrical conductivity.

A parametric study was conducted to determine the effect of variations in the inputs to the analysis which can be varied experimentally, and to determine the effect that the uncertainty in the transport properties of argon has on the predicted temperature profiles.

CHAPTER I

INTRODUCTION

The recent interest in radiofrequency (rf) induction heating as a
means of producing high density plasmas has prompted work on theoretical
techniques that can adequately model the physical processes occurring in
the plasma. The theoretical treatment must include the heat transfer
problem and the determination of the electromagnetic field intensities
inside the plasma. Previous theoretical work on modeling the d.c. arc
plasma forms a basis for treating the energy balance problem, but these
equations must now be treated simultaneously with the electromagnetic
field equations as they apply to the induction arc.

Efforts to solve the rf induction plasma problem have been hampered
by a lack of complete input data reported by the experimenters. The work
coil geometry and the magnetic field intensity at the plasma radius are
needed as starting points for quantitative comparisons of spectroscopi-
cally measured temperature profiles. Experimentally measuring the mag-
netic field intensity at the plasma radius is difficult since the coil
currents are high (of the order of 50-150 amperes, rms) and the frequen-
cies are high (typically between 2 and 30 MHz).

The development of the induction arc stems from work by Hittorf[1]
on the low pressure electrodeless ring discharge. Babat[2] is credited
with inventing the induction arc in 1942 when he used a powerful vacuum
tube oscillator to raise the pressure of a ring discharge up to atmospheric

level. T. B. Reed[3] first demonstrated in 1961 that an "induction torch"
at one atmosphere could be produced. He used a 26 mm outside diameter
open ended quartz tube surrounded by a 3/16 inch copper work coil to pro-
duce an argon plasma. Spectroscopic temperature profiles of argon plas-
mas were determined by Goldfarb and Dresvin,[4] Schultz and Anderson,[5] and
Rovinskii, Gruzdev, et al.,[6] and the results of their work are presented
in Figure 1, taken from Eckert's[7] survey of the state-of-the-art of in-
duction plasmas. Stokes[8] reported temperature profiles of an argon plasma
at one atmosphere along with the power dissipated per unit length of work
coil which Eckert[9,10] used as a basis for comparison with the numerical
solutions of Pridmore-Brown[11] and his own closed-form analytical predic-
tions.[9,12] Stokes used a water-cooled quartz tube with a 2.3 cm inner
radius and excited the gas at 3.8 MHz. The power dissipation was deter-
mined from the measured heat flux into the cooling water and from the
total radiation emitted. The applied magnetic flux was not reported. A
wide range of magnetic flux intensities was used in the calculations
until the predicted radiation and conduction values matched those re-
ported in the experiment. The predicted temperature profiles were in
good agreement with spectroscopically measured values though the experi-
mental profiles were flatter, as seen in Figure 2. The experimental tem-
perature profiles were determined from continuum intensity measurements
at 4288 Å.

This dissertation describes work aimed at providing spectroscopi-
cally determined radial temperature profiles in an rf produced argon
plasma over a wide range of experimentally measured applied magnetic flux
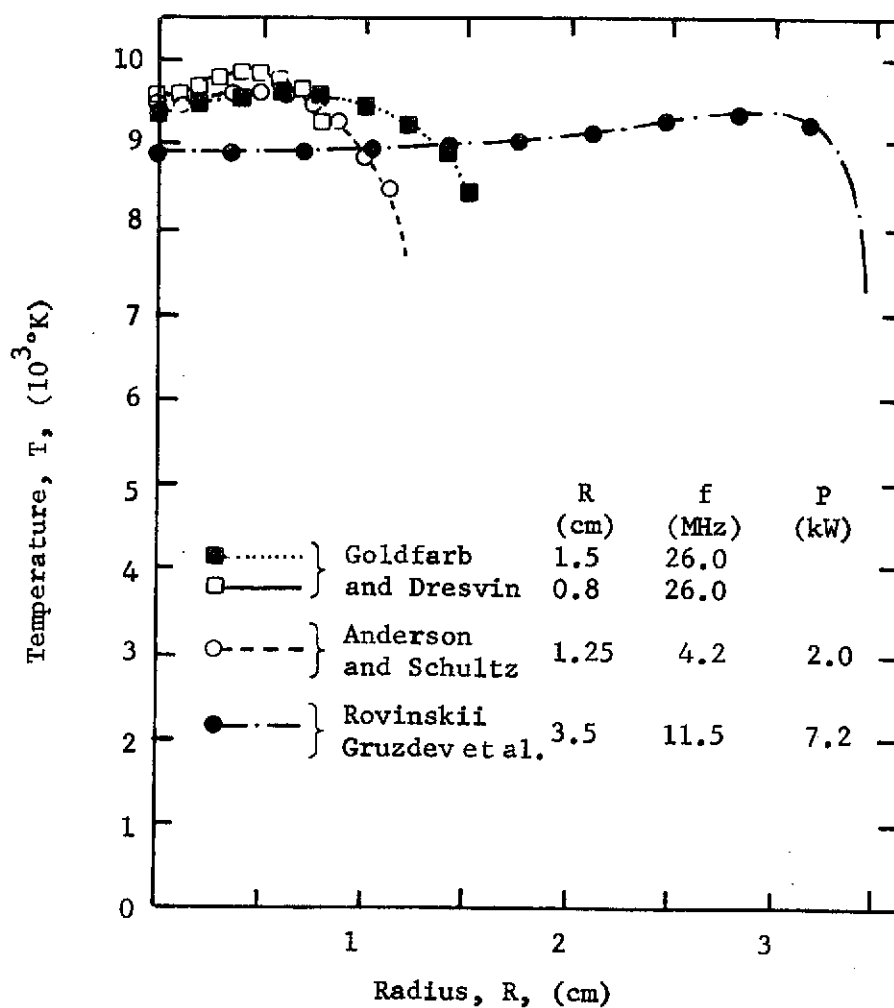
Figure 1. Measured Radial Temperature Distributions in Several
Induction Plasmas of Different Radii
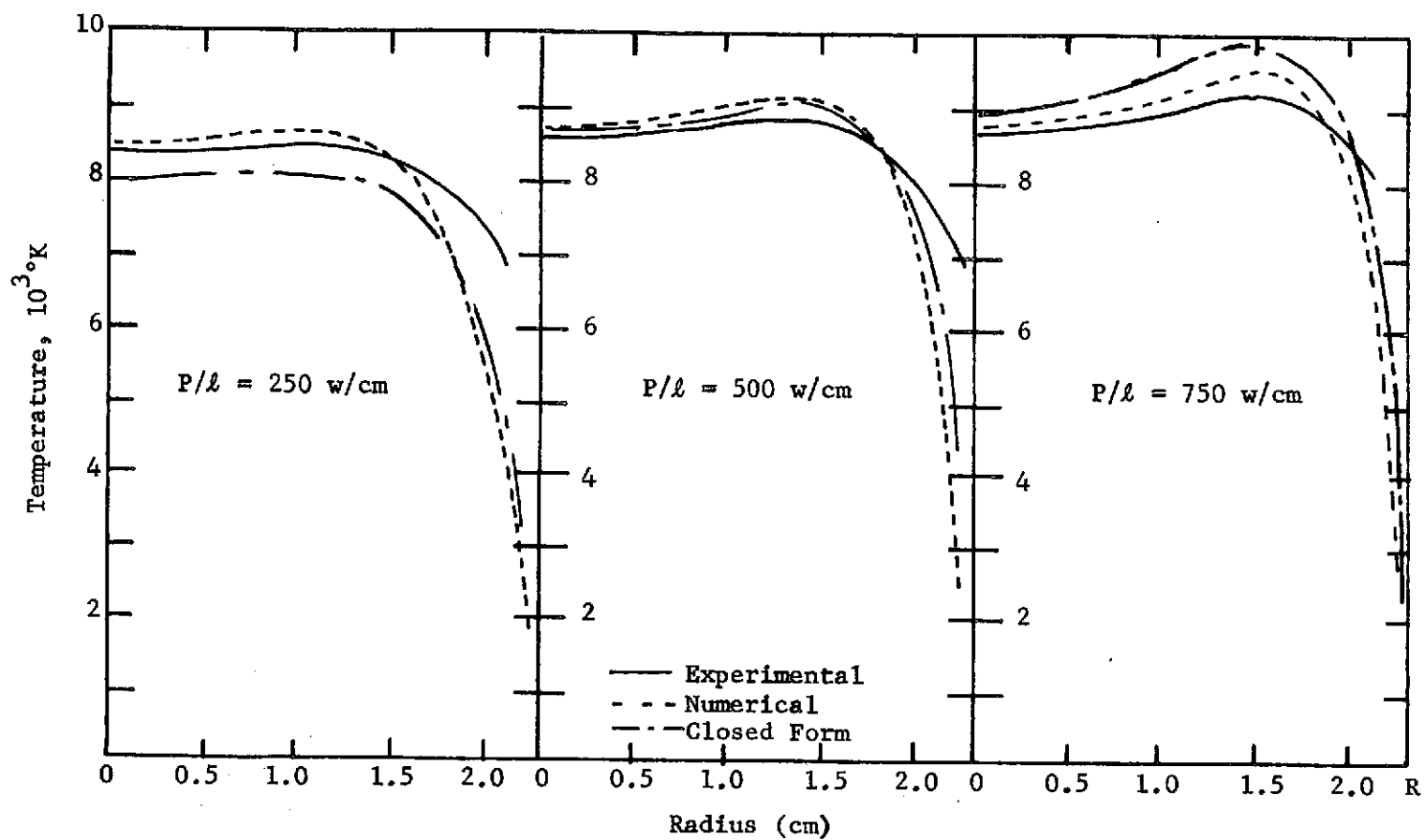
Figure 2. Comparison Between Spectroscopically Determined Temperatures, Numerical Calculations, and Closed Form Analytical Solutions

intensities and to compare the results with a representative numerical analysis based on the one-dimensional Elenbaas-Heller equation and with an approximate closed form analytical solution. A better judgment can then be made on the accuracy of these theoretical treatments. Additionally, the argon plasma is seeded with submicron tungsten particles to effect a significant change in the electrical conductivity of the gas and a comparison is made between the experimentally observed changes in the temperature profiles with those predicted by existing theory.

CHAPTER II

THEORETICAL STUDIES

Introduction

The heat balance at each position in an induction plasma arc is
given by the Elenbaas-Heller equation which balances the heat generated
through current dissipation with conduction, convection, and radiation
losses.[13,14] The heat balance equation is coupled to Maxwell's equations
governing the electric and magnetic fields in the induction plasma and
both sets of equations must be satisfied.

Analytical and numerical attempts to solve the problem are hindered
by a lack of experimental data that include all input conditions required
for quantitative comparisons, most notably the magnetic field strength
inside the work coil. Numerical methods are cumbersome and require a
digital computer. Analytical studies have failed to produce quantitative
predictions universally applicable to the variety of experimental condi-
tions and gases used in rf plasma work. Eckert and Brown[11,12] compared
their numerical method to the experimental work of Stokes,[8] but even in
this case Stokes did not measure the ampere turns of the induction coil.
This measurement is needed to determine the magnetic field strength inside
the work coil.

The transport properties of argon are examined in this chapter
because the quantitative results of the solution to the plasma problem
are dependent on the values chosen for the transport properties and the

theory serves as a basis for predicting the properties of a tungsten seeded argon plasma.

Governing Equations

Consider the plasma to be an infinite axially symmetric cylinder with an applied alternating axial magnetic field

$$H_z = H_o \exp(i2\pi\nu t) \tag{1}$$

where ν is the frequency of the alternating current I in the work coil as shown in Figure 3.

Maxwell's Equations

The relevant Maxwell equations[15] are

$$\nabla \times \bar{E} = -\frac{\partial \bar{B}}{\partial t} = -\mu \frac{\partial \bar{H}}{\partial t} \tag{2}$$

$$\nabla \times \bar{H} = \bar{J} + \frac{\partial \bar{D}}{\partial t} = \bar{J} + e \frac{\partial \bar{E}}{\partial t} \tag{3}$$

$$\bar{J} = \sigma\bar{E} \tag{4}$$

where $\bar{E}$ and $\bar{H}$ are the induced electric and magnetic field intensities, $\bar{B}$ is the magnetic induction, $\bar{D}$ is the electric displacement current, $\bar{J}$ is the electric current density, and σ is the electrical conductivity of the plasma. Equation (4) assumes a purely resistive plasma, i.e., there is no imaginary component of the conductivity. In the absence of polarization or magnetization,
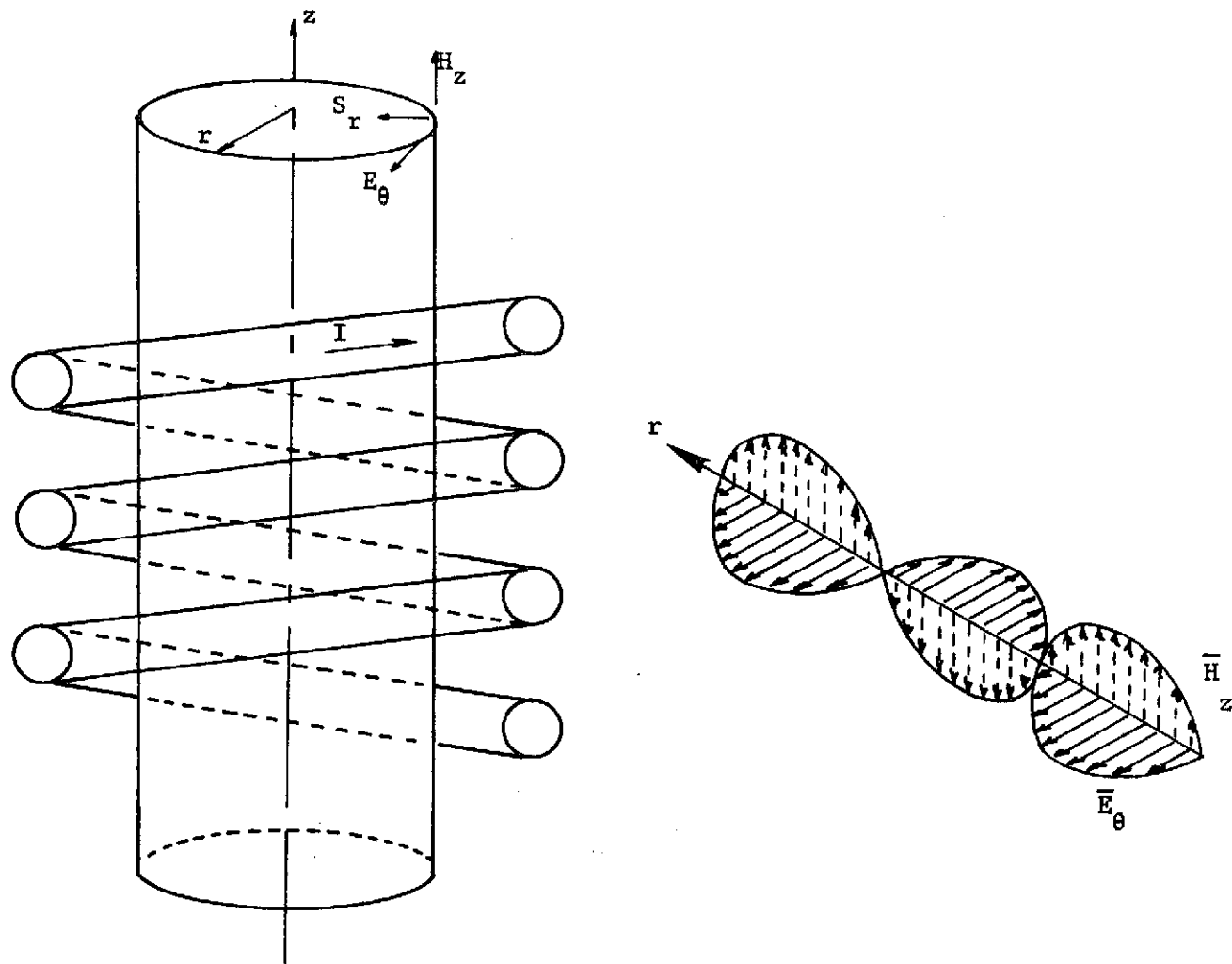
Figure 3. Cylindrical Coordinates of Plasma and Electromagnetic Field

$$\overline{B} = \mu \overline{H} \tag{5}$$

$$\overline{D} = \epsilon \overline{E} \tag{6}$$

where μ is the permeability and ϵ the permittivity of the gas. The Poynting vector $\overline{S}$, defined by $\overline{S} = \overline{E} \times \overline{H}$, represents the flux of electromagnetic energy and points in the direction of propagation of the wave.

Following the treatment of Brown, et al.[16] as modified by Freeman and Chase,[17] equation (2) expressed in cylindrical coordinates for an electric field with component E_θ only and magnetic field with axial component H_z only becomes:

$$E_\theta + r \frac{dE_\theta}{dr} = - \mu \frac{\partial H_z}{\partial t} r \tag{7}$$

or, from equation (1)

$$\frac{1}{r} \frac{d}{dr} rE_\theta = - i2\pi\nu\mu H_z \tag{8}$$

Similarly, equations (3) and (4), in the absence of displacement currents, can be expressed in cylindrical coordinates for the applicable electromagnetic field components

$$\frac{dH_z}{dr} = - J_\theta = - \sigma E_\theta \tag{9}$$

The assumption of a good conductor (i.e., no displacement currents) is equivalent to requiring

$$\sigma \gg \varepsilon 2\pi\nu \tag{10}$$

This is a valid assumption for argon at 4 MHz over the temperature range investigated as can be seen from the electrical conductivity values for argon presented later.

Equations (8) and (9) may be combined to eliminate either $\bar{H}_z$ or $\bar{E}_\theta$. Differentiating equation (8) and substituting into equation (9), the equation for the induced electric field is obtained

$$\frac{d^2 E_\theta}{dr^2} + \frac{1}{r} \frac{dE}{dr} - \left(i 2\pi\nu\mu\sigma + \frac{1}{r^2} \right) E_\theta = 0 \tag{11}$$

If E_θ is divided into its real and imaginary parts, equation (11) results in two equations

$$\frac{d^2 E_R}{dr^2} + \frac{1}{r} \frac{dE_R}{dr} - \frac{E_R}{r^2} + \sigma\mu 2\pi\nu \, E_I = 0 \tag{12}$$

$$\frac{d^2 E_I}{dr^2} + \frac{1}{r} \frac{dE_I}{dr} - \frac{E_I}{r^2} - \sigma\mu 2\pi\nu \, E_R = 0 \tag{13}$$

The rate at which electromagnetic energy in a unit volume is dissipated can be arrived at from equations (2) and (3). Scalarly multiplying equation (2) by $\bar{H}$ and equation (3) by $-\bar{E}$ and adding the two equations produces

$$\bar{H} \cdot (\nabla \times \bar{E}) - \bar{E} \cdot (\nabla \times \bar{H}) = - \frac{\partial}{\partial t} (\mu H^2 + \varepsilon E^2) - \bar{J} \cdot \bar{E} \tag{14}$$

Now using the vector identity

$$\nabla \cdot (\bar{E} \times \bar{H}) = \bar{H} \cdot (\nabla \times \bar{E}) - \bar{E} \cdot (\nabla \times \bar{H}) \tag{15}$$

to get

$$\nabla \cdot (\bar{E} \times \bar{H}) = - \frac{\partial}{\partial t} (\mu H^2 + \epsilon E^2) - \bar{J} \cdot \bar{E} \tag{16}$$

and integrating over a unit volume dτ, and applying Green's theorem to the left hand side of equation (16), one obtains

$$\int_s (\bar{E} \times \bar{H}) \cdot d\bar{s} = - \frac{\partial}{\partial t} \int_V (\epsilon E^2 + \mu H^2) d\tau - \int_V \bar{J} \cdot \bar{E} d\tau \tag{17}$$

The first term on the right hand side represents the time rate of decrease of stored electromagnetic energy in the volume and the second term on the right hand side represents losses by Joule heating or gains by an applied electric field. The left hand side then must represent the net outward flow of energy across surface s and leads to the definition of the Poynting vector $\bar{S}$

$$\bar{S} = \bar{E} \times \bar{H} \tag{18}$$

which represents the flux of electromagnetic energy. For steady state, Poynting's theorem is then

$$\nabla \cdot \bar{S} = - \bar{J} \cdot \bar{E} \tag{19}$$

or from equation (4) and for our geometry

$$\nabla \cdot \overline{S} = -\sigma |E|^2 \qquad (20)$$

If $\overline{E}$ is divided into its real and imaginary parts, E_I and E_R, the time averaged root mean square value of the electric field in the θ direction is then

$$E_\theta = \frac{\sqrt{2}}{2} (E_I^2 + E_R^2)^{\frac{1}{2}} \qquad (21)$$

and the power input per unit volume for use in the steady state energy balance equation is then σE_θ^2 or

$$\sigma E_\theta^2 = \frac{1}{2} \sigma (E_I^2 + E_R^2) \qquad (22)$$

Energy Balance Equation

The energy balance equation equates the time rate of change of energy in a unit volume with the divergence of the heat flux, the power radiated, and the electromagnetic power dissipated by the applied electric field

$$\rho C_p \frac{DT}{Dt} = \nabla \cdot \lambda \nabla T + \sigma E_\theta^2 - \Phi \qquad (23)$$

where $\frac{DT}{Dt}$ stands for the total time derivative of the temperature, T, ρ is the plasma density, C_p the specific heat at constant pressure, λ is the thermal conductivity, and Φ is the radiation source strength. The second

term on the right side of the equation represents the dissipative component of the electromagnetic energy.

Expanding equation (23) in cylindrical coordinates and assuming a constant pressure axisymmetric plasma, one obtains

$$\rho C_p \left(\frac{\partial T}{\partial t} + u_r \frac{\partial T}{\partial r} + u_z \frac{\partial T}{\partial z} \right) = \lambda \left(\frac{\partial^2 T}{\partial r^2} + \frac{1}{r} \frac{\partial T}{\partial r} + \frac{\partial^2 T}{\partial z^2} \right) \tag{24}$$

$$+ \frac{d\lambda}{dT} \left[\left(\frac{\partial T}{\partial r} \right)^2 + \left(\frac{\partial T}{\partial z} \right)^2 \right] + \sigma E_\theta^2 - \Phi = 0$$

where u_r and u_z represent the radial and axial gas velocities.

Assuming steady state conditions and rearranging the terms, one obtains the two-dimensional energy balance equation

$$\lambda \left(\frac{\partial^2 T}{\partial r^2} + \frac{1}{r} \frac{\partial T}{\partial r} + \frac{\partial^2 T}{\partial z^2} \right) + \frac{d\lambda}{dT} \left[\left(\frac{\partial T}{\partial r} \right)^2 + \left(\frac{\partial T}{\partial z} \right)^2 \right] \tag{25}$$

$$- \rho C_p \left(u_r \frac{\partial T}{\partial r} + u_z \frac{\partial T}{\partial z} \right) + \sigma E_\theta^2 - \Phi = 0$$

The energy balance equation may be reduced to one-dimensional form if it is assumed that the temperature gradients in the axial direction are very small compared to the temperature gradients in the radial direction

$$\frac{\partial^2 T}{\partial z^2} \ll \frac{\partial^2 T}{\partial r^2} \quad \text{and} \quad \left(\frac{\partial T}{\partial z} \right)^2 \ll \left(\frac{\partial T}{\partial r} \right)^2 \, .$$

$$\frac{1}{r} \frac{d}{dr} r \lambda \frac{dT}{dr} - \rho C_p u_r \frac{dT}{dr} + \sigma E_\theta^2 - \Phi = 0 \tag{26}$$

The radial flow velocity, u_r, is assumed zero in the one-dimensional analytical treatments of Eckert[9,18] and Rovenskii, et al.,[19,20] and in the one-dimensional numerical treatments by Brown,[11] and Miller and Ayen.[21] The work of Chase,[22,23] however, shows that the rf field imposes a magnetic pressure gradient that causes the charged particles to preferentially migrate toward the center of the plasma, and through collisions give a net inward radial velocity that forms a double vortex flow. Experimental work by Chase[22] on an rf plasma with a configuration similar to the one used in this research shows the radial velocity to be of the order of magnitude of 10% of the net axial flow velocity.

Equation (26) may be linearized by introducing the heat conduction potential defined by

$$S = \int_0^T \lambda \, dT \qquad (27)$$

With the aid of equation (27), equation (26) becomes

$$\frac{d^2 S}{dr^2} + \frac{1}{r}\frac{dS}{dr} - \frac{\rho C_p u_r}{\lambda}\frac{dS}{dr} + \sigma E_\theta^2 - \Phi = 0 \qquad (28)$$

If E_θ is divided into its real and imaginary parts as shown in equation (21), equation (28) becomes

$$\frac{d^2 S}{dr^2} + \frac{1}{r}\frac{dS}{dr} - \frac{\rho C_p u_r}{\lambda}\frac{dS}{dr} + \frac{1}{2}\sigma (E_R^2 + E_I^2) - \Phi = 0 \qquad (29)$$

and equations (12,13, and 29) along with the continuity equation in cylindrical coordinates

$$\frac{1}{r}\frac{d}{dr}\left(r\rho u_r\right) = 0 \tag{30}$$

and boundary conditions:

$$
\begin{array}{ll}
& \dfrac{dS}{dr} = 0 \\[2mm]
r = 0 \quad E_R = 0 \qquad & r = R \quad \dfrac{dE_R}{dr} + \dfrac{E_R}{r} = 0 \\[2mm]
E_I = 0 & \dfrac{dE_I}{dr} + \dfrac{E_I}{r} = - 2\pi\mu\nu H(R)
\end{array}
\tag{31}
$$

$$S = \int_0^{T_{wall}} \lambda dT$$

form a one-dimensional system of equations that describe the plasma.

Solution Techniques

Eckert[7] provides an up to date review of the reported techniques used for numerical solutions to the equations governing the induction arc as well as the assumptions necessary for approximate closed form solutions. He pointed out that lack of complete input data from reports of experimental work makes quantitative comparisons difficult and that experimenters did not attempt to minimize two-dimensional or convection effects in their work.

Keefer[24] at the University of Florida, developed a one-dimensional numerical technique programmed under the direction of Sprouse[25] at the Arnold Engineering Development Center. This program (called SUPERSIX) was obtained and converted to run on the Univac 1108 at Georgia Tech to permit a comparison of the experimental work reported in this dissertation with a numerical analysis of the governing equations.

The analysis reduces the sixth order system of equations given by

equations (12, 13, 29, 30) to six first order differential equations as follows. Defining

$$y_1 = \frac{S}{S_w} = \frac{\int_o^T \lambda \, dT}{\int_o^{T_w} \lambda \, dT} \qquad (32)$$

where T_w is the input wall temperature and

$$y_2 = \frac{dy_1}{dx} \qquad (33)$$

$$y_3 = E_R$$

$$y_4 = x \frac{dE_R}{dx}$$

$$y_5 = E_I$$

$$y_6 = x \frac{dE_I}{dx}$$

where x is the non-dimensional radial position $x = r/R$, one obtains from equations (12, 13, 29, 30)

$$\frac{dy_1}{dx} = y_2 \qquad (34)$$

$$\frac{dy_2}{dx} = \left(\frac{R\rho u_R \, C_p(y_1)}{x \, \lambda} - \frac{1}{x}\right) y_2 - \frac{R^2 \sigma(y_1)}{2S_w} (y_3{}^2 + y_5{}^2) + \frac{R^2 \Phi(y_1)}{S_w}$$

(continued)

$$\frac{dy_3}{dx} = \frac{1}{x} \, y_4$$

$$\frac{dy_4}{dx} = \frac{1}{x} \, y_3 - 2R^2 x \sigma \mu \, 2\pi \nu y_5$$

$$\frac{dy_5}{dx} = \frac{1}{x} \, y_6$$

$$\frac{dy_6}{dx} = \frac{1}{x} \, y_5 + 2R^2 x \sigma \mu \, 2\pi \nu y_3$$

where R is the plasma radius with boundary conditions

$$x = 1 \; : \; y_1 = 1; \; y_5 + y_6 = - \; 2\pi \mu \nu RH(R); \; y_3 + y_4 = 0 \qquad (35)$$

$$x = 0 \; : \; y_2 = y_3 = y_5 = 0$$

A Runge-Kutta integration scheme is used to solve the system of equations (34,35) with the required inputs being frequency, wall temperature, plasma radius, and magnetic field strength at the outer surface of the plasma. The radial flow velocity at the wall is input through the term $\rho u_r R$. Provisions are made in the program for parametric analysis using the last plasma profile as the initial guess for a new case where only one input parameter is slightly varied. The analysis does not take axial convection into account, as can be seen from the governing equations. Typical run times on the Univac 1108 for convergence to the first case are 20-30 minutes.

The analytical work of Gruzdev, Rovenskii, and Sobolev[19,20] provides

a simplified closed form solution to the one-dimensional problem that is useful for comparison with the numerical method and the results of this research. By considering E and H as root mean square values such that the value of the Poynting vector becomes E·H and neglecting radial convection and radiation, the one-dimensional energy balance equation for steady state becomes

$$\nabla \cdot \lambda \nabla T + \nabla \cdot EH = 0 \tag{36}$$

or in cylindrical coordinates

$$\frac{1}{r} \frac{d}{dr} \left(rEH - r \lambda \frac{dT}{dr} \right) = 0 \tag{37}$$

Since both fluxes vanish at r = 0

$$\lambda \frac{dT}{dr} = EH \tag{38}$$

From equation (9)

$$\lambda \frac{dT}{dr} = - \frac{H}{\sigma} \frac{dH}{dr} \tag{39}$$

Integrating equation (39) from the outer boundary r = R where the temperature equals the wall temperature, T_w, and the magnetic field has a value at the boundary of H_R

$$\int_{T_R}^{T} \sigma(T) \; \lambda(T) \; dT = - \int_{R}^{r} H(r) \; dH = \frac{H_R^2}{2} \left[1 - \left(\frac{H(r)}{H_R}\right)^2 \right] \tag{40}$$

If the magnetic field as a function of r is known, the temperature at any point may be calculated. If $H(0) \ll H_R$, which is a good assumption according to the experimental work of Eckert[26] and the theoretical predictions of the numerical analysis, then the maximum temperature (which occurs at the center of the plasma in the case of no radiation) may be approximated from the magnetic field at the plasma radius from

$$H_R = \left[2 \int_{T_w}^{T(0)} \sigma(T) \; \lambda(T) \; dT \right]^{\frac{1}{2}} \tag{41}$$

The choice of T_w does not affect the final $T(0)$ for a given H_R for argon as long as $T_w < 4000°K$ because of the very low values of σ and λ below about $5000°K$.

Transport Properties

The values chosen for the transport properties of argon, namely the electrical and thermal conductivities and radiation source strength, bear directly on the quantitative results of the analysis of the governing equations. The values are also important because they form the basis for predicting the changes in the properties in those cases where the plasma was seeded with tungsten.

Electrical Conductivity

The mobility, μ, of a gas is defined in terms of the drift velocity

of the electrons, $\bar{u}$ and the applied electric field, $\bar{E}$

$$\mu = \frac{\bar{u}}{\bar{E}} \tag{42}$$

and the electrical conductivity, σ, in terms of the current density, $\bar{J}$, is given by

$$\bar{J} = \sigma\bar{E} = \frac{\sigma\bar{u}}{\mu} \tag{43}$$

If it is assumed that an electron loses all of its momentum in each collision, then

$$q\bar{E} = m_e\bar{u}\nu_e \tag{44}$$

where q is the elementary electric charge, m_e is the mass of an electron, and ν_e is the electron collision frequency. From equations (43) and (44) the average drift velocity is

$$\bar{u} = \frac{q\bar{E}}{m_e\nu_e} \tag{45}$$

and the current density is

$$\bar{J} = qN_-\bar{u} \tag{46}$$

where N_- is the number density of electrons. Substituting equation (45) into equation (46)

$$\bar{J} = \frac{q^2 N_- \bar{E}}{m_e \nu_e}$$ (47)

or from equation (43)

$$\sigma = \frac{q^2 N_-}{m_e \nu_e}$$ (48)

The electron collision frequency can be expressed in terms of Q_{ei}^j (the effective momentum transfer collision cross section between electrons and species i of gas j), the velocity of the electrons v_e, and the number density of species i of gas j N_i^j.

$$\nu_e = \sum_j \sum_i N_i^j \overline{v_e Q_{ei}^j}$$ (49)

where the mean quantity $\overline{v_e Q_{ei}^j}$ may be approximated by $\bar{v}_e Q_{ei}^j$ when Q_{ei}^j is taken at $\bar{v}_e$. Then

$$\nu_e \simeq \bar{v}_e \sum_j \sum_i N_i^j Q_{ei}^j$$ (50)

If the electron velocity distribution is Maxwellian

$$\bar{v}_e = \left(\frac{8kT_e}{\pi m_e}\right)^{\frac{1}{2}}$$ (51)

where k is the Boltzmann constant and T_e is the electron temperature. Then

$$\sigma = \frac{q^2 N_-}{\left(\frac{m_e 8kT_e}{\pi}\right)^{\frac{1}{2}} \sum_j \sum_i N_i^j \, Q_{ei}^j}$$

(52)

The Saha equation predicts the number density of electrons from the number density of neutrals of gas j, N_0^j

$$N_-^j = \left(\frac{N_0^j \, 2u_+^j(T)}{u_0^j(T)}\right)^{\frac{1}{2}} \frac{(2\pi m_e k)^{\frac{3}{4}}}{h^{\frac{3}{2}}} \, T_e^{\frac{3}{4}} \left(\exp - \left(\frac{\varphi^j - \Delta E}{kT}\right)\right)^{\frac{1}{2}}$$

(53)

where h is Planck's constant, φ^j is the ionization potential of gas j, ΔE is the lowering of the ionization potential due to increased charged particle interactions found in the high temperature high density environment of a plasma, and u_+^j and u_0^j are the partition functions for singly ionized and neutral atoms defined by

$$u_0^j = \sum_{s=1}^{s=n^*} g_s \, e^{-E_s/kT}$$

(54)

$$u_+^j = \sum_{s=1}^{s=n^*} g_s^+ \, e^{-E_s/kT}$$

where g_s and g_s^+ are the statistical weights of the neutral and singly ionized atoms at excitation level s (s = 1 ground state) and E_s is the bound energy of level s. Substituting equation (53) into equation (52) and simplifying

$$
\sigma = \frac{q^2 \pi \left(\dfrac{m_e k \pi T_e}{8}\right)^{\frac{1}{4}} \sum\limits_{j} (N_0^j)^{\frac{1}{2}} \sqrt{\dfrac{2u_+^j(T)}{u_0^j(T)}} \left(e^{-\left(\dfrac{\varphi^j - \Delta E}{kT}\right)}\right)^{\frac{1}{2}}}{h^{\frac{3}{2}} \sum\limits_{j} \sum\limits_{i} N_i^j Q_{ei}^j}
\tag{55}
$$

For the case of argon only, equation (55) becomes

$$
\sigma_{Ar} = \frac{q^2 \pi \left(\dfrac{m_e k \pi T_e}{8}\right)^{\frac{1}{4}} N_D^{Ar \, \frac{1}{2}} \sqrt{\dfrac{2u_+(T)}{u_0(T)}} \left(e^{-\left(\dfrac{\varphi - \Delta E}{kT}\right)}\right)^{\frac{1}{2}}}{h^{\frac{3}{2}} \sum\limits_{i} N_i^{Ar} Q_{ei}^{Ar}}
\tag{56}
$$

Figure 4 is a compilation of results from the theoretical works of De-
voto,[27] Yos,[28] Cann,[29] and Cambel,[30] and the experimental work of Emmons,[31]
Lin et al.,[32] and Lau.[33] The empirical values used in this study are
determined by an analytical expression that best represents the available
experimental and theoretical data.

For the case of argon seeded with submicron tungsten particles,
the summation over j in equation (55) must now include both argon and
tungsten. Performing this summation and factoring out the expression for
pure argon conductivity one obtains

$$
\sigma_{Ar+w} = \sigma_{Ar} \left[\frac{1 + \sqrt{\dfrac{N_0^w}{N_0^{Ar}} \dfrac{u_+^w}{u_0^w} \dfrac{u_0^{Ar}}{u_+^{Ar}}} \exp\left[\dfrac{\varphi^{Ar} - \varphi^w}{kT}\right]}{1 + \dfrac{\sum\limits_{i} N_i^w Q_{ei}^w}{\sum\limits_{i} N_i^{Ar} Q_{ei}^{Ar}}} \right]
\tag{57}
$$

Substituting in values for φ^{Ar} and φ^w from Drawin and Felenkok[34] and
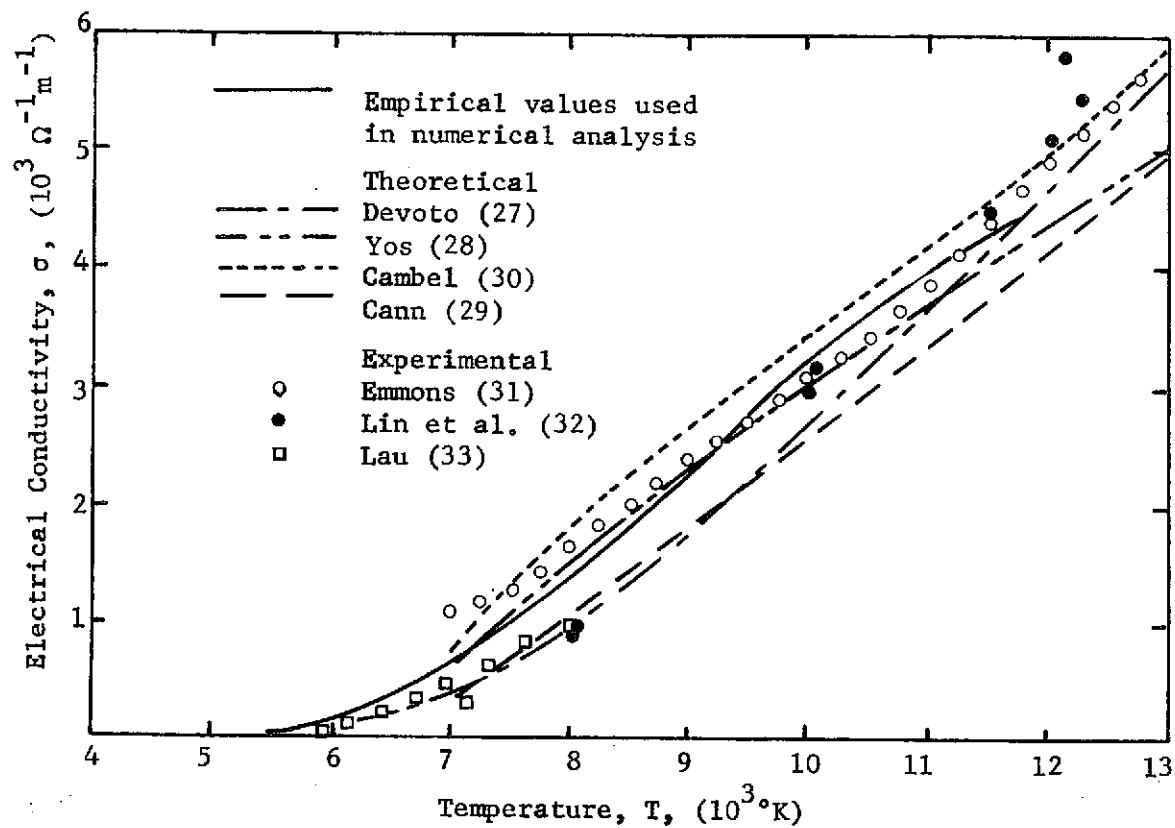
Figure 4. Theoretical and Experimental Values for Electrical
Conductivity of Argon at High Temperatures

average values for u_+^{Ar} and u_0^{Ar} from Olsen[35] and taking $\dfrac{u_+^w}{u_0^w} = 1$ from Laun[36] equation (57) becomes

$$\sigma_{Ar+w} = \left[\frac{1 + \sqrt{\left(\dfrac{N_0^w/N_0^{Ar}}{5.519}\right) \exp\,[7.78/kT]}}{1 + \dfrac{\sum\limits_i N_i^w Q_{ei}^w}{\sum\limits_i N_i^{Ar} Q_{ei}^{Ar}}} \right] \qquad (58)$$

The electron collision cross sections for tungsten have not been calculated or experimentally measured, but based on the cross sections of other metals[37] and on the predicted values of uranium and similar metals,[38] it was assumed that $(\sum\limits_i N_i^w Q_{ei}^w)/(\sum\limits_i N_i^{Ar} Q_{ei}^{Ar}) \ll 1$. This assumption is suspect for tungsten number densities greater than one percent of the argon number density.

The effect of the seed can be seen in Figure 5 which shows the electrical conductivity of seeded argon from equation (58) compared with the conductivity of pure argon.

Thermal Conductivity

A compilation of argon thermal conductivity data is plotted in Figure 6 showing the theoretical work by Devoto,[27] Yos,[28] Admur and Mason,[39] Cann,[29] and the experimental work of Emmons,[31] and Knopp and Cambel.[40]

An analytical expression that yields the empirical values used in the numerical analysis was fit to the experimental data. It is felt that the experimental values are more reliable since they are easy to measure and are in good agreement, while the theoretical basis for thermal con-
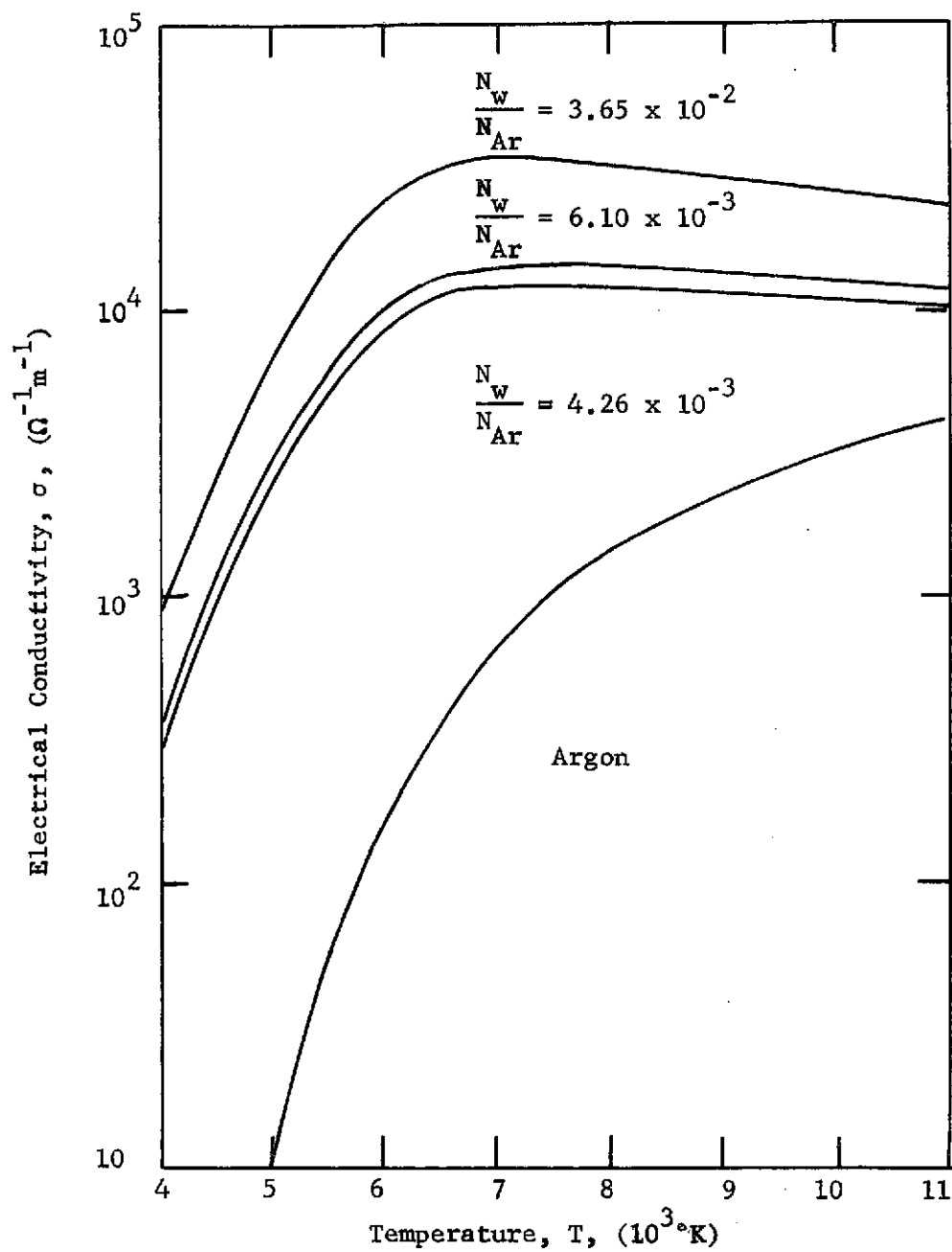
Figure 5. Electrical Conductivity of Tungsten Seeded Argon
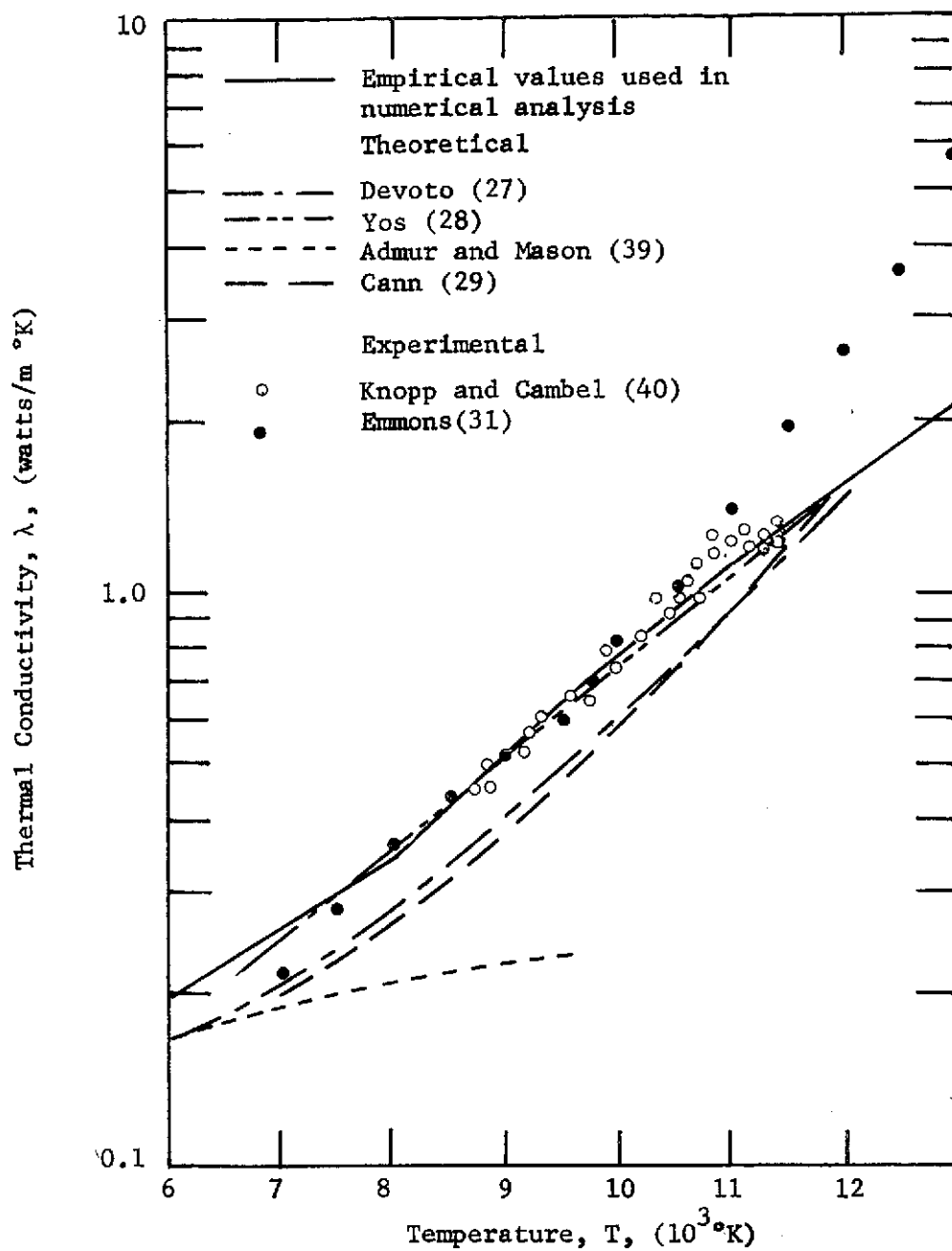
Figure 6. Theoretical and Experimental Values for Thermal
Conductivity of Argon at High Temperatures

ductivity is quite complex.

Devoto[27] conveniently treated the contribution of the electrons to the thermal conductivity of the plasma separately, so the effect of the addition of tungsten seed was assumed to be an increase of the electron contribution to the thermal conductivity, due to an increase in the electron number density. The effect of the tungsten collisions on the heavy atom thermal conductivity was neglected because of the low tungsten partial pressures. For evaluations of the case of tungsten seeded argon, the thermal conductivity due to the heavy atoms was assumed the same as that of pure argon. The contribution of the electrons to the thermal conductivity was calculated by taking the value of the electron component of the thermal conductivity of pure argon at the temperature required to produce the same number density of electrons as was present in the seeded case. Figure 7 is a plot of the thermal conductivity assumed in the analysis and a plot of the thermal conductivity of the tungsten seeded argon for tungsten number densities used in the experiment where the electron contribution is added at a temperature that yields an equivalent electron number density for the case of pure argon. This approach to accounting for the tungsten is considered to be as good an approach as possible at the present time due to lack of data on heavy metal collision cross sections.

Radiation Source Strength

The values used in the numerical analysis for the radiation source strength term were taken from the d.c. arc data of Emmons[31] modified below 9000°K to bring them more in line with the theoretical estimates of Horn[41]
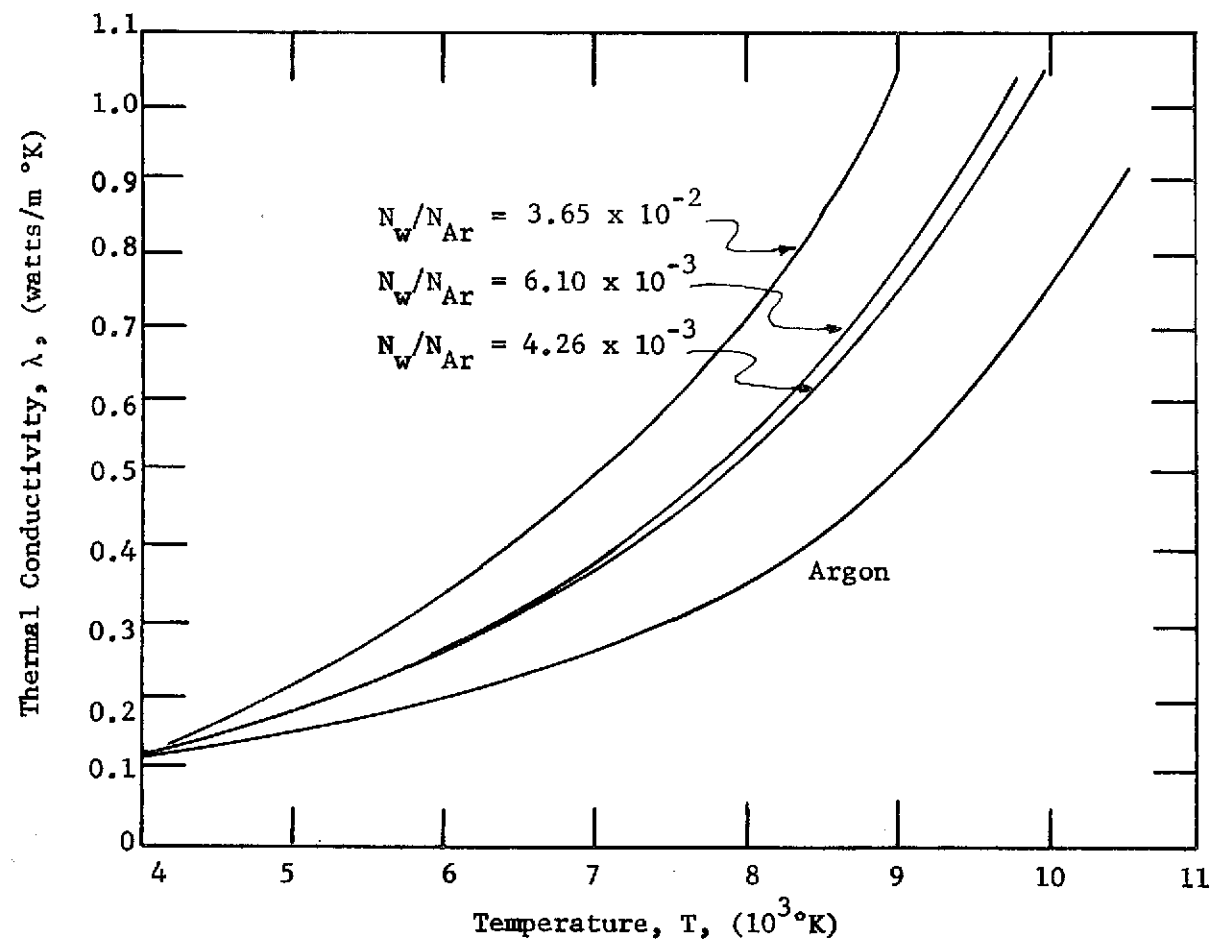
Figure 7. Thermal Conductivity of Tungsten Seeded Argon

The y-axis is labeled "Thermal Conductivity, λ, (watts/m °K)" with values from 0 to 1.1.

The x-axis is labeled "Temperature, T, $(10^3 °K)$" with values from 4 to 11.

Curve labels:
$N_w/N_{Ar} = 3.65 \times 10^{-2}$
$N_w/N_{Ar} = 6.10 \times 10^{-3}$
$N_w/N_{Ar} = 4.26 \times 10^{-3}$
Argon

and the more recent induction discharge data obtained by Stokes.[42] It was felt that the induction arc data were more reliable at the lower temperatures. Stokes[42] points out that "An important difference between the induction discharge experiments reported here and the arcs used for most of Emmons work is that stable, much larger plasmas can be obtained at low peak temperatures with induction heating." Pridmore-Brown,[11] in his numerical analysis, did much the same things at the suggestion of Eckert who felt that Emmons' values were too high at low temperatures. Miller and Ayen[21] arrived at a radiation source strength term for their two-dimensional analysis by extrapolating the data of Evans and Tankin[43] to lower temperatures which yielded values significantly below those of Emmons at temperatures below 10,000°K.

Figure 8 is a plot of the experimental data of Emmons,[31] Stokes,[42] Evans and Tankin,[43] and Schreiber and Hunter[44] along with the theoretical values derived by Horn,[41] and the values predicted by the Kramer-Unsold[45] theory. The empirical values chosen for this work are also plotted. The radiation source strength term was not modified for the addition of tungsten seed. Work by United Aircraft[46] on tungsten seeded plasmas with similar operating characteristics shows less than a 10% increase in power radiated for tungsten partial pressures on the order of 0.005 atm. This assumption may not be valid for higher tungsten partial pressures.

Effect of Magnetic Field

The magnetic field strength in the coil for the case of no plasma represents a maximum, since the field strength within the plasma is reduced. Assuming an rms current of 100 amps in the work coil and an effec-
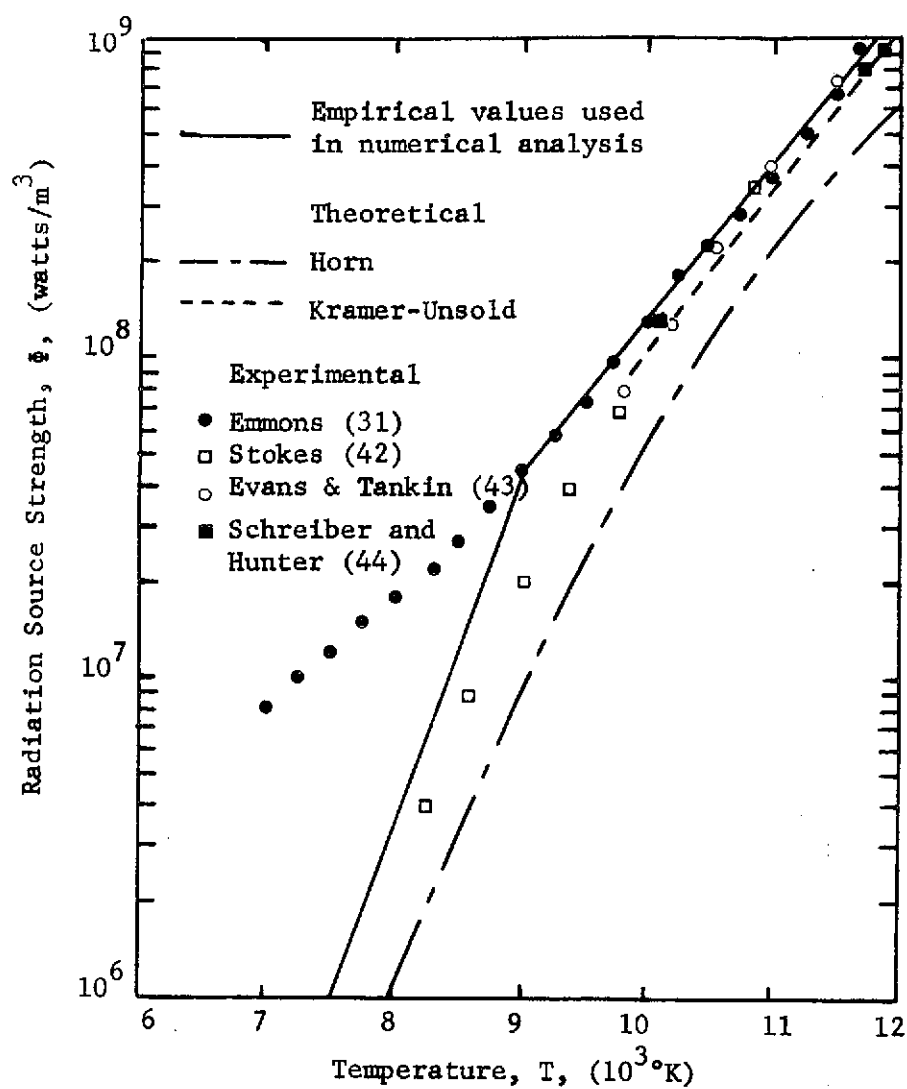
Figure 8. Theoretical and Experimental Values for Argon Radiation Source Strength at High Temperatures

tive turn per cm of 0.52 (verified by experiment--see Appendix A), the
magnetic field intensity would be 52 amp-turns/cm, which corresponds to a
magnetic induction of about 5×10^{-3} webers/m^2, or 50 gauss. The work of
Devoto[27] has shown that it would take a magnetic induction of one to two
orders of magnitude greater to cause any change in the transport proper-
ties. Further, the results of the numerical analysis and the experimental
work of Eckert[47] and Trekhov et al.[48] show the magnetic induction inside
the plasma to be an order of magnitude lower than the field strength at
the plasma radius.

CHAPTER III

INSTRUMENTATION AND EQUIPMENT

RF Plasma Generator

The radio-frequency plasma generator and associated gas flow system was designed and built by Dr. Robert A. Benns as part of his dissertation research. A detailed description of the equipment and theory of operation are found in his dissertation.[49]

The generator operates at 4 MHz and utilizes an air cooled Eimac 4CX-35000C tetrode with an output power of up to 85 kW. The torch and operating controls are located in a copper lined room with a viewing port in the wall that allows spectroscopic observation of the plasma from the adjacent diagnostics room. The copper shielding is necessary to insure that stray rf fields are not present in the diagnostics equipment. The plasma generator operating parameters are listed in Table 1.

The plasma is contained in a 40.64 cm long quartz tube with an inside diameter of 5.08 cm and a wall thickness of 1.75 mm. A 1/4 inch water cooled copper work coil surrounds the torch. The work coil is approximately 9 cm long with a coil pitch of approximately 2/3 turn per cm. The pitch of the work coil is not constant but has been varied to allow a large enough space between the second and third turns from the bottom to permit scanning of the entire diameter of the plasma without coil interference. The exact geometry of the coil and torch is drawn to scale in Figure 33 of Appendix A.

Table 1. Plasma Generator Operating Parameters

	Operating Value	Maximum Rating
dc plate voltage	16,500 volts	20,000 volts
dc grid voltage	- 400 volts	
dc screen voltage	750 volts	2,500 volts
dc plate current	6.2 amperes	15 amperes
dc grid current	.14 amperes	
dc screen current	.50 amperes	
peak rf plate voltage	15,900 volts	
peak rf plate current	9.3 amperes	
peak rf grid voltage	500 volts	
peak rf grid current	.28 amperes	
input impedance	1,785 ohms	
output impedance	1,892 ohms	
total plate input power	102,000 watts	
plate dissipation	28,000 watts	35,000 watts
grid dissipation	14 watts	500 watts
screen dissipation	200 watts	1,750 watts
grid driving power	70 watts	
plate output power	74,000 watts	
plate efficiency	72.5 percent	

A water cooled copper electrode is inserted through a size 12 rubber stopper in the bottom of the torch. The tip of the electrode is coated with tungsten. The electrode serves as ground for the arc welder during the starting process and also helps stabilize the vortex flow in the tube. Figure 9 shows the quartz torch with the stopper and electrode in place. The center of the electrode is open to allow a regulated amount of gas flow through the center of the tube. The primary vortex gas flow is from the two copper tubes inserted near the perimeter of the stopper. The ends of the copper tubes are closed off and a small hole drilled in each provides flow tangential to the tube wall inclined 45 degrees in the upward direction.

The gas flow system is designed to allow any desired combination of pure argon and aerosol to enter either the tangential flow copper tubes or the center flow through the water cooled electrode. In practice, very little flow could be sustained through the center electrode without plasma extinction, thus only a small pure argon flow was used which raised the visible plasma flame off the surface of the electrode. Samples of the gas were taken when tungsten aerosol was injected in the plasma to determine the aerosol density. This was accomplished by operating the solenoids that allowed the vacuum tank to draw in a measured volume of aerosol through previously weighed filter papers. Two samples were taken for every aerosol run to insure a consistent aerosol and to give some basis for ascertaining the accuracy of this measurement.

The submicron tungsten particles are injected into the plasma in an argon aerosol using the same gas flow system. This is accomplished by
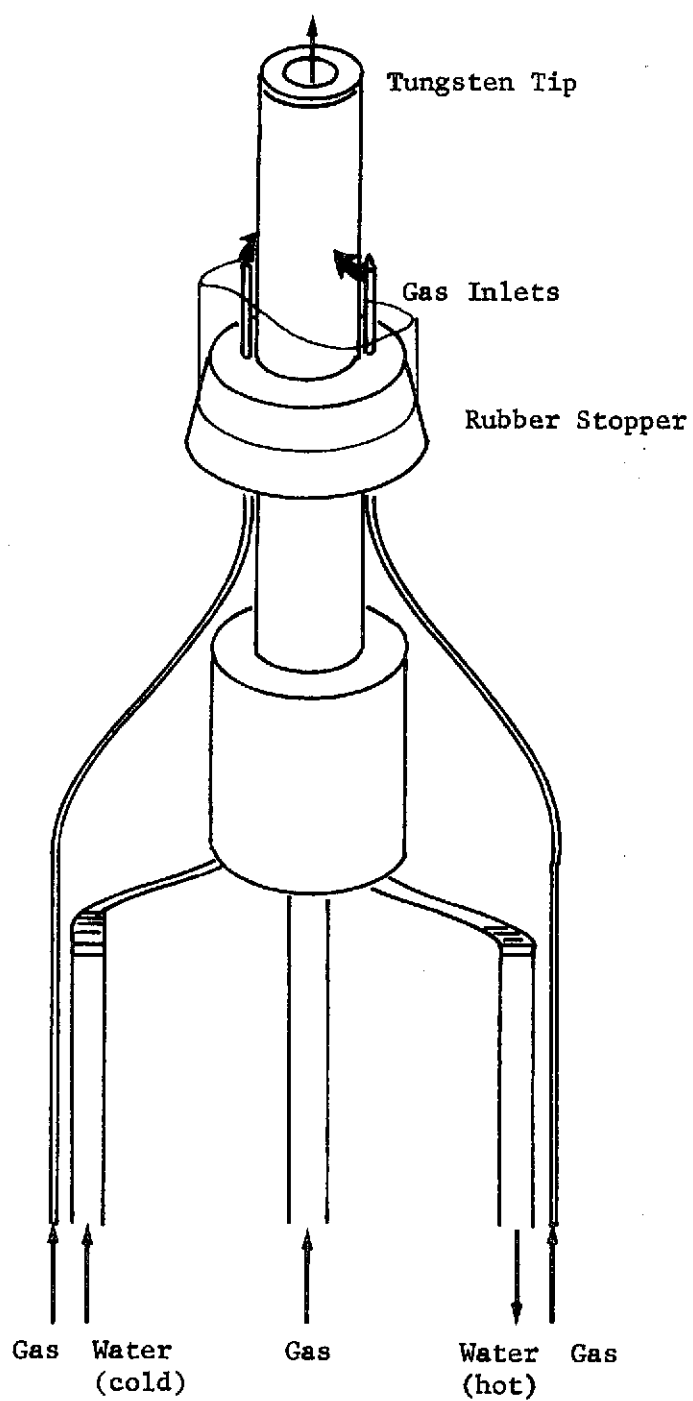
Figure 9. Quartz Tube with Water-Cooled Center Electrode and Copper Gas Flow Tubes

allowing a set fraction of the pure argon to flow into a large test tube filled with dry tungsten powder. The injected argon agitates the reservoir of tungsten powder on the bottom of the tube and creates an aerosol in the upper volume of the tube. The tube is mounted vertically on a vibrator and the aerosol is drawn off the top of the tube and mixed with the pure argon that bypassed the tube. The major drawback is that it takes approximately two minutes for the aerosol density to stabilize. Because the plasma coupling has such a large dependence on the aerosol density, stabilization of the screen and grid currents of the power amplifier tube is a good indication of aerosol density stabilization. Figure 10 is a drawing of the test tube configuration. The tube is mounted vertically on a vibrator.

Diagnostics Instrumentation

The plasma diagnostics instrumentation is contained in a room adjacent to the plasma generator with a viewing port in the wall between the two rooms. A schematic diagram of the instrumentation and optics used for spectroscopic observation of the plasma is given in Figure 11.

The optics are mounted on a four by six foot Ealing optical table. Magnetic optical rails and carriers are used so that the optical components can be easily adjusted. A lens with a focal length of 743 mm focuses an enlarged image of the plasma on the entrance slit of the spectrometer. The scanning mirror, mounted on a custom made precision scanner, rotates without vibration. This causes the plasma image to move across the entrance slit of the spectrometer. A potentiometer is mounted with amplification gears on the scanning mechanism and the variable resistance
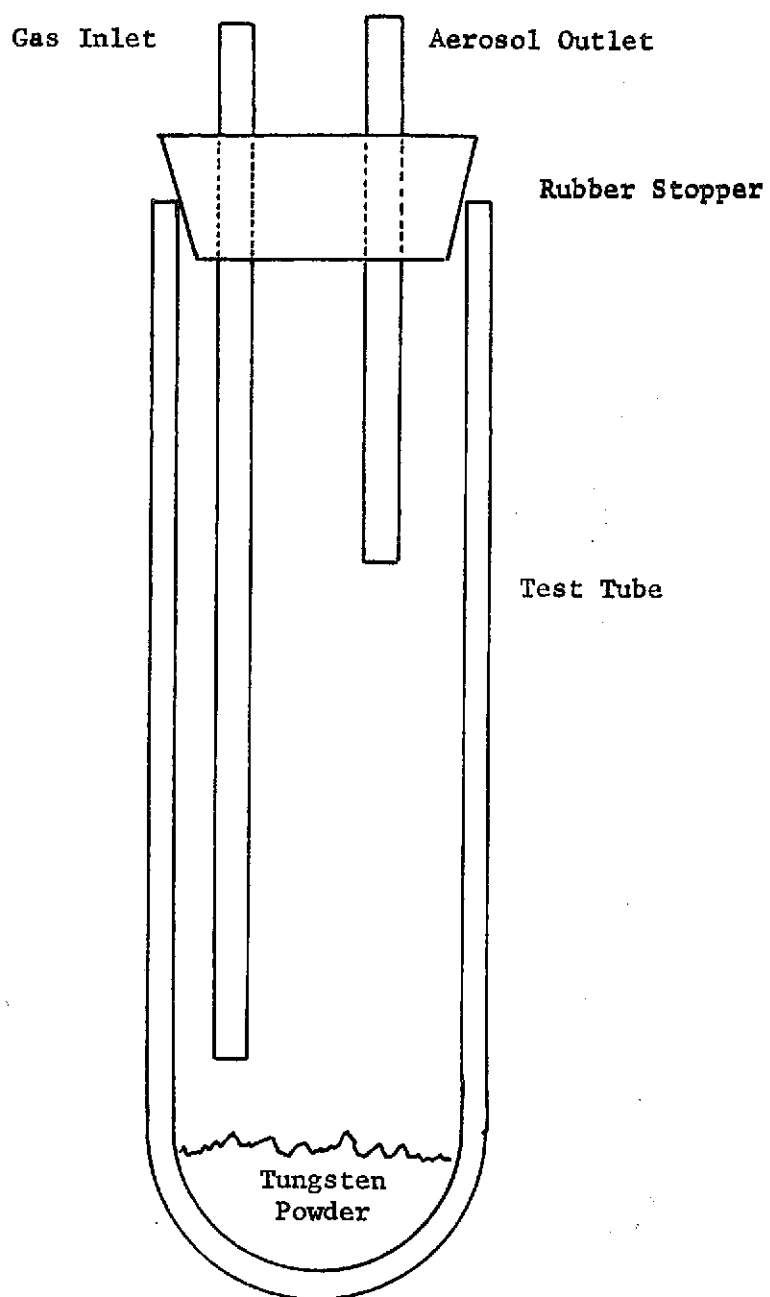
Figure 10. Test Tube Aerosol Generator
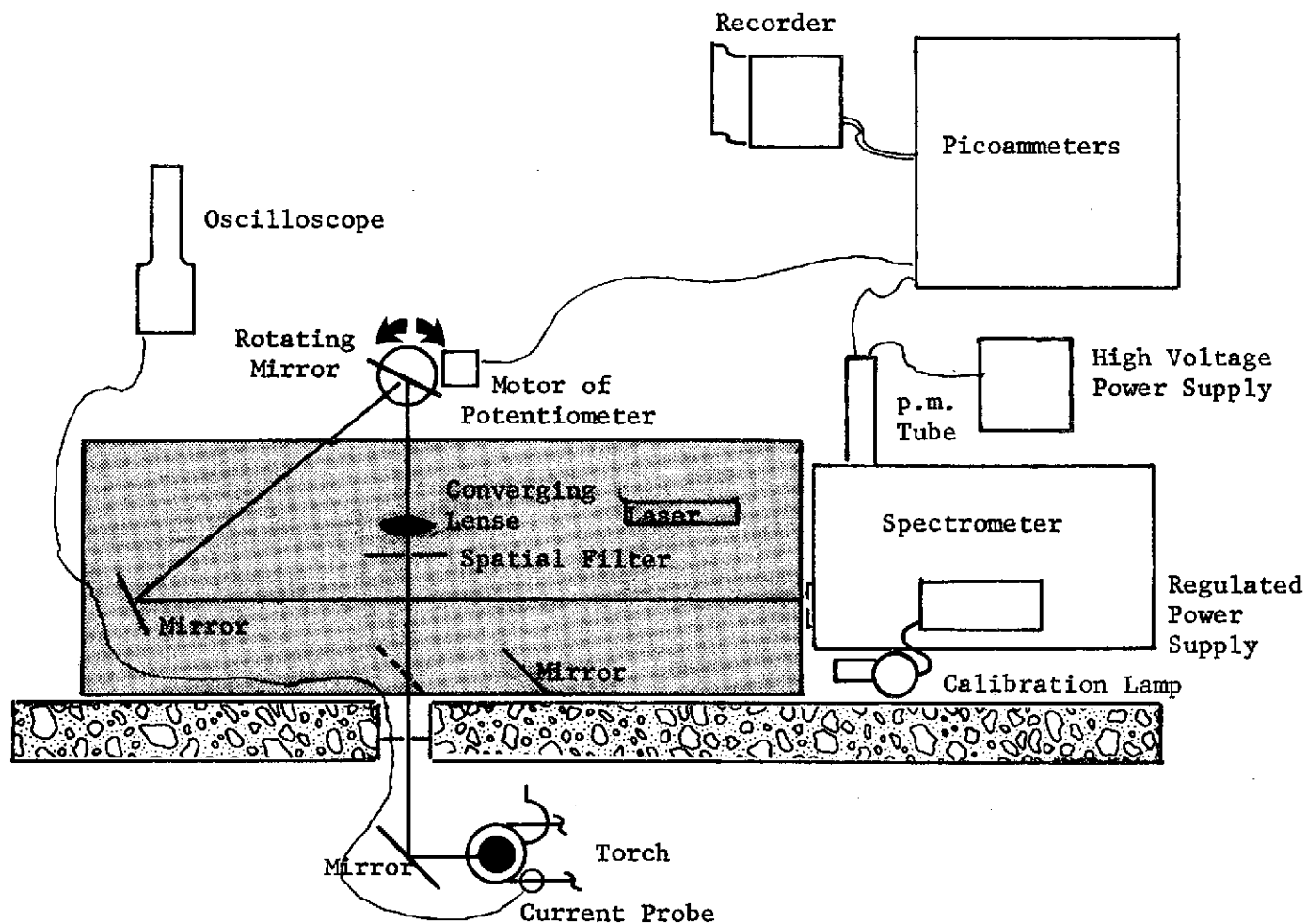
Figure 11. Optics and Instrumentation Set-Up

is calibrated to provide a spatial position trace on the visicorder output. Spatial filters are used to insure that no stray reflected light from the plasma is reflected through the viewing port. A laser is used to locate the optical path and allow the spatial calibration of the scanning mechanism. This is accomplished by noting the visicorder indication from the scanning potentiometer when the laser is at the torch radius.

The spectrometer is a McPherson Model 2051 scanning monochromator with a one meter focal length and an f 8.7 plane diffraction grating. The grating is 102 mm x 102 mm with 1200 lines/mm and is blazed for 5000 Å. An EMI 9558QA photomultiplier tube is mounted on the exit slit. The entrance slit width and the exit slit to the photomultiplier are set at 50 μ for all continuum observations. The light entering the spectrometer falls on only a small part of the grating and remains entirely on the grating during the spatial scan. The photomultiplier has 1000 V applied which is in the linear range of the tube.

The output of the photomultiplier tube and the scanning potentiometer is monitored by one of three picoammeters and recorded by a visicorder which uses light sensitive paper and pinpoints of light to leave a permanent trace of the picoammeter output. The response time of the system is limited by the visicorder which has a full scale response time of approximately .02 second.

The absolute calibration of the system is accomplished with a tungsten strip lamp and regulated power supply traceable to the National Bureau of Standards. The lamp is mounted as shown in Figure 11 and a remotely movable mirror, identical to the mirror in the plasma room, is used

to provide a substitute optical path. Half of a quartz tube is placed in the path of the lamp to simulate the torch. Figure 12 is a plot of the NBS tungsten strip lamp at 35 amps vs. wavelength and Figure 13 is a plot of the absolute sensitivity of the optical system vs. wavelength.

The coil current is measured with a Tektronix P6021 high frequency current probe and Type 134 current probe amplifier fed into a Tektronix Model 597 cathode ray oscilloscope. The current probe saturates at 1 amp rms so a Tektronix Model CT-5 high frequency step-down transformer was mounted around the plasma work coil and was set to a 1000:1 step-down ratio. Tektronix calibrated the transformer and current probe to an accuracy of three percent. A Polaroid camera attachment was used on the cathode ray oscilloscope to record the current trace.
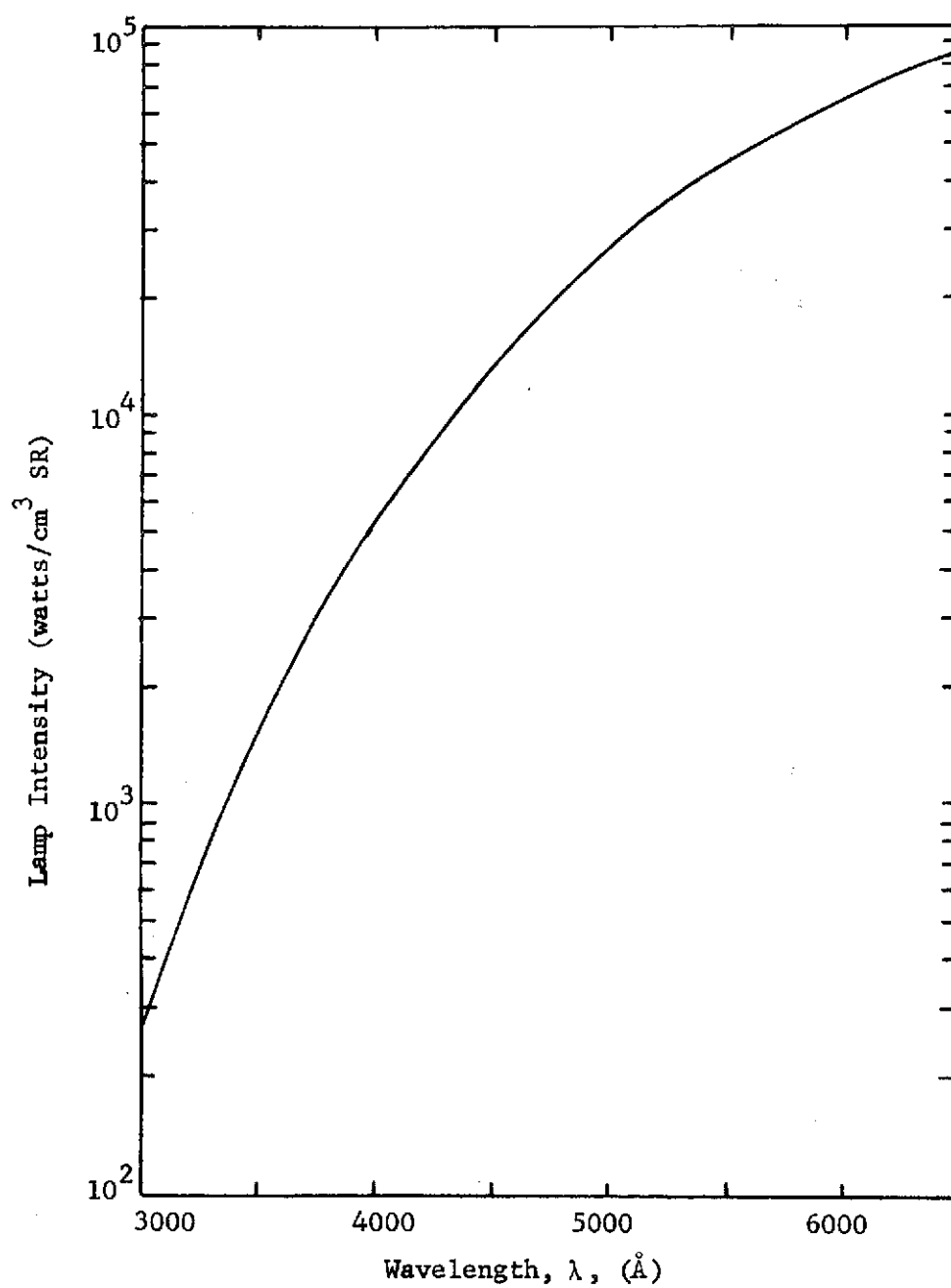
Figure 12. Calibration Lamp Output
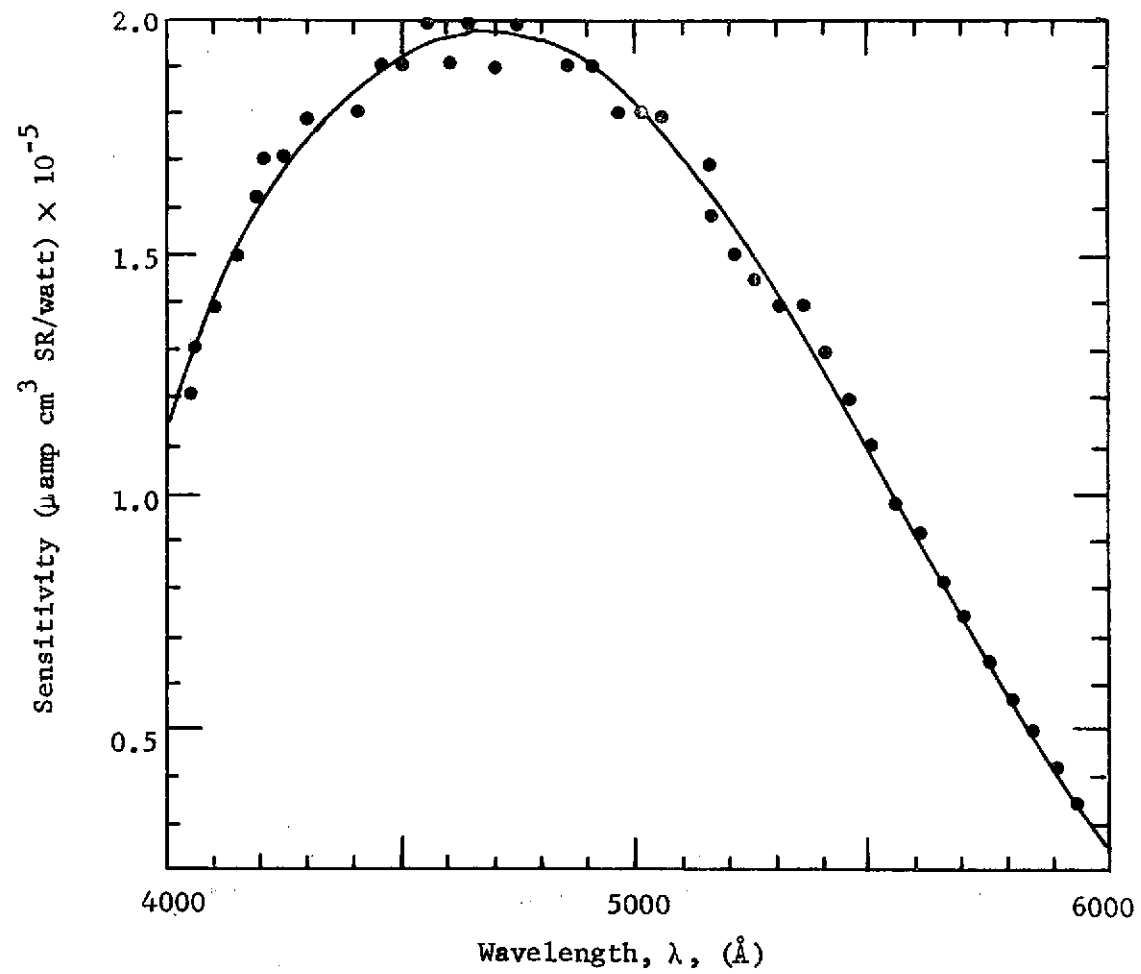
Figure 13. Sensitivity of Plasma Diagnostics System

CHAPTER IV

EXPERIMENTAL PROCEDURE

A typical experimental run consists of from six to ten spatial scans of the plasma at different power settings. The first five scans are generally pure argon. The tungsten generator is turned on and the flow system is adjusted to inject tungsten aerosol into the argon for the remaining scans. The flow is allowed to stabilize and the tungsten flow is not adjusted for the scans of plasma containing tungsten.

A new quartz torch is used for each run since the high power levels required for sustaining a plasma with tungsten aerosol usually destroys or permanently discolors the tube used in the previous run.

The torch assembly is mounted inside the work coil and the gas flow lines are attached. The entire assembly is then checked for gas flow leaks since any air entering the torch will make plasma ignition virtually impossible. New filter papers are dried out, weighed, and inserted in the sample holders.

The new torch is spatially calibrated by setting the scanning monochromator to the helium-neon laser wavelength (6328 Å) and opening the exit slit. The optical path inside the diagnostics room is checked to insure the laser beam is centered on the mirrors and lens and the path it traces during the scan is centered in the rectangular slits of the spatial filters. The position of the laser beam inside the quartz torch is calibrated to the visicorder output of the rotating potentiometer that

is gear mounted to the scanning mechanism and has a small d.c. voltage applied to it.

The diagnostics room equipment is warmed up and the plasma generator start-up procedure is initiated. The plasma start-up check list is given in Appendix B and takes approximately forty minutes to complete. The scanning monochromator is set to the desired continuum wavelength, 4315 Å for most runs, and the slit widths checked at 50 μ. The high voltage to the photomultiplier is increased to 1000 volts.

The plasma is ignited with a d.c. power supply operating at 40 amperes. The plasma generator can only be raised to approximately 4 kW plate discharge power before ignition because the tank circuit is tuned to the impedance of the argon plasma. The rf driver voltage is raised until the tube screen current is near the value for automatic over-current trip-off. An arc is drawn from the welding rod to the grounded water cooled center electrode. The generator power is raised after ignition, and the center electrode is then ungrounded.

The plasma is run for approximately five minutes at a plate discharge power level of approximately 15 kW to allow the amplifier tube to warm up and the quartz torch wall temperature to stabilize.

The plasma is then adjusted to the desired power level and the d.c. plate voltage and current are recorded. The desired picoammeter scale is determined and recorded while observing the center of the plasma. The visicorder is then turned on and the plasma scanned. The current in the work coil is observed on the cathode ray oscilloscope during the scan and the current amplifier is set to scale and recorded. A Polaroid photograph is taken of the sine wave with the scale factor and the run and scan

numbers recorded on the back of the photograph.

The power levels required for the seeded plasma are higher than for the pure argon plasma so the power must be raised during the switch-over to a seeded plasma. The vacuum pump is turned on and a vacuum drawn on the sample tank. The data scans of the seeded plasma are accomplished in the same manner as those of the pure argon. The low power scans are done first and the power raised for each run. At high power levels the tube will discolor. The visicorder plot of each scan is checked and asymmetry of the scan is used as an indication of tube discoloration and thus ends the run.

Two aerosol samples are taken with the plasma running. The vacuum of the sample tank is recorded and the solenoid valve that opens the tank to the flow system is opened for approximately 10 seconds. The valve is then closed and the tank vacuum recorded. A sample is then taken through the remaining filter paper with the solenoid valve open for approximately twenty seconds.

The filter papers are removed and weighed and the aerosol density is calculated from the weight change of the filter papers and the volume of argon drawn into the sample tank.

The visicorder output is cut up into the individual scans and each scan is checked for symmetry. The run and scan number are recorded on the visicorder output. The photographs of the current of the work coil are measured and, based on the amplifier scale, the peak to peak and root mean square currents are calculated and recorded.

The visicorder output with the recorded picoammeter scales serve

as the raw data for the spatially observed intensity profile used in the data analysis section that follows. The calibration of the observed intensity is accomplished with a NBS standard tungsten strip lamp as described in Chapter III. A typical visicorder trace is shown in Chapter V.

CHAPTER V

DATA ANALYSIS

Introduction

There is a wide range of diagnostic methods available to the
experimenter for measuring the electron temperature of a plasma. These
methods fall chiefly into three categories; probes, and the active and
passive uses of electromagnetic radiation. Probes, such as those de-
veloped by Tonks and Langmuir,[50] are historically significant but not
practical for high density plasmas due to deterioration of the probes
and perturbations the probe may introduce. Thompson scattering of pho-
tons by electrons yields information on electron temperature and density
and ion temperature. The cross section for Thompson scattering is so
small that lasers with powers of hundreds of megawatts are required to
overcome the background due to the bremsstrahlung radiation. Passive
methods that involve observation of the emitted radiation include tech-
niques utilizing x-rays, microwaves, and radiation in the visible, infra-
red, and ultraviolet range. Relative intensities of spectral lines, line
shapes, or the intensity of continuum radiation may be employed. Meald
and Wharton[51] give a good general tabulation of useful diagnostic tech-
niques and the temperature and density ranges over which the methods may
be utilized.

The electron temperatures (on the order of 6000-9000°K) and number

densities (10^{21}-10^{22} m^{-3}) of the argon plasma under consideration favor

spectroscopic techniques in the visible range. Equipment requirements

are minimized in the visible range and the emission intensity is high.

The temperature dependence of the absolute continuum emission was chosen

as the basis for electron temperature measurement in favor of several

other available techniques. The chief advantage of this method is the

high degree of dependence the continuum emission coefficient has on tem-

perature in this range, thus minimizing the resulting experimental error

in temperature determination. This technique does require an absolute

calibration of the system.

Methods involving the relative intensities of spectral lines require

only relative calibrations of the optical system but errors are introduced

in the form of experimentally determined atomic transition probabilities

and possible self absorption of lines. These transition probabilities are

readily available,[52,53,54] but the estimated error in some argon lines is

as high as 30%. This technique also requires that two or more spectral

lines at different wavelengths be observed simultaneously while spatially

scanning the plasma. A Boltzmann atomic plot of the natural log of the

relative intensities of many lines versus the upper level electron energy

associated with the transition that leads to each line reduces some of the

errors caused by the uncertainties in transition probabilities. The slope

of a straight line through the data points is a function of temperature.

The accuracy of this method increases with additional lines and with lines

spread over a wide range of electron upper level energies. Unfortunately,

the slope of the line is not highly temperature dependent and, for argon

lines in the visible range a wide range in upper level energies requires

a wide range in the observed spectrum. A Boltzmann plot was made from

observations at the center of the plasma using lines between 4000 Å and

8000 Å with poor results.

The measurement of absolute line intensities also introduces experi-

mental problems. Either the line shape must be determined at many spatial

points with a high resolution spectrometer, or a slit width that introduces

the entire line radiation must be determined and the continuum background

taken into account. Self absorption at the line center may also be a

problem.

The continuum measurements were taken at the 4315 Å wavelength and

checked by comparison with three runs at 5000 Å. A photoelectric trace

of the argon spectrum at an average temperature of 7500°K from 4200 Å to

4400 Å with a tungsten seed density of 18×10^{-6} gm/cc is given in Figure

14 and shows the continuum at 4315 Å to be 15 Å from any argon or tungsten

spectral lines.

Analysis Equations

There are two independent but experimentally inseparable contribu-

tions to the continuum radiation emitted from a plasma in local thermo-

dynamic equilibrium (LTE). Bremsstrahlung (radiation from free-free

transitions) is the result of the Coulomb interaction of unbound electrons

with positive ions. The kinetic energy of the electrons is transformed

into radiation as the electrons are accelerated by the electric and mag-

netic fields present in the plasma. Free-bound (recombination) radiation

is due to the transition of free electrons into bound states; the reverse
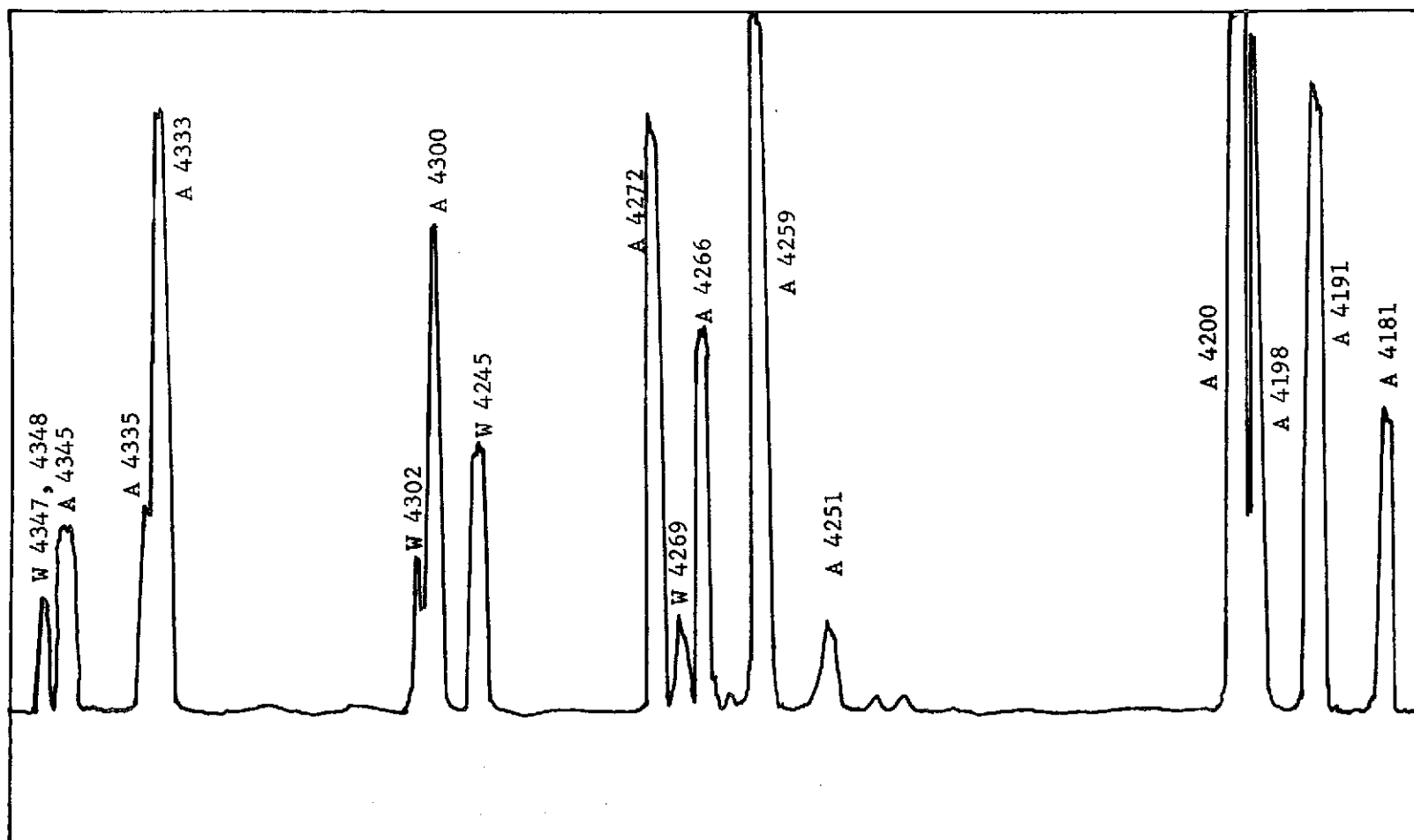
Figure 14. Photoelectric Trace of Tungsten Seeded Argon Spectrum
from 4200 Å to 4400 Å

of photoionization.

Kramers[55] first calculated the emission coefficient due to Brems-strahlung for a Maxwellian electron velocity distribution and a plasma containing only ions of equal charge. The emission coefficient expressed as energy radiated per unit frequency is:

$$\epsilon_\nu^{ff} = \frac{16\pi \; e^6 \; z^2 \; N_e N_i \; G^{ff}}{3c^2 (6\pi mk)^{\frac{1}{2}} \; T^{\frac{1}{2}}} \; \exp\left\{-\frac{h\nu}{kT}\right\} \tag{59}$$

with the quantities defined as follows:

e = electronic charge

z = level of ionization

N_e = number density of electrons

N_i = number density of singly ionized atoms

G^{ff} = free-free Gaunt factor

c = speed of light

m = rest mass of electron

k = Boltzmann constant

T = electron temperature

h = Planck's constant

ν = frequency

The Gaunt factor corrects the semi-classical photoionization cross section for hydrogen like systems to the exact values calculated through wave mechanics. The Gaunt factors, averaged over the Maxwellian electron velocity distribution, have been calculated by Karzas and Latter.[56] The values of the free-free Gaunt factors are of order 1 and are usually taken

to be unity at the lower end of the visible spectrum, since the free-free contribution to the continuum is small compared to the free-bound continuum.

The free-bound emission coefficient for a Maxwellian electron velocity distribution involves a summation of emission coefficients over all possible energy states to which a free electron may undergo transition. Unsöld[57] demonstrated that the summation could be replaced by an integral for frequencies that involved transitions to sufficiently dense levels. Unsöld defines this cut-off frequency ν_g in terms of the energy difference between the ionization potential and the bound state for which higher levels are spaced closely enough to allow integration. The emission coefficient for a one-electron system at frequencies below ν_g is:

$$\nu \leq \nu_g \qquad \epsilon_\nu^{fb} = \frac{16\pi^2 e^6 z^2 N_e N_i}{3c^2 (6\pi mk)^{\frac{1}{2}} T^{\frac{1}{2}}} \left\{ 1 - \exp\left(-\frac{h\nu}{kT}\right) \right\} \tag{60}$$

Biberman et al.[58,59] corrected the emission coefficient for other hydrogen-like gases by introducing a correction factor $\xi(T,\nu)$ or $\xi(T,\lambda)$.

$$\nu \leq \nu_g \qquad \epsilon_\nu^{fb} = \frac{16\pi e^6 z^2 N_e N_i g_{z,1}}{3c^3 (6\pi mk)^{\frac{1}{2}} T^{\frac{1}{2}} u_z} \left\{ 1 - \exp\left(-\frac{h\nu}{kT}\right) \right\} \xi(T,\nu) \tag{61}$$

where $g_{z,1}$ is the statistical weight of the ground state of the singly ionized atom and u_z is the partition function of the singly ionized atom defined by:

$$u_z(T) = \sum_{s=1}^{n} g_{z,s} e^{-\frac{E_{z,s}}{kT}} \tag{62}$$

Bauder[60] used a cut-off frequency of $\nu_g = 9.5 \times 10^{14}$ sec^{-1}, corresponding to a wavelength of $\lambda = 3160$ Å in his work on high density d.c. plasma arcs. Schlüter[61,62] has calculated ξ factors for argon which are nearly temperature independent below 14,000°K.

The total continuum emission coefficient is then the sum of ϵ_ν^{fb} and ϵ_ν^{ff}. Taking the free-free Gaunt factor to be unity and expressing the emission coefficient as energy radiated per unit wavelength by multiplying equations (59) and (61) by c/λ^2 we have:

$$\epsilon_\lambda = \frac{16\pi \, e^6 \, z^2 \, N_e N_i}{3c^2 (6\pi mk)^{\frac{1}{2}} \, T^{\frac{1}{2}} \lambda^2} \left[\frac{g_{z,1}}{u_z} (1 - \exp^{-\alpha}) \, \xi(\lambda,T) + \exp^{-\alpha} \right] \qquad (63)$$

where

$$\alpha = \frac{h\nu}{kT} = \frac{hc}{\lambda kT}$$

Evaluating the constants in equation (63) and using the data from Drawin and Felenbok[34] for the statistical weight $(g_{z,1} = 6)$ and partition function $(u_z(T) = 5.519)$ for argon over the temperature range of interest, equation (63) becomes (for ϵ_λ in $\frac{\text{watts}}{\text{ster. cm}^4}$):

$$\lambda > 3160 \text{ Å} \qquad \epsilon_\lambda = 1.65 \times 10^{-19} \frac{N_e N_i}{\lambda^2 \sqrt{T}} \left[\frac{6\xi(\lambda,T)}{5.519} (1 - e^{-\alpha}) + e^{-\alpha} \right] \qquad (64)$$

where

N_e = electron number density, cm^{-3}

N_i = singly ionized number density, cm^{-3}

T = electron temperature, °K

λ = continuum wavelength, Å

The number density of the electrons is equal to that of the singly ionized atoms below approximately 20,000°K and can be calculated from the Saha relation, equation (53) in Chapter II.

The neutral particle number density can be approximated from the ideal gas law for slightly ionized argon by

$$P = N_o \, R \, T \tag{65}$$

where R is the universal gas constant and P is the pressure which is very nearly 1 atmosphere pressure in the plasma.

The number densities for argon neutrals, singly ionized atoms, and electrons at one atmosphere are given in Figure 15 as a function of temperature as calculated from equations (53) and (65). The continuum emission coefficient as a function of temperature given by equation (64) for argon at 4300 Å and one atmosphere is plotted in Figure 16.

The assumption of local thermodynamic equilibrium (LTE) requires that the population densities of the electrons be determined exclusively by particle collisions and that all species have a Maxwellian velocity distribution at the same temperature. For bound levels, the distributions are given by the Boltzmann and Saha equations. Griem[63] presents a criterion for LTE based on a collisional rate which is ten times larger than the radiative transition rate. If we apply this validity criterion estimate to the experimental conditions present in this work, we find that electron densities of about $5 \times 10^{22} \, m^{-3}$ are required which makes the LTE assumption
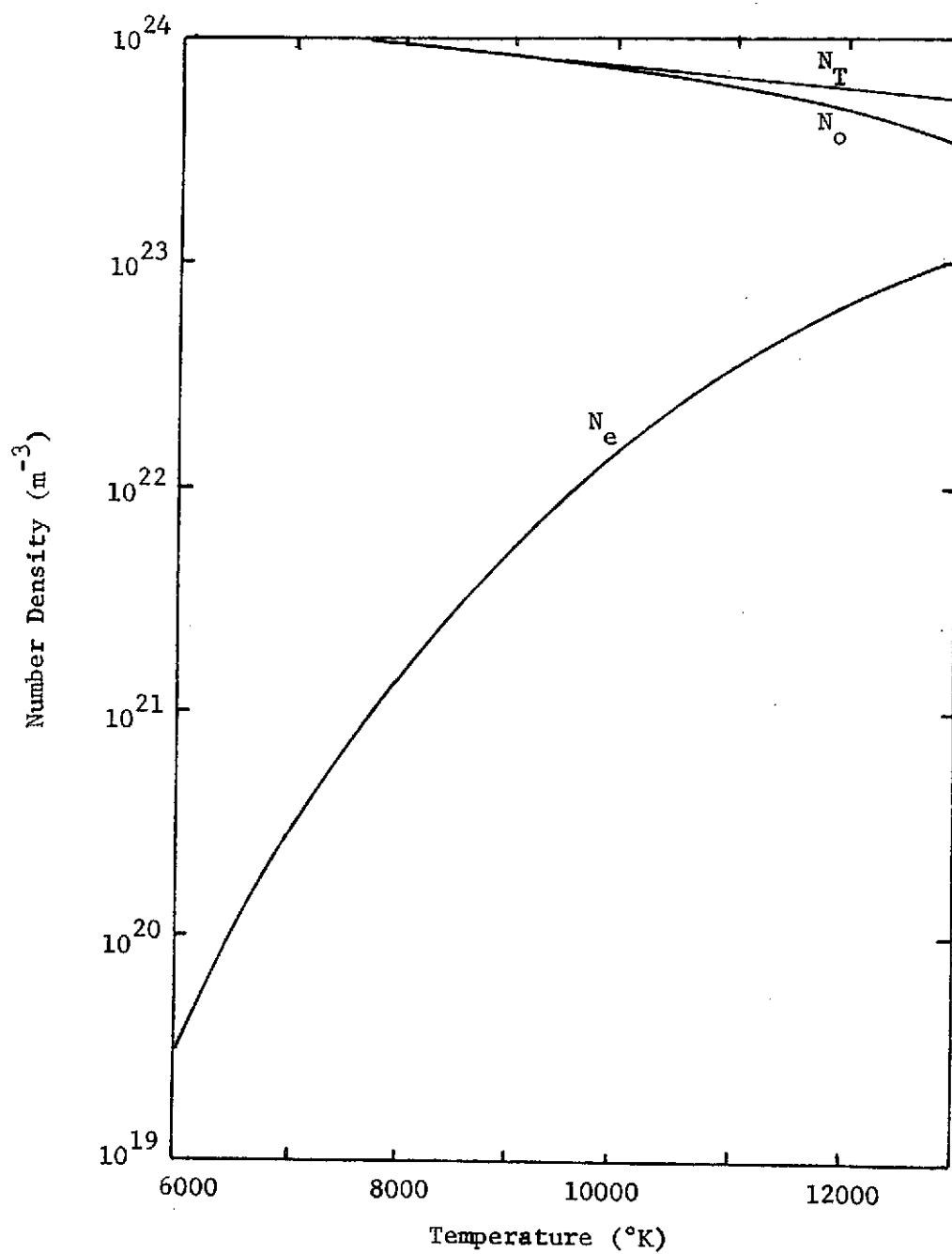
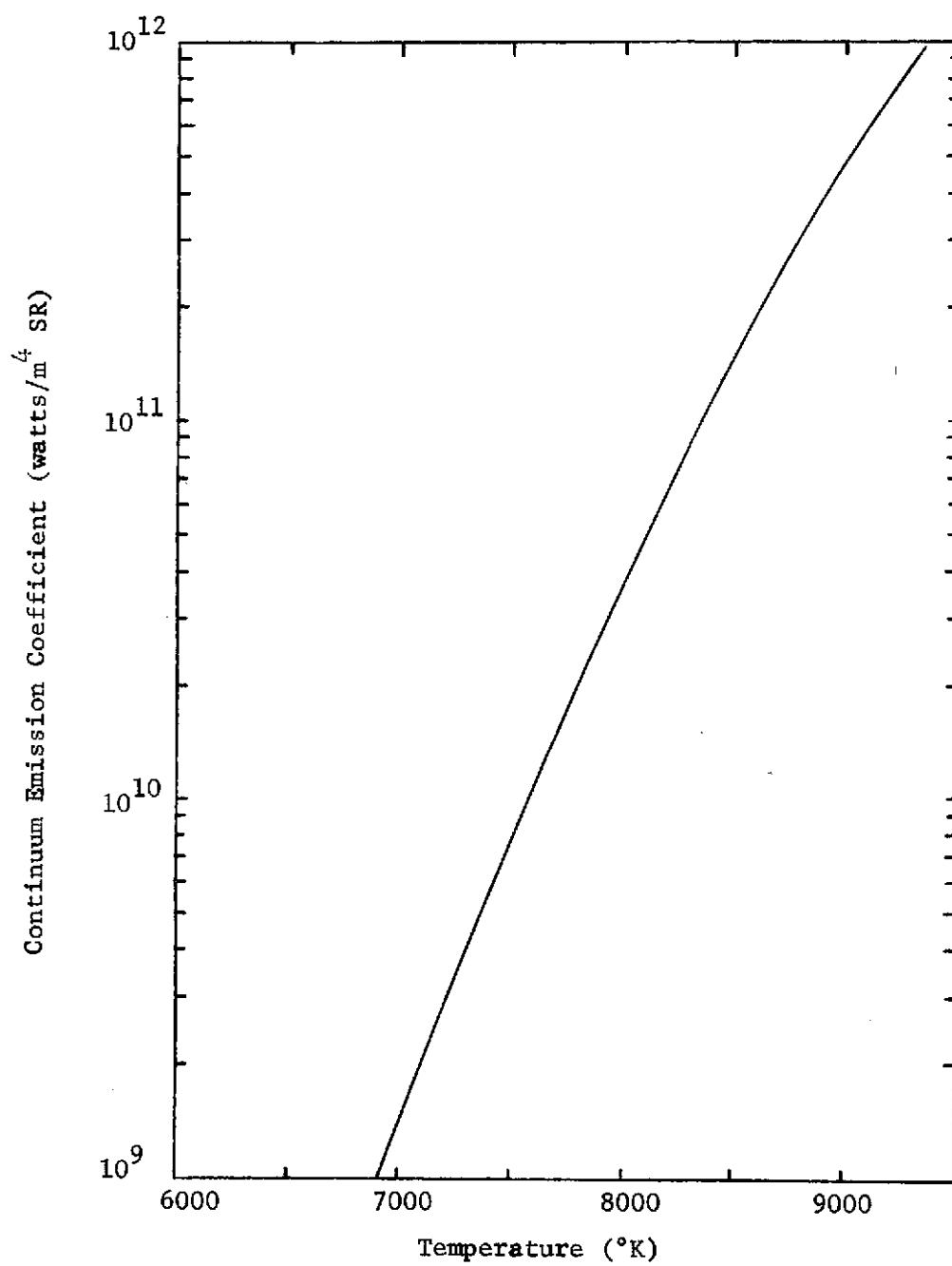Figure 15. Number Density of Argon Plasma Species at One Atmosphere

Figure 16. Argon Continuum Emission Coefficient at 4315 Å

suspect below about 11,000°K. Shumaker and Popenoe[64] used a wall stabil-

ized arc for studies of equilibrium in argon and concluded that departures

from LTE occur at electron densities below 5×10^{22} m^{-3}. Their data in-

cluded no correction for self-absorption of the lines studied. Olsen[65]

used an argon arc burning freely between cooled metal electrodes to com-

pare temperatures determined from measured emission coefficients of three

species of plasma radiation and concluded that his atmospheric pressure

plasma was in LTE at a temperature of 10,000°K. He states that "Discrep-

ancies between temperatures determined from atom and ion line intensities

have been shown to have been caused by self-absorption of the atom line

in the outer layers of the plasma."

Work on rf argon plasmas by Scholz and Anderson[5] indicates that an

rf plasma may be in LTE at much lower number densities than a d.c. arc

because of the larger plasma radii and lower axial and radial temperature

gradients present. Shumaker and Popenoe[64] discussed the relevance of

plasma diameter and temperature gradients in their report on d.c. arc

studies.

> By comparing an arc with a black body in which complete LTE
> exists one can recognize three essential differences which may
> cause departures from equilibrium. First, in the arc much of
> the radiation escapes so that LTE will be achieved only if radi-
> ative depopulation rates are negligible compared to rates of
> collisional population and depopulation. Second, in the arc
> steep temperature and number density gradients exist which may
> generate diffusional fluxes of such magnitude that collisional
> (and radiative) processes are unable to maintain equilibrium
> distributions. And third, since electrons absorb energy from an
> electric field much more rapidly than ions do the kinetic tem-
> perature of the electron gas will be higher than that of the
> heavy particle gas which obtains its energy then mainly by col-
> lisions with the electrons. Since collisional processes will
> be dominated by electron collisions it turns out that all of

these effects should decrease rapidly in importance with increasing electron density . . .. The importance of the second effect should also depend upon arc channel diameter and radial position in the arc.[64]

Scholz and Anderson[5] investigated LTE in an rf argon plasma operating at 4.2 MHZ at pressures of 0.01, 0.1, 0.5, and 1.0 atmosphere. They used four emission lines and the continuum centered at three different wavelengths to show that the central core of the rf argon plasma was in LTE at 1.0 and 0.5 atm and very nearly so at 0.1 atm. They state that this

. . . equilibrium is due in part to the existence of low (i.e. $|\nabla T| \leq 530°K/cm$) axial and radial temperature gradients. At these pressures the plasma is in an apparent state of LTE and the thermal limit extends down to the ground state. The LTE electron number density criterion given by equation (1) [Griem] appears to be conservative for this plasma.[11]

The problem of relating the radial emission coefficient to the observed intensity profile is simply a geometric one for optically thin plasmas and the standard Abel inversion technique may be used. The problem is more difficult when reabsorption inside the plasma cannot be neglected. Griem[60] suggested a self-consistent iterative procedure for obtaining emission coefficients in the case of moderate optical depths.

The absorption coefficient is defined by:

$$\kappa(\lambda,T) = \frac{\epsilon(\lambda,T)}{B(\lambda,T)} \tag{66}$$

where $B(\lambda,T)$ is the blackbody radiation.

The plasma is assumed axially symmetric and divided into N zones of radii R/N, $2R/N$, . . ., and R as indicated in Figure 17. The tempera-
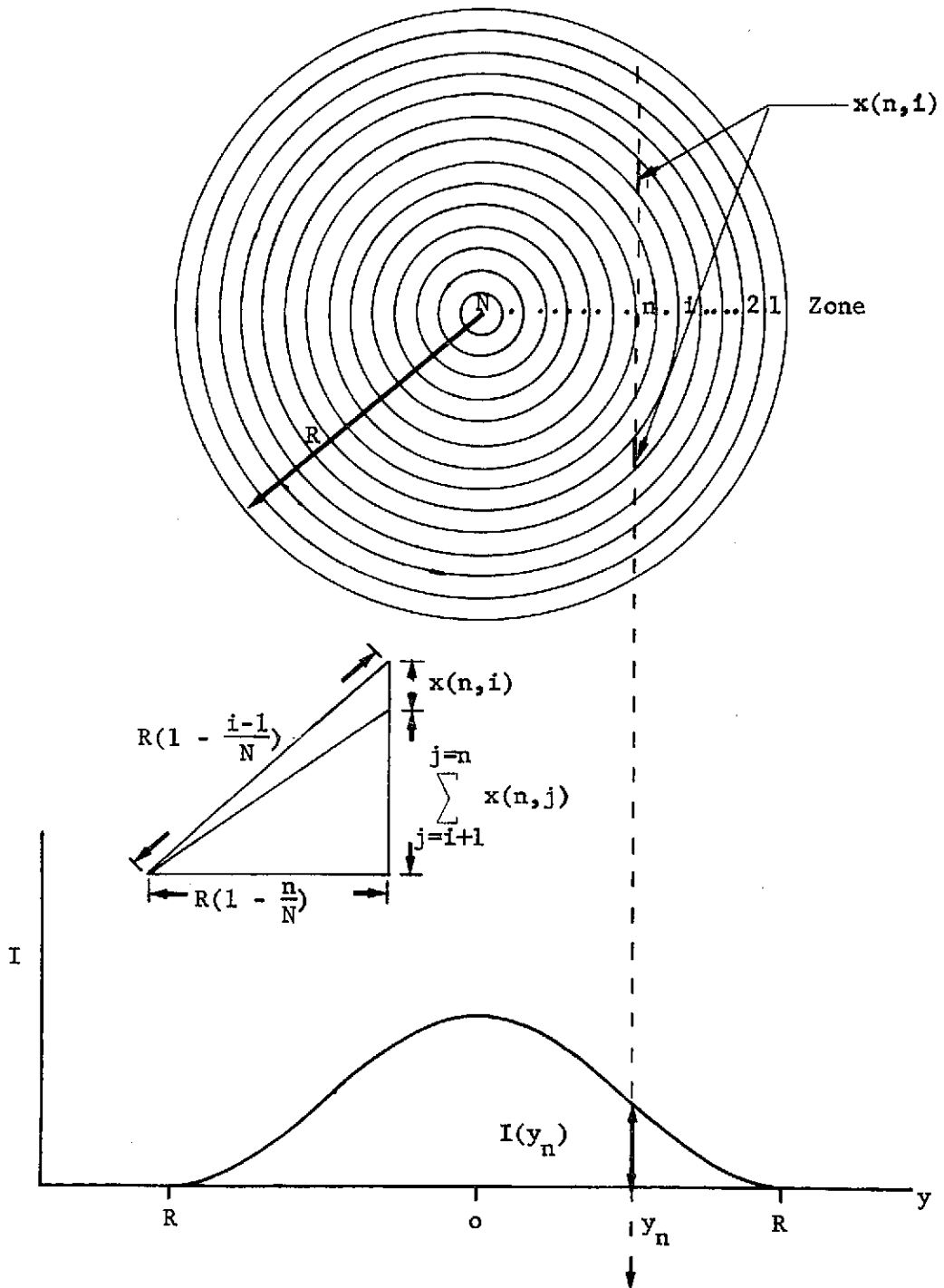
Figure 17. Plasma Geometry for Computer Program

ture, emission coefficient, and absorption coefficient are considered constant in a given zone. The reduction in intensity of radiation I_o after passing through a zone of constant $K(\lambda,T)$ and distance x is given by:

$$I = I_o \, e^{-Kx} \tag{67}$$

If that zone is also emitting radiation with the same emission coefficient throughout that zone, the observed intensity will be:

$$I = I_o \, e^{-Kx} + \int_o^x \epsilon \, e^{-K(x-\xi)} \, d\xi \tag{68}$$

or

$$I = I_o \, e^{-Kx} + \frac{\epsilon}{K} [1 - e^{-Kx}] \tag{69}$$

The intensity of the radiation observed at a given spatial position, y_n, as shown in Figure 17, is the sum of the radiation emitted from each zone minus the radiation attenuated by the zones between each emitting zone and the surface.

A computer program was written to relate the emission coefficient, absorption coefficient, and temperature of each zone to the observed intensity of the radiation emitted from the surface of the plasma.

Computer Program — MAD

The computer program, MAD (Modified Abel Diagnostic code), utilizes the spatially observed surface radiation intensity as raw data fed in at N discrete points according to Figure 17. The program calculates the radi-

ally dependent temperature, emission coefficient, and absorption coefficient for a plasma that is not optically thin. A typical visicorder trace, as shown in Figure 18, is reduced to give values of the observed radiation in watts/sec m^3 based on the output current of the photomultiplier tube and the calibrated sensitivity of the system. The radius of the plasma is found from the radiation intensity trace and the spatial position trace. The radius is assumed to be that position where the intensity drops to zero.

The data fed in are first curve fitted with a third order spline fit subroutine and interpolated to give observed intensity values for N zones. The program then calculates values of $x(n,i)$, which is the thickness of zone i when observed at chordal position y_n, shown in Figure 17. This distance is

$$x(n,i) = R\left[\left(1 - \frac{i-1}{N}\right)^2 - \left(1 - \frac{n}{N}\right)^2\right]^{\frac{1}{2}} - \sum_{j=i+1}^{n} x(n,j) \qquad (70)$$

During the first iteration, the emission coefficients are calculated for each zone from the observed intensity $I(y_n)$ and the values of $x(n,i)$, assuming the plasma to be optically thin, i.e., the absorption coefficient K is set equal to zero for all zones. Starting from zone one and working toward the center, the emission coefficient of each zone is calculated using the emission coefficients of previously calculated zones from:

$$I(y_n) = 2 \sum_{i=1}^{n} \varepsilon(i) \, x(n,i) \qquad (71)$$
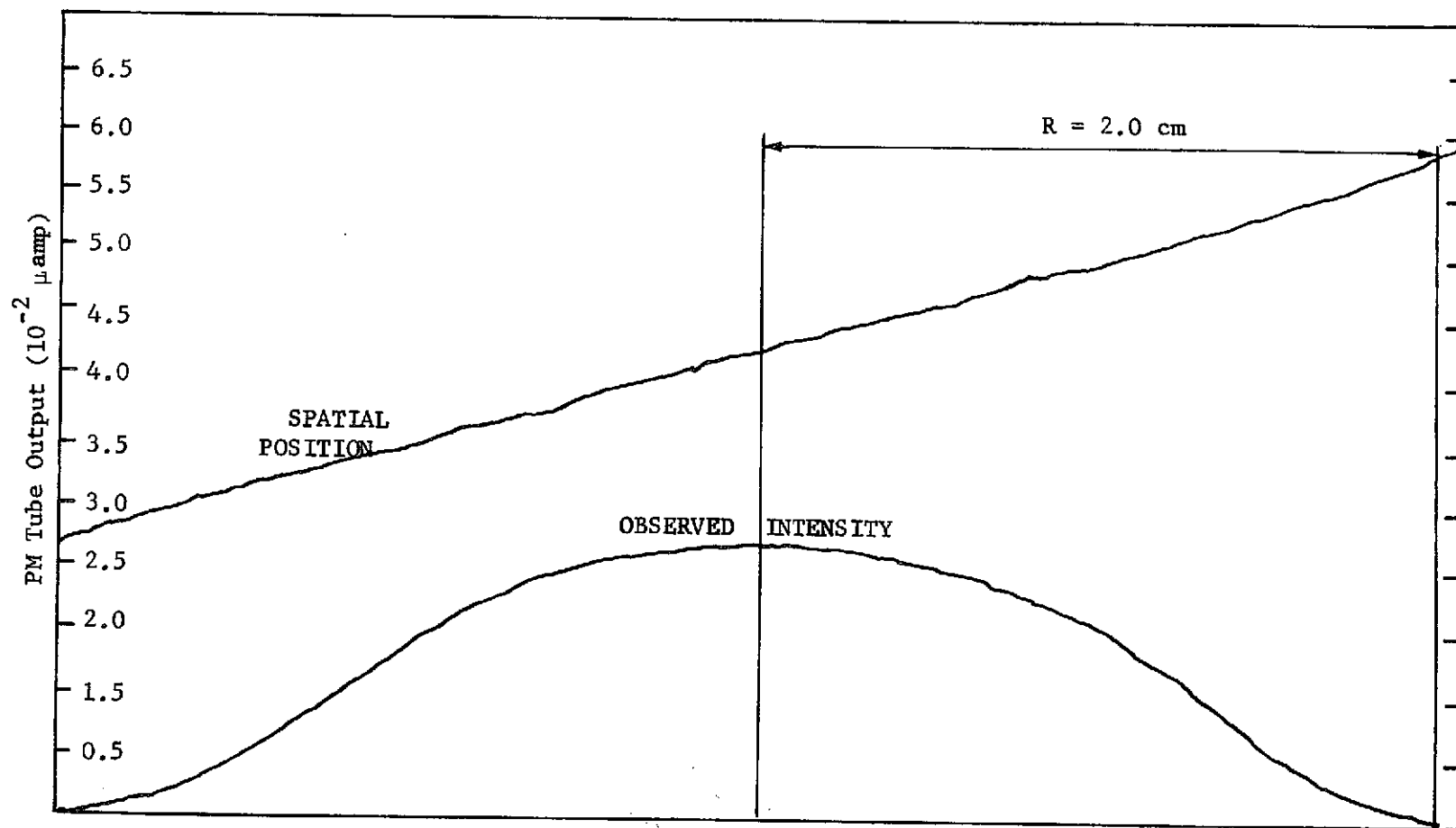
Figure 18.   Photoelectric Trace of Observed Intensity vs. Spatial Position

or

$$\epsilon(n) = \left[I(y_n) - 2 \sum_{i=1}^{n-1} \epsilon(i) \, x(n,i) \right] \frac{1}{2x(n,n)} \qquad (72)$$

where $\epsilon(i)$ for $i < n$ have been calculated previously.

The temperature and number density for each zone can be calculated from the emission coefficient and equations (53), (64), and (65). Values for the number density are interpolated from data given by Olsen's GASCOMP program using an $N = aT^{5/4} \exp^{b/T}$ dependence between values 1000°K apart. The a and b coefficients are calculated for each 1000°K interval and the error is less than one percent over the temperature range of 4000-14,000°K. The correct temperature and number density for a given emission coefficient are then arrived at by binary search iterative procedure. The first approximation of the absorption coefficient is calculated by dividing the emission coefficient by the blackbody radiation at the temperature of the given zone as indicated by equation (66).

After the first iteration, a new set of emission coefficients is calculated based on the observed intensity data and the first approximation to the absorption coefficients. Equation (71) is modified to include the absorption coefficients:

$$I(y_n) = \sum_{i=1}^{n} \left\{ \frac{\epsilon(i)}{\kappa(i)} [1 - \exp(-\kappa(i) \, x(n,i))] \left\{ \exp \left(\sum_{j=1}^{i-1} -\kappa(j) \, x(n,j) \right) \right.\right. \qquad (73)$$

$$\left.\left. + \exp \left(\sum_{j=1}^{n} -\kappa(j) \, x(n,j) + \sum_{j=i+1}^{n} -\kappa(j) \, x(n,j) \right) \right\}\right\}$$

This calculation is best accomplished on the computer by defining
a set of optical arrays based on equations (67) and (69). Let $\epsilon(i)A(n,i)$
represent the emission from a zone of length $x(n,i)$ and constant emission
coefficient $\epsilon(i)$ and absorption coefficient $K(i)$. From equation (69)

$$A(n,i) \equiv \frac{1}{K(i)} \left[1 - \exp(-K(i)\, x(n,i)) \right] \tag{74}$$

Defining $B(n,i)$ as:

$$B(n,i) = -K(i)\, x(n,i) \tag{75}$$

then $\exp B(n,i)$ represents the attenuation of radiant energy passing
through a zone of length $x(n,i)$ according to equation (67).

Arrays $C(n,i)$ and $D(n,i)$ are defined in terms of sums of $B(n,i)$
such that $\exp C(n,i)$ represents the total attenuating power of all of the
zones between the zone emitting radiation $\epsilon(i)A(n,i)$ and the surface for
zones on the near side of the plasma, and $\exp D(n,i)$ represents the equiv-
alent for zones on the far side of the plasma:

$$C(n,i) = \sum_{j=1}^{i-1} B(n,j) \tag{76}$$

$$D(n,i) = \sum_{j=1}^{n} B(n,j) + \sum_{j=i+1}^{n} B(n,j) \tag{77}$$

Now the radiation emitted from zone i and along chordal position n is

$$I = \epsilon(i)A(n,i) \tag{78}$$

The radiation from this zone reaching the surface is then

$$I = \epsilon(i)A(n,i) \ \exp \ (C(n,i)) \tag{79}$$

for zones on the near side of the plasma and

$$I = \epsilon(i)A(n,i) \ \exp \ (D(n,i)) \tag{80}$$

for zones on the far side of the plasma. Equation (73) then reduces to:

$$I(y_n) = \sum_{i=1}^{n} \epsilon(i)A(n,i) \ [\exp \ (C(n,i) + \exp \ (D(n,i)))] \tag{81}$$

The emission coefficients can then be calculated starting from zone 1 and proceeding inward by:

$$\epsilon(n) = \frac{I(y_n) - \displaystyle\sum_{i=1}^{n-1} \epsilon(i)A(n,i) \ [\exp \ (C(n,i)) + \exp \ (D(n,i))]}{A(n,n) \ [\exp \ (C(n,n)) + \exp \ (D(n,n))]} \tag{82}$$

where $\epsilon(i)$ for $i < n$ have been calculated previously.

These new emission coefficients are used to calculate new temperatures and absorption coefficients. The iteration terminates when the

changes in emission coefficients, absorption coefficients, and temperatures for all zones are less than one percent of the values in the previous iteration.

This analysis provides a self-consistent radial distribution of temperature, emission coefficient, and absorption coefficient for the distribution of the observed intensity for moderately self-absorbing plasmas.

A listing of the program is given in Appendix C.

Error Analysis

Chordal Average Temperature

The experimental errors associated with the temperature measurements are small compared with the experimental magnetic field intensity measurements because of the high temperature dependence of the emission coefficient. If we define a chordal average temperature as the equally weighted sum of the temperature of each zone divided by the number of zones, and the chordal average emission coefficient as the value of the emission coefficient determined by that temperature, the chordal average emission coefficient multiplied by the plasma diameter will yield the value of the emitted intensity, $I(y_c)$, along a chord through the center of the plasma.

It is estimated that the photoelectric trace of the observed intensity can be read within 10% and the sensitivity of the system as shown in Figure 13 is known within 15% giving a total uncertainty in the observed intensity of 25%. The absorption coefficient is neglected in estimating the error in measured chordal average temperatures since the theory and experiment show the plasma is optically thin. The uncertainty in observed intensity results in an uncertainty in the average emission coefficient

of the same value since

$$\overline{\epsilon} = I(y_c)/R \tag{83}$$

so

$$\Delta\overline{\epsilon} = \frac{2\overline{\epsilon}}{2I_c} \Delta I_c = \Delta I_c/R \tag{84}$$

and

$$\frac{\Delta\overline{\epsilon}}{\overline{\epsilon}} = \frac{\Delta I_c}{R\overline{\epsilon}} = \frac{\Delta I_c}{I_c} \tag{85}$$

The uncertainty in the chordal average temperature can be esti-

mated from the observed intensity error by

$$\frac{\Delta T}{T} = \frac{\frac{\partial T}{\partial z} \Delta\overline{\epsilon}}{T} = \frac{\frac{\partial T}{\partial z} \overline{\epsilon} \Delta I_c}{T I_c} \tag{86}$$

The values of $\overline{\epsilon}$ and $\frac{\partial\overline{\epsilon}}{\partial T}$ as functions of temperature can be obtained

from equation (64) or estimated from Figure 16. Over the temperature

range of $7000°K \leq T \leq 9500°K$, a 25% uncertainty in observed intensity re-

sults in a chordal average temperature uncertainty of less than 2%. The

uncertainty in experimentally measured chordal average temperatures is

much less than that of the experimentally measured magnetic field inten-

sity. Thus, only the error bars associated with the magnetic field inten-

sity measurements are shown in the results section.

Magnetic Field Intensity

The Tektronix high frequency current probe, amplifier, and step

down transformer are calibrated to within 3%. It is estimated that the

magnetic field intensity can be calculated from the coil current to within an accuracy of 2% based on the experimental measurements reported in Appendix A. The current recorded from the photographs of the trace on the oscilloscope is estimated to be correct within 10%, giving a total uncertainty in the reported magnetic field intensity of 15%.

Tungsten Aerosol Density

The tungsten aerosol density was measured twice during each experimental run and the uncertainty in the reported density is estimated to be 20%, based on the average discrepancies in measured values.

CHAPTER VI

RESULTS

Introduction

A total of 59 experimental runs resulting in temperature profiles were made. Approximately 50 more runs were made that did not yield results due to equipment failure. The failure was most often in the plasma generating equipment.

The first 27 runs were made without measurement of the coil current in order to develop a degree of confidence in the plasma generator and the diagnostics instrumentation. Three runs were made using the continuum at 5000 Å and at 4315 Å to ensure that the resulting temperature profiles were not dependent on the continuum wavelength chosen. The plasma spectrum was recorded from 3500-8000 Å and analyzed to ensure that no unknown contaminants were in the plasma. Twelve of these first 27 runs included various concentrations of tungsten aerosols ranging in number density ratios N_w/N_{Ar} from 2.5 x 10^{-3} to 3.7 x 10^{-2} to ensure that the effect of tungsten could be measured and to gain experience in operating the plasma generator with a seeded plasma. High speed, 16 mm motion pictures of the plasma were made at 1000 frames/sec to check for instabilities in the plasma that might not be observable to the naked eye. A small pulsation of the plasma at a frequency of 60 Hz could be detected which caused a variation in the plasma radius of about 10%. This resulted from the 60 Hz

ripple in the coil current from the rectifier circuit.

There were 32 runs made with temperature profiles recorded at various power levels. The coil current was measured along with the plate dissipation power. Eleven of these runs were made with tungsten to argon number density ratios of 4.3×10^{-3}, 6.1×10^{-3}, and 3.6×10^{-2}.

Experimental Results

Argon

The observed intensity for four representative runs at magnetic field intensities of 33.1, 46.0, 55.2, and 77.2 amp-turns/cm are illustrated in Figure 19. Figure 20 is a plot of the resulting radial distributions of the calculated emission coefficients. The absorption coefficients were also calculated in the analysis and ranged from about 10^{-6} cm^{-1} for the low power case to 2×10^{-5} cm^{-1} for the highest power case, indicating that the plasma was optically thin.

The temperature profiles that result from the radial emission coefficients are presented in Figure 21. While the observed intensity ranged over an order of magnitude for the various power levels, the resulting temperature profiles varied only about 10% from the lowest power case to the highest. This is due to the very high temperature dependence of the emission coefficient.

The four temperature profiles presented in Figure 21 are compared with the theoretical analyses in Figure 22. The solid line indicates the experimental results; the dotted and dashed lines represent the numerical results described in Chapter II. The plasma radius was reduced in one case to the experimentally observed radius and the thermal con-

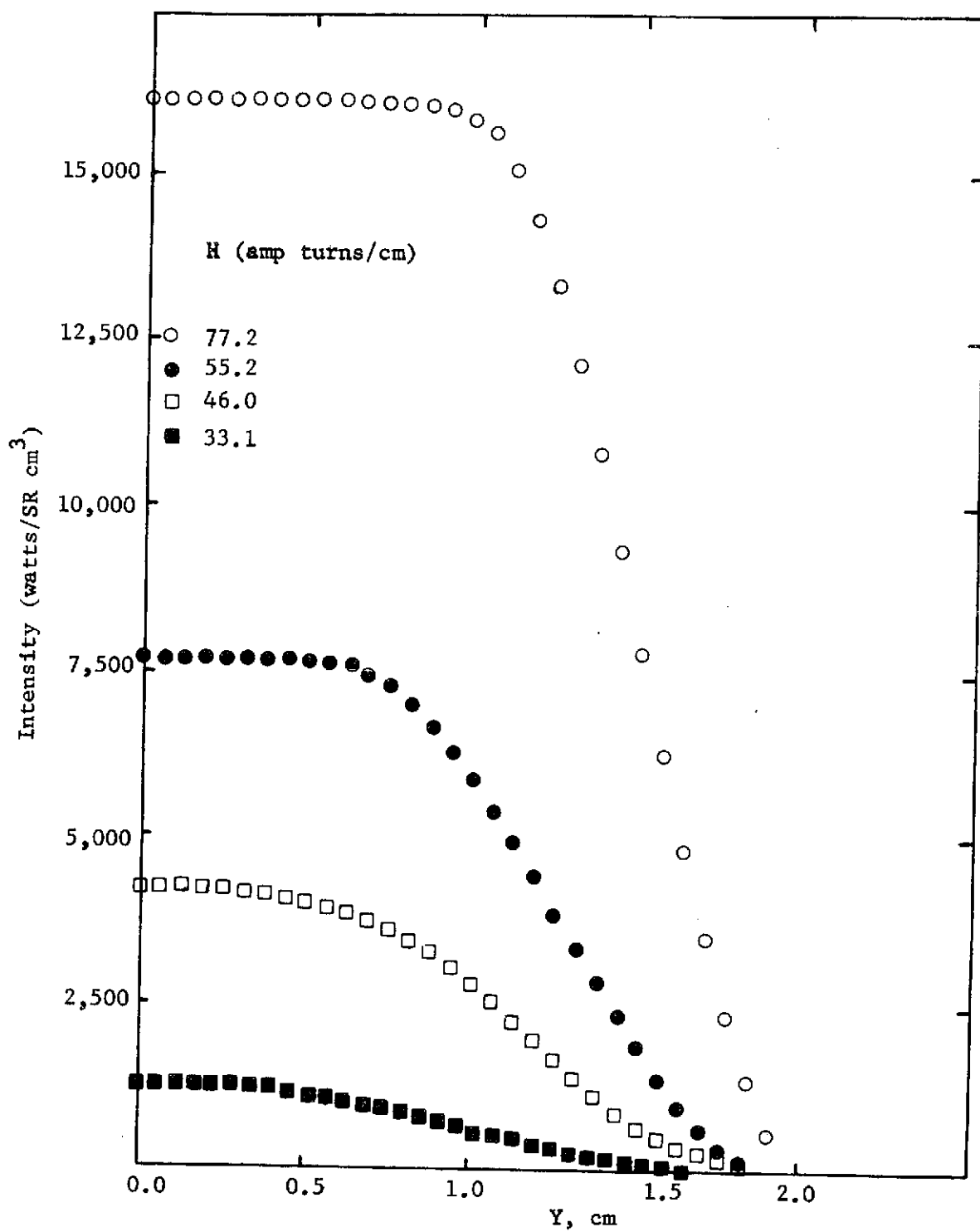Figure 19. Observed Intensity Profiles for Four Representative
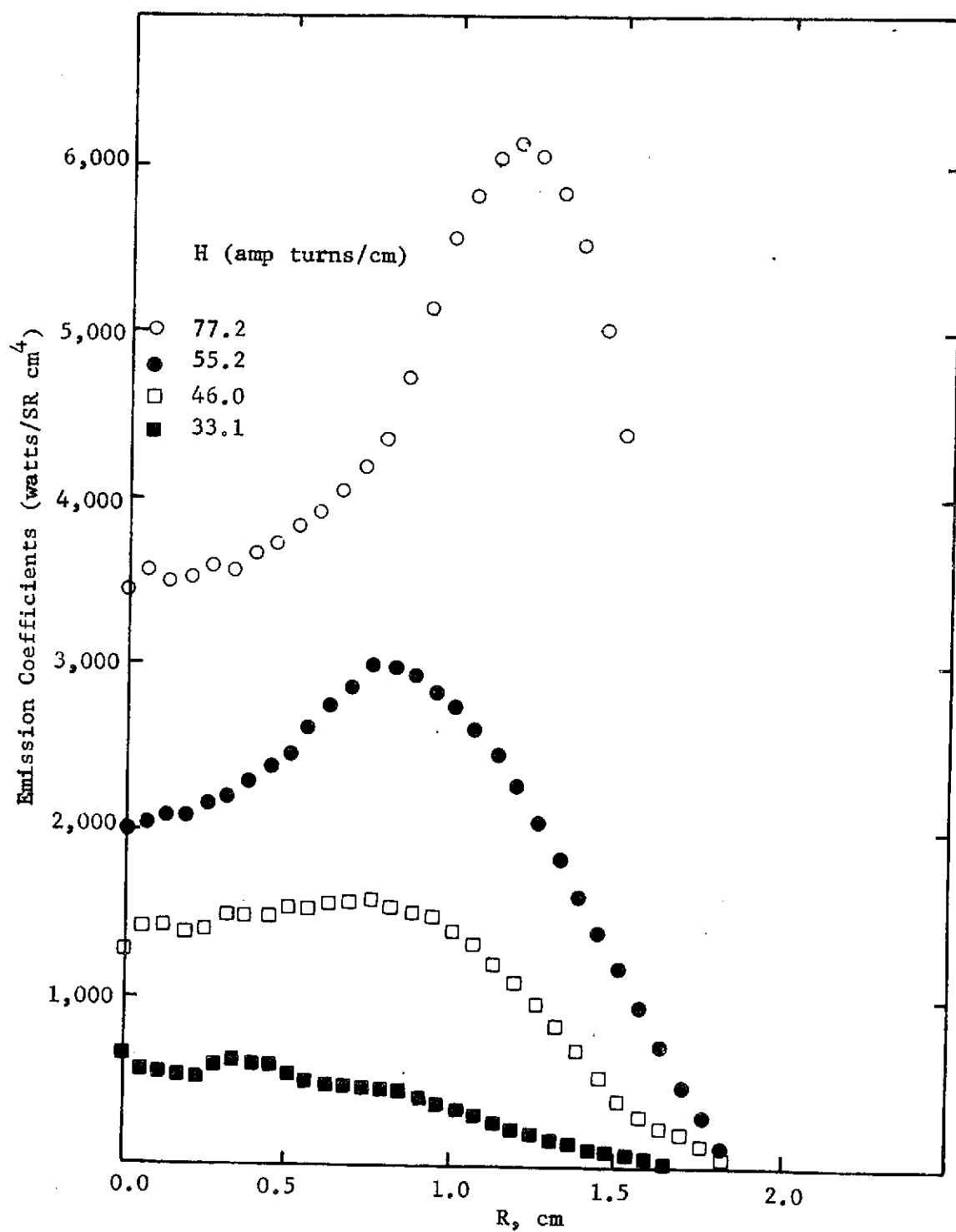Magnetic Field Intensities

Figure 20. Calculated Emission Coefficient Profiles for Four
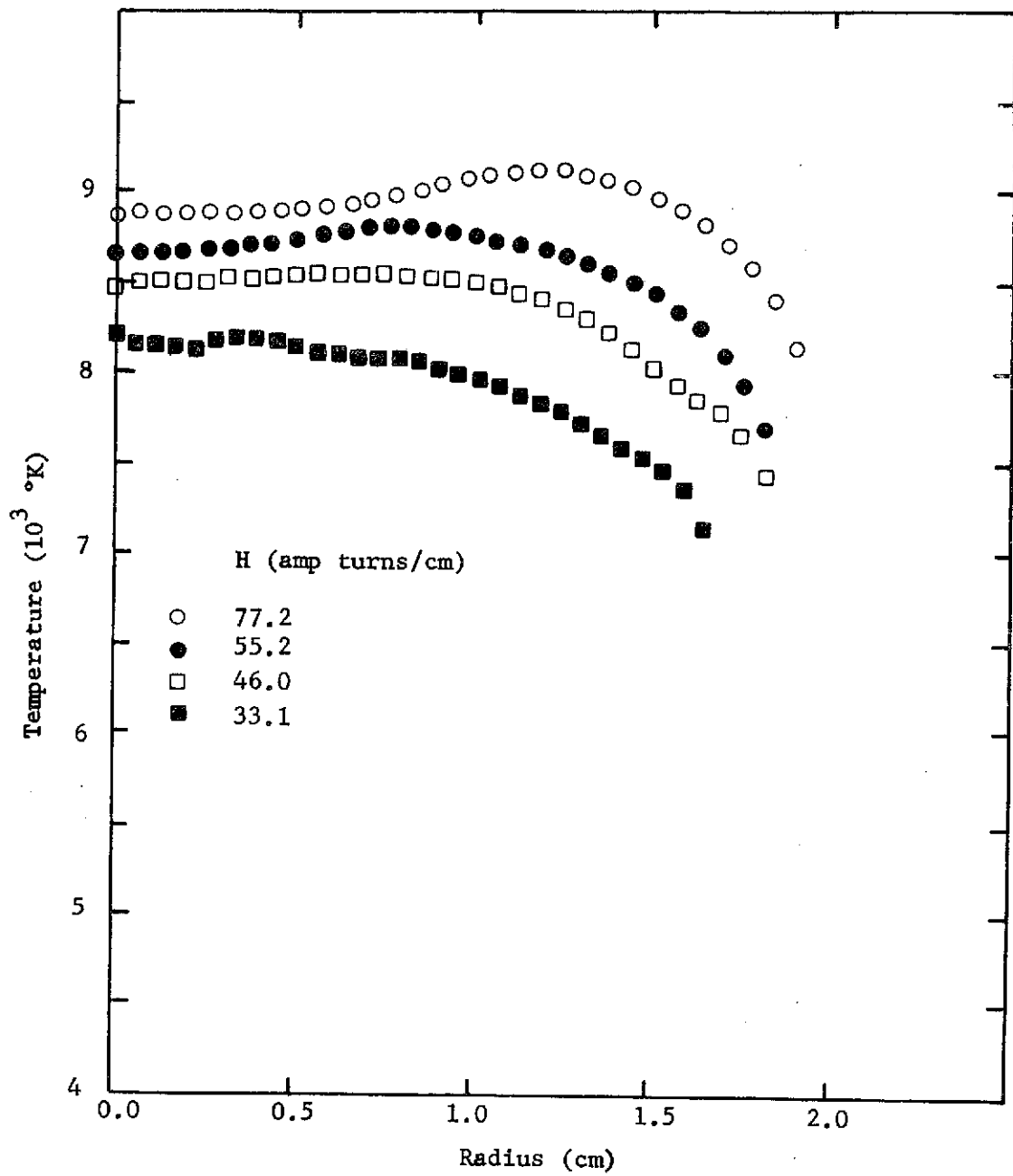Representative Magnetic Field Intensities

Figure 21. Experimental Temperature Profiles for Four Representative
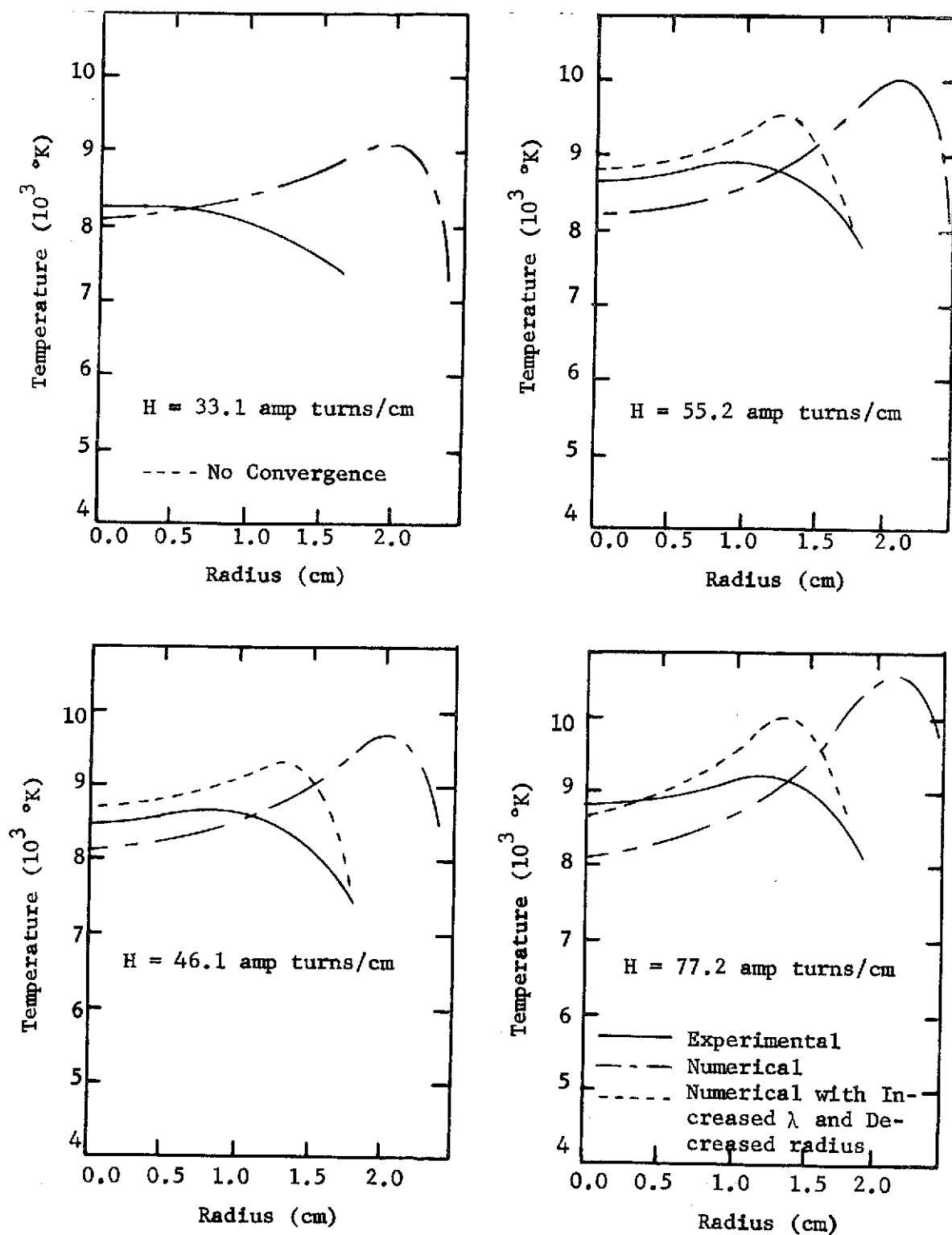Magnetic Field Intensities

Figure 22. Comparison of Experimental and Theoretical Temperature Profiles for Four Representative Magnetic Field Intensities

ductivity increased as explained later. The off-center peak temperature
of the numerical analysis is much more pronounced than the results of the
experiment. The off-center maximum of the temperature profile is a result
of the skin heating by the electromagnetic field and radiation cooling of
the plasma. When radiation is neglected, the numerical analysis yields a
temperature profile with the maximum temperature occurring at the center
of the plasma. The experimental results also have an off-center tempera-
ture peak but the difference between the center temperature and the peak
temperature is much less than predicted by theory. This is in keeping
with the results of other experimenters as shown in Chapter I. The most
probable reason for this is the complex turbulent flow pattern present
in the experimental plasma that is not accounted for in the theoretical
analysis. This turbulent mixing flow will tend to flatten out the tem-
perature profile. Neglecting axial convection in the numerical analyses
may also account for the difference since the axial temperature gradient
will be highest at the radial position where the peak temperature occurs,
tending to flatten the temperature profile. The magnetic field intensity
is increasing at the axial point, where the plasma was observed, as shown
in Figure 33 of Appendix A, and the peak temperature increases with in-
creasing magnetic field intensity. An approximate analysis was made with
an assumed axial temperature gradient calculated from the derivative of the
applied magnetic field intensity and the change in the radially dependent
temperature with applied magnetic field intensity as predicted by the nu-
merical analysis. This analysis shows that the correction term is an order
of magnitude lower than the radiation term. This is not in agreement with

the theoretical predictions of Miller and Ayen.[21] Their two-dimensional analysis of temperature profiles in a torch with an assumed flat axial flow shows a definite flattening of the temperature profiles at the beginning of the energy addition region and a gradual increasing of the off-center maximum temperature at increasing axial positions.

The effect of the turbulence is to increase the effective thermal conductivity. The numerical analysis shows a marked decrease in magnetic field intensity near the tube wall while it appears that the vortex flow decreases the radius of the plasma, thus delaying the drop in magnetic field values. The numerical analysis was run with the thermal conductivity values doubled and the radius reduced to match the experimentally observed radius. The results are shown in Figure 22. The profile shapes are in better agreement with the experimentally observed profiles, indicating that the turbulent flow may indeed cause a significant increase in the effective thermal conductivity due to mass convection.

Additional insights can be gained if the chordal average temperatures are plotted as functions of applied magnetic field strengths as shown in Figure 23. The chordal average of the numerical temperature profiles remains in good agreement with the experimental chordal average throughout most of the range of magnetic field intensities. The uncertainty in the numerical solution due to the uncertainty in the electrical conductivity is reflected by the cross hatching.

The analytical approximation of Roninskii et al.[6] predicts temperatures several thousand degrees higher than does the numerical analysis. This is due to the radiation term which is neglected. At lower tempera-
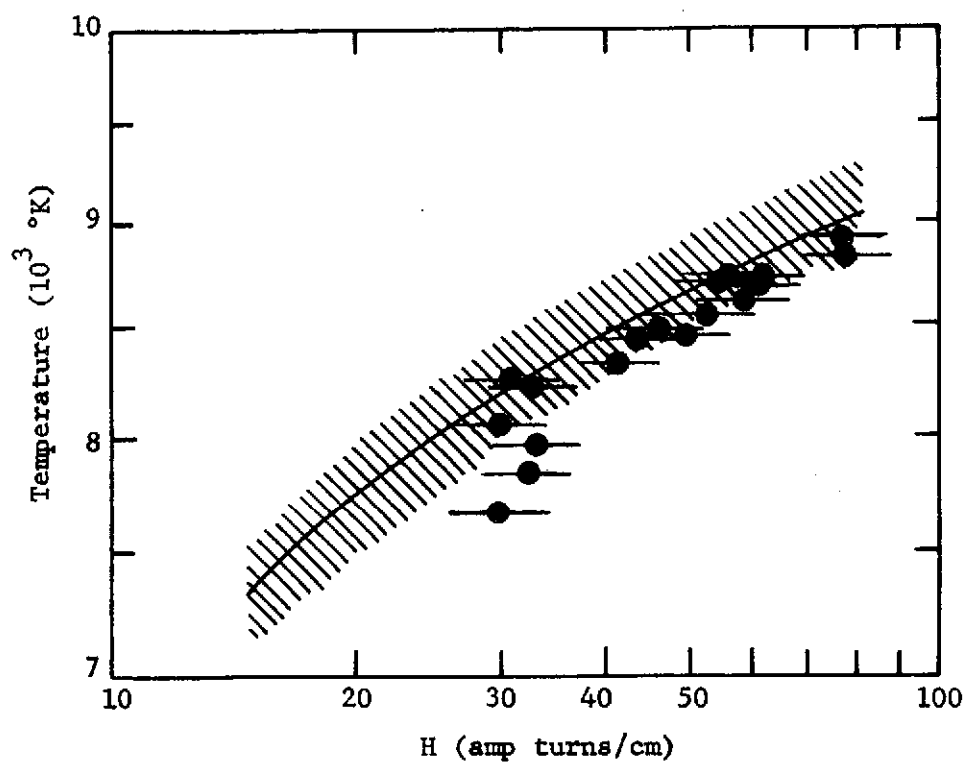
Figure 23. Comparison of Experimental and Theoretical Chordal
Average Temperatures vs. Magnetic Field Intensity

tures, radiation plays a less important role, and the two techniques converge. If the radiation term is set equal to zero in the numerical technique, the two solutions are nearly identical. In this case the maximum temperature occurs in the center for both techniques.

Figure 24 is a plot of the total linear power input and the power radiated as a function of magnetic field intensity predicted by the numerical analysis. The radiated power represents 50% of the total power input for a magnetic field strength of 75 amp-turns/cm and drops to 35% for a field strength of 30 am-turns/cm.

The numerical analysis predicts that a plasma can be sustained at magnetic field strengths as low as 15 amp-turns/cm, but experimentally the limit was determined to be about 30 amp-turns/cm. This can be seen in Figure 23, where the experimental points tend to diverge from theory at about 30 amp-turns/cm. This can also be attributed to flow. The plasma is literally "blown out" at low power levels by the flow.

Argon Seeded with Tungsten

The argon plasma was seeded with tungsten at number density ratios of 4.3×10^{-3}, 6.1×10^{-3}, and 3.6×10^{-2}. The greatest effect on the temperature profiles was with an N_w/N_{Ar} of 6.1×10^{-3}. This is most likely because the collision cross section of tungsten can no longer be neglected at the higher number densities of tungsten. Temperature profiles for three different magnetic field strengths and a tungsten number density ratio of 6.1×10^{-3} are shown in Figure 25. The temperatures are reduced approximately 1000°K below the pure argon case. Figure 26 is a plot of these same three profiles compared with the results of the numerical
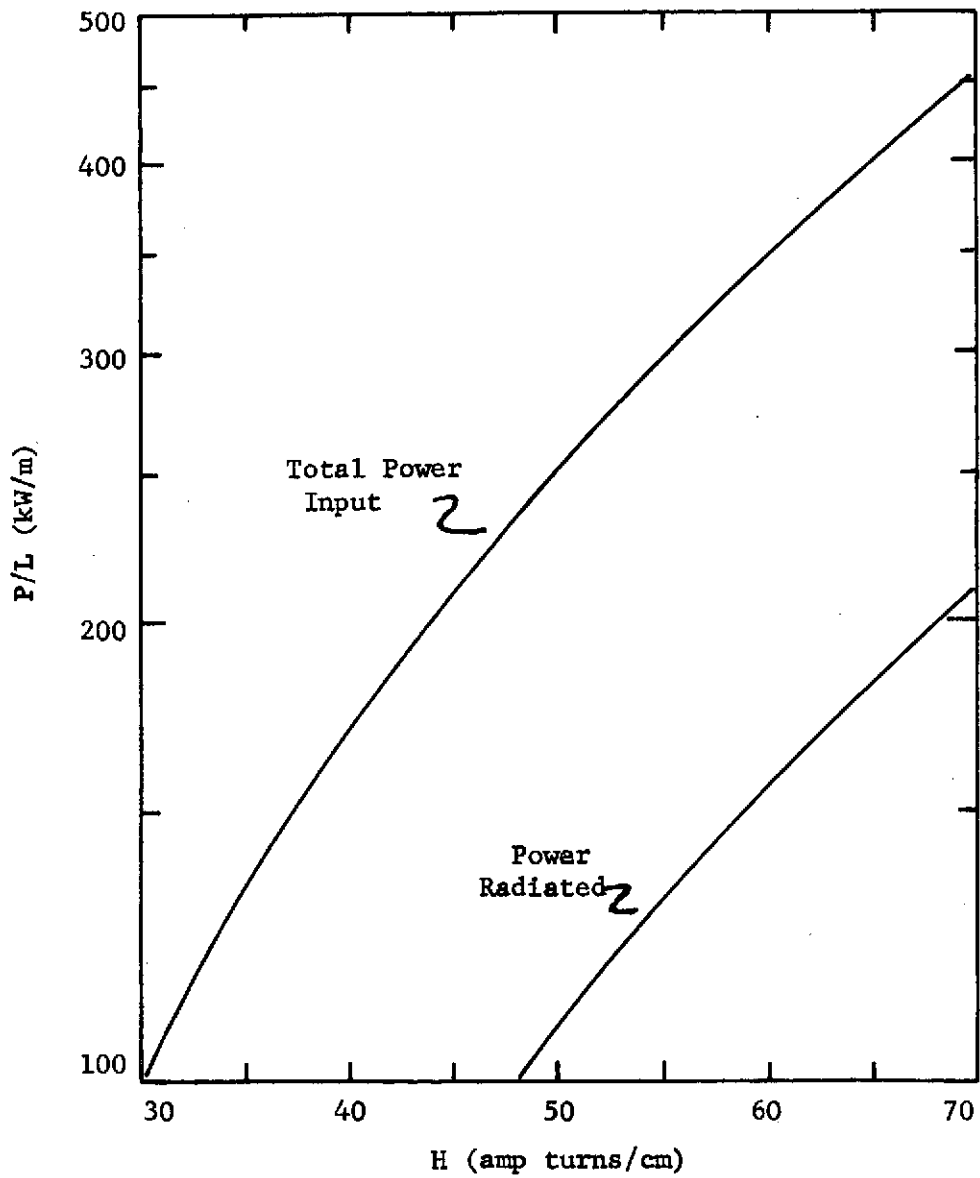
Figure 24. Numerical Analysis Predictions of Total Linear Power
Input and Power Radiated
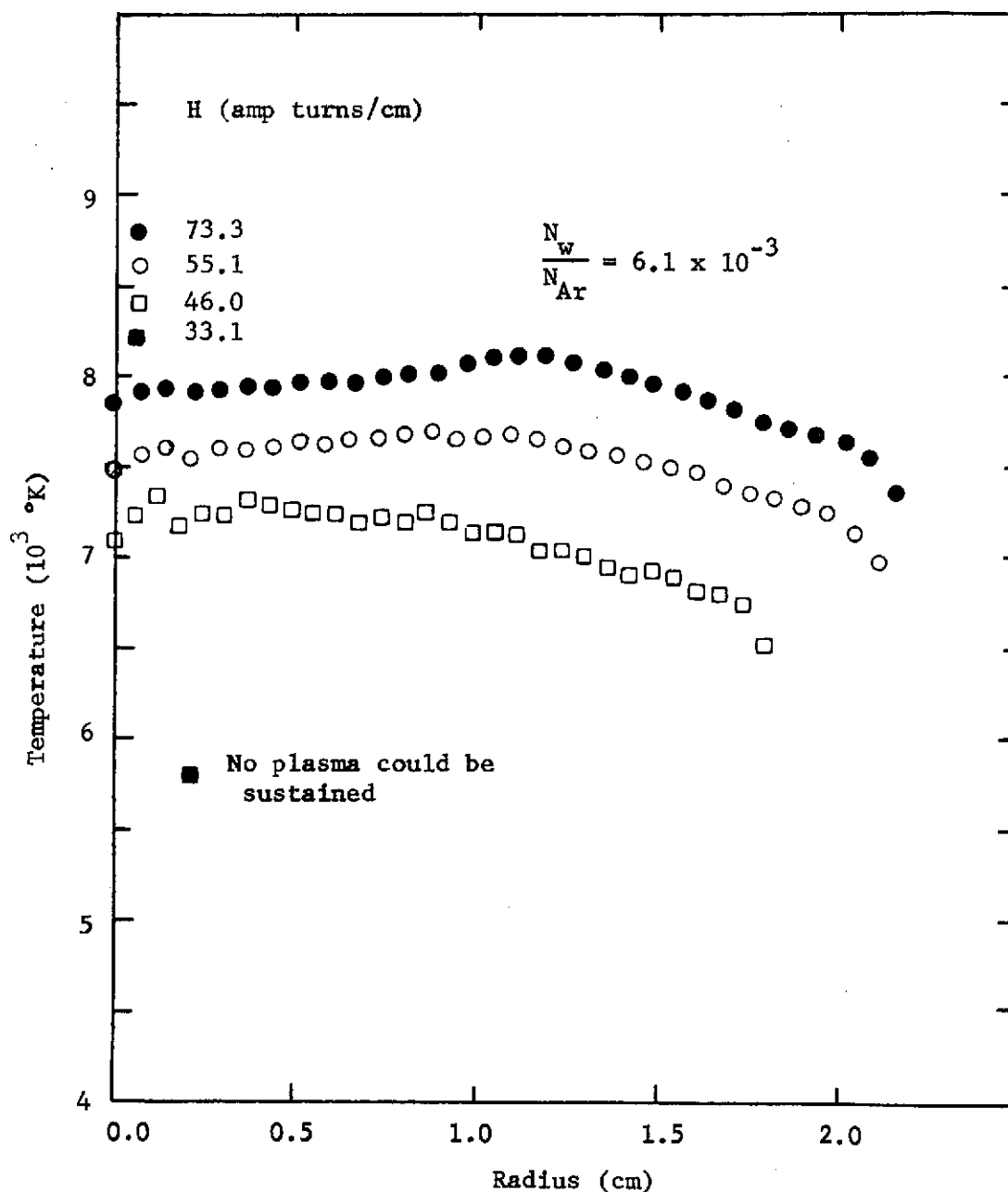
Figure 25. Experimental Temperature Profiles for a Tungsten Seeded
Argon Plasma at Four Representative Magnetic Field
Intensities

H = 33.1 amp turns/cm

No plasma could be sustained experimentally or numerically.

——— Experimental
— — — Numerical

$$\frac{N_w}{N_{Ar}} = 6.1 \times 10^{-3}$$

Figure 26. Comparison of Experimental and Theoretical Temperature Profiles for a Tungsten Seeded Argon Plasma at Four Representative Magnetic Field Intensities

analysis. The transport properties were altered in the numerical analysis as discussed in Chapter II. Figure 27 is a plot of the chordal average temperatures of the plasma as a function of magnetic field strength for the various tungsten partial pressures. The temperatures decrease with the addition of seed as predicted by the theoretical analysis with generally good agreement until the seed reaches an N_w/N_{Ar} of 3.6×10^{-2}. The experimental temperatures begin to rise for higher seed concentrations while the temperature calculated from the theory continues to decrease. This is because the theory neglects electron collisions with tungsten in the calculation of electrical conductivity.

Parametric Study of Numerical Analysis

The uncertainties in the transport properties of both seeded and unseeded argon and the experimental parameters that can be varied make it worthwhile to examine the effect the dat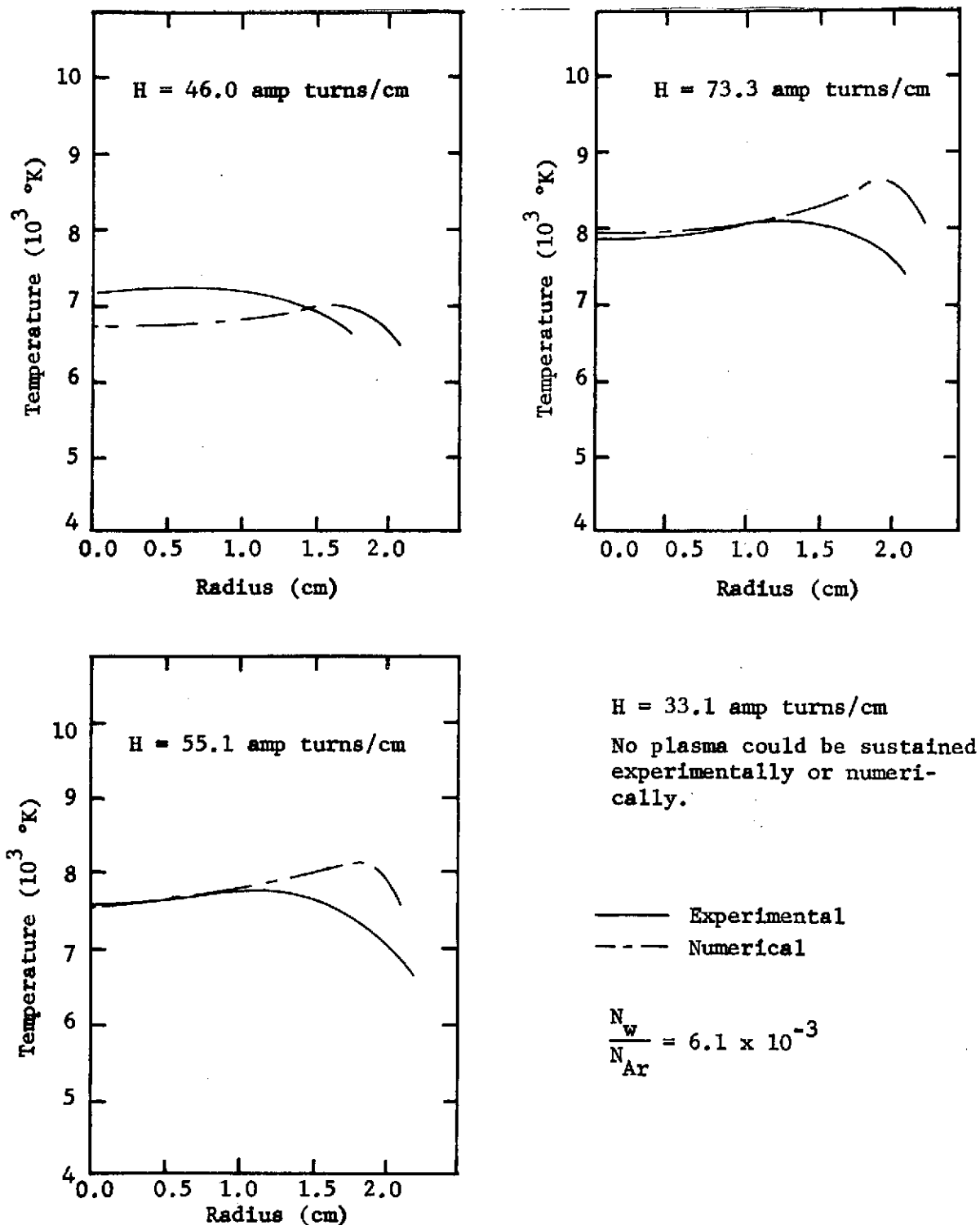a input to the numerical analysis has on the predicted temperature profiles. Figures 28, 29, 30, 31, and 32 each shows the temperature profiles at four different magnetic field intensities with the electrical conductivity, thermal conductivity, frequency, radius, and radial mass flow rate varied over the indicated ranges.

The effect of the electrical conductivity can be seen in Figure 28. The values were varied by translating the empirical curve with respect to temperature by 1000°K to either side of the values normally used in the analysis. This effectively bounds the available data. The electrical conductivity terms enter the governing equations through both the energy balance equation and the equation for the induced electric field. The induced electric field is lowered for higher values of electrical conduc-
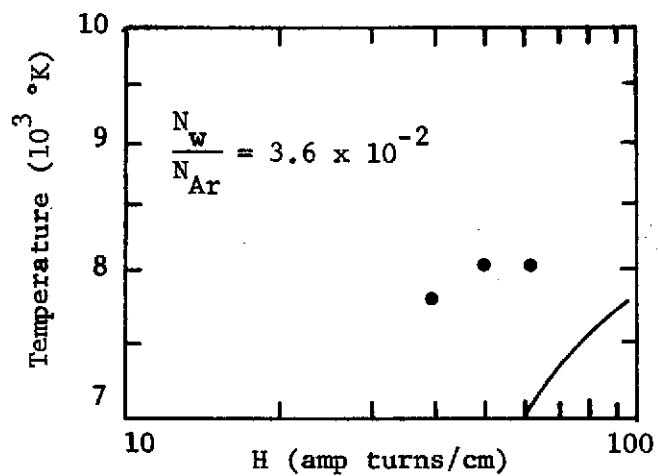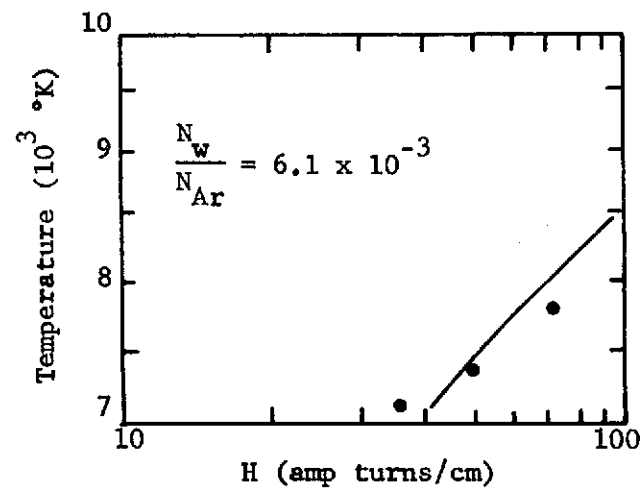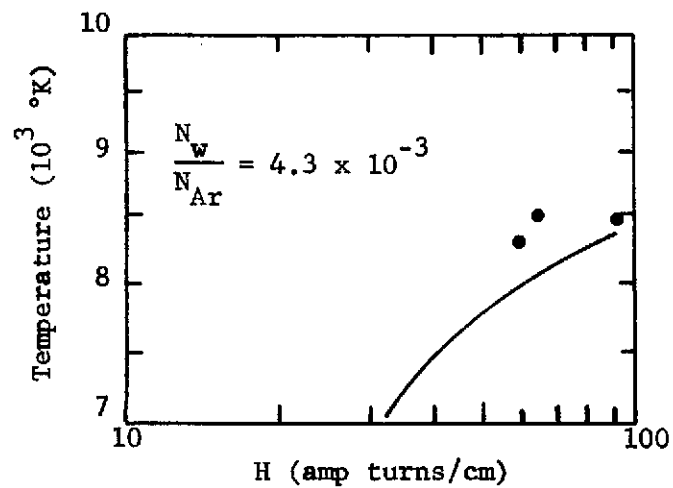
Figure 27. Comparison of Experimental and Theoretical Chordal Average Temperatures vs. Magnetic Field Intensity for Three Different Tungsten Partial Pressures
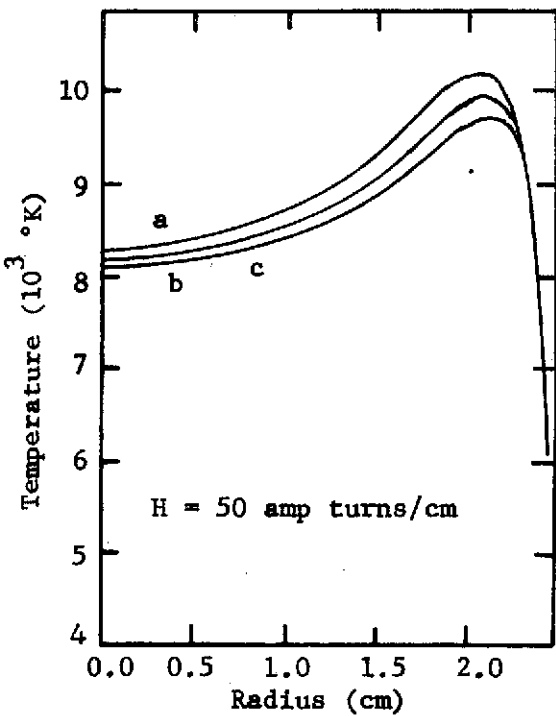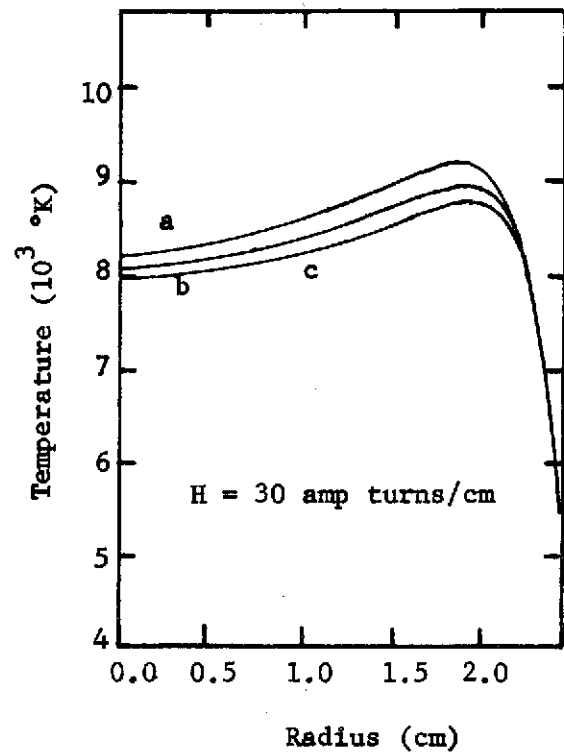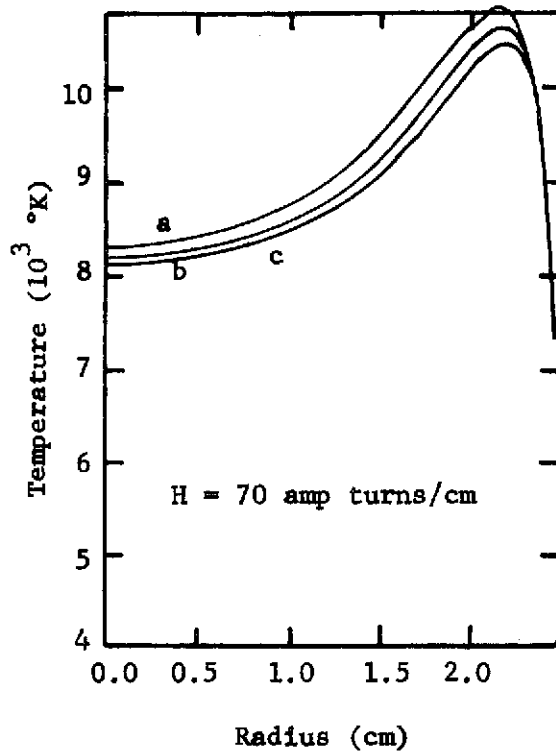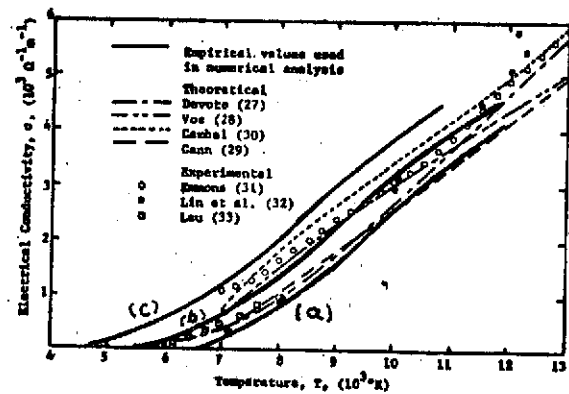
Figure 28. Parametric Study of Numerical Analysis--Electrical
Conductivity
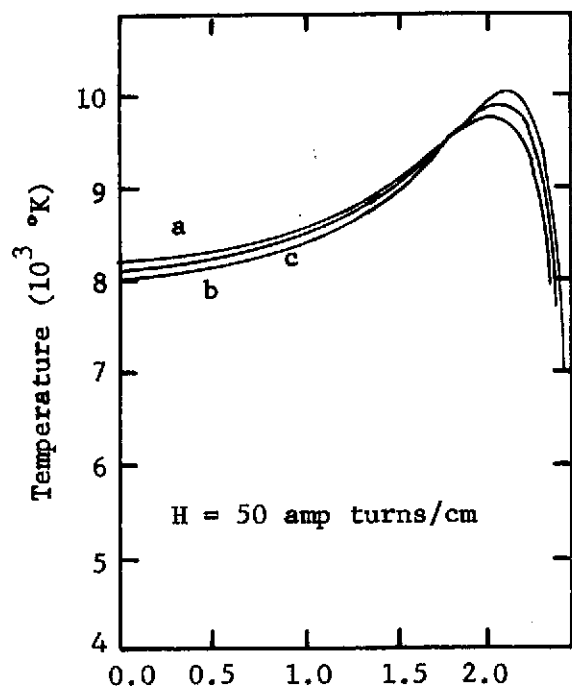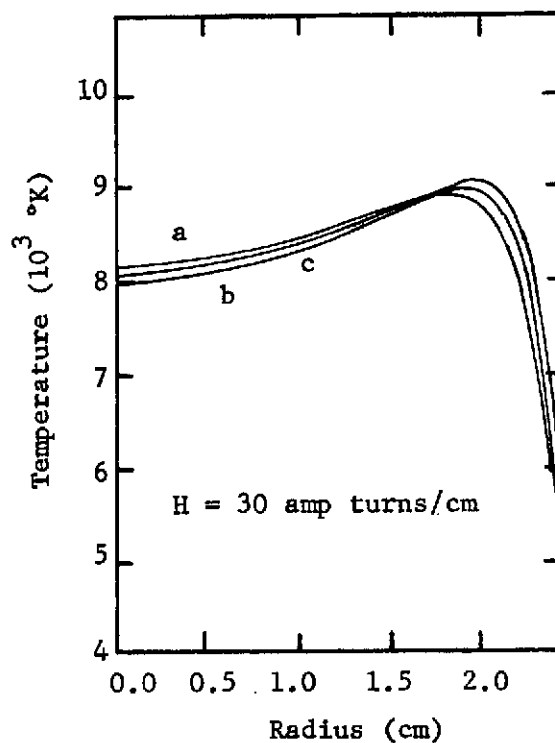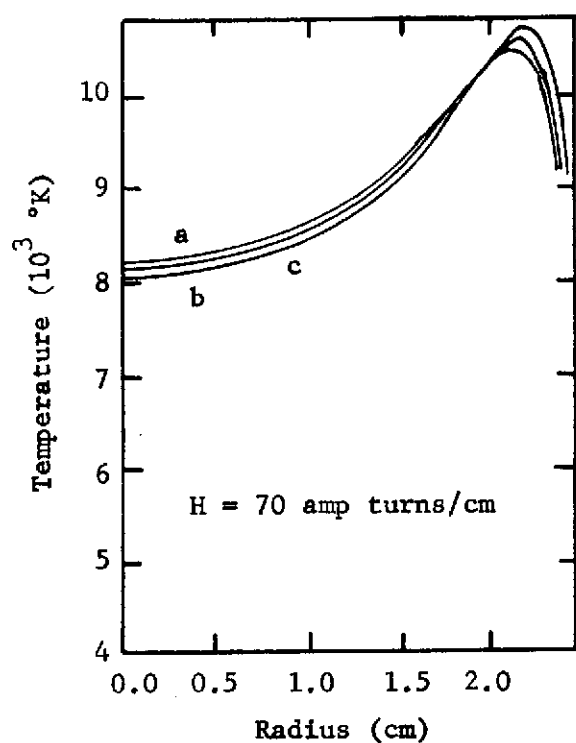
Figure 29. Parametric Study of Numerical Analysis--Thermal Conductivity
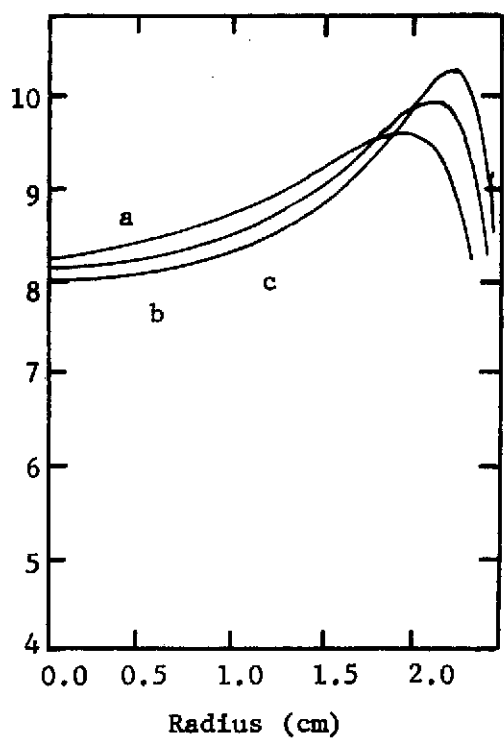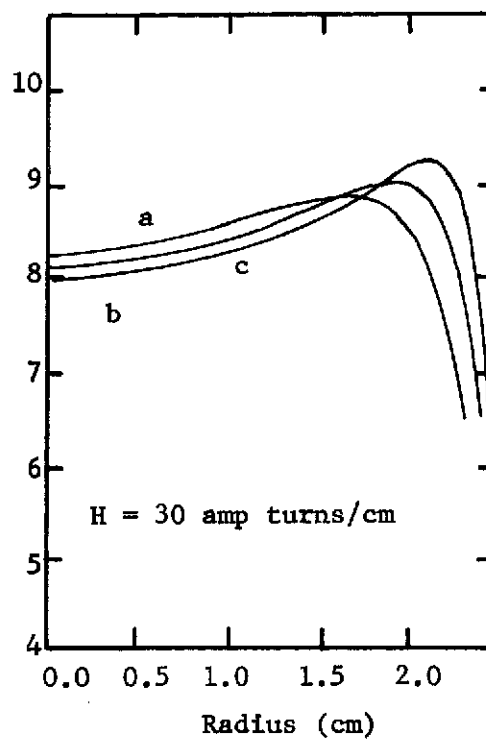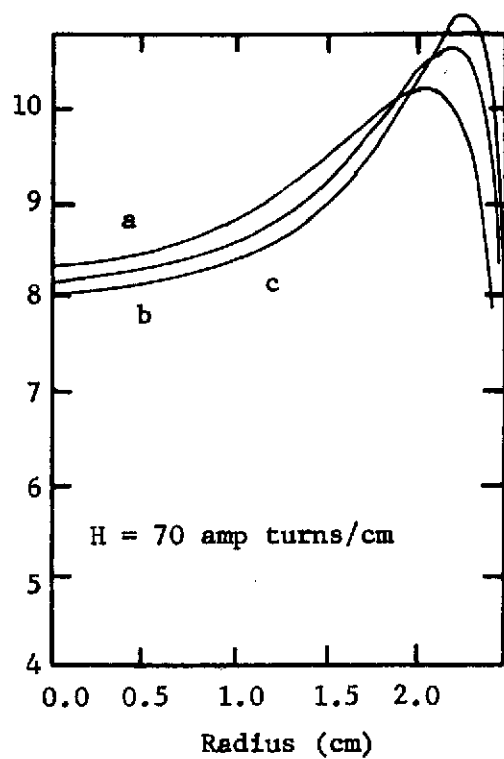
Figure 30. Parametric Study of Numerical Analysis--Frequency
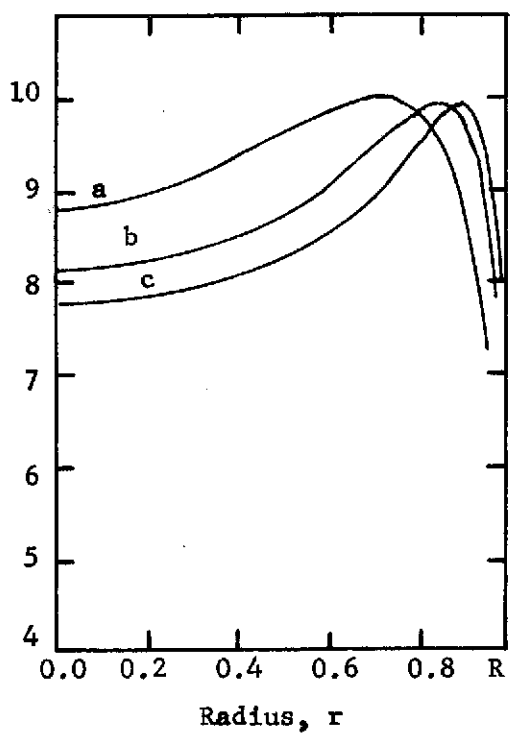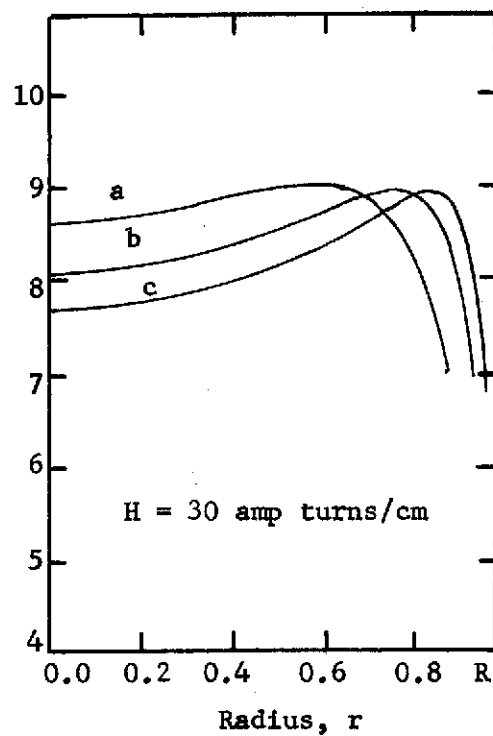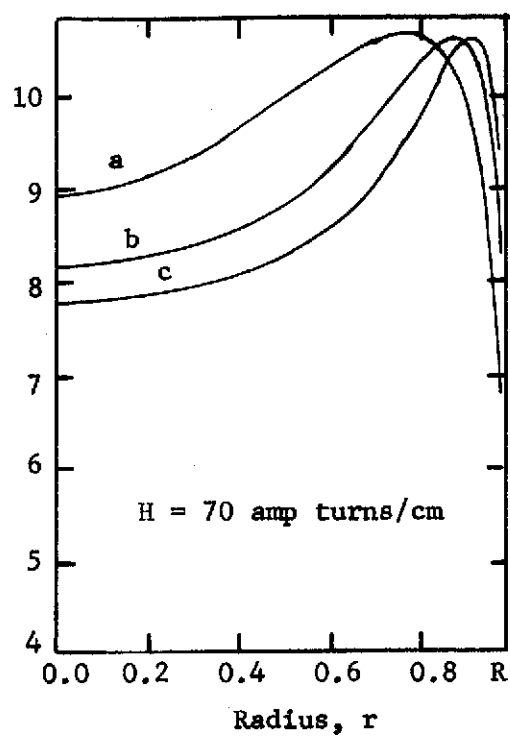
Figure 31. Parametric Study of Numerical Analysis--Radius

Temperature (10^3 °K)

10

9

8

7

6

5

4

0.0   0.5   1.0   1.5   2.0

Radius (cm)

a

b

c

H = 70 amp turns/cm

Temperature (10^3 °K)

10

9

8

7

6

5

4

0.0   0.5   1.0   1.5   2.0

Radius (cm)

a

b

c

H = 30 amp turns/cm

Temperature (10^3 °K)

10

9

8

7

6

5

4

0.0   0.5   1.0   1.5   2.0

a

b

c

H = 50 amp turns/cm
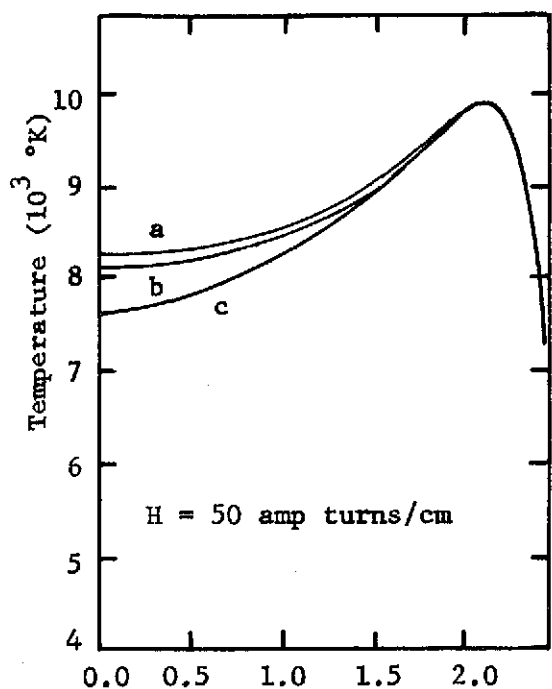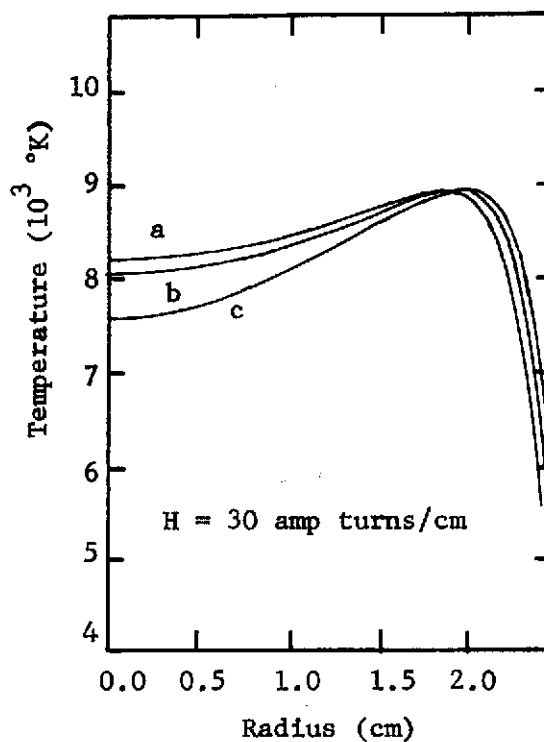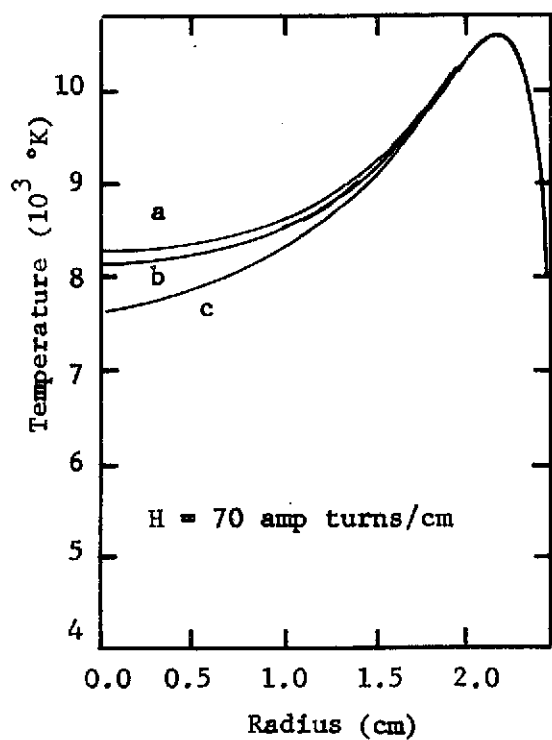
MASS FLOW RATE

$$(\rho \; u_r \; R) \; \frac{kg}{m \; sec}$$

+

(a)   +1.0 x 10^{-3}

(b)   0
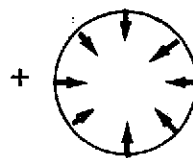
(c)   -1.0 x 10^{-3}

Figure 32.   Parametric Study of Numerical Analysis--Radial
Mass Flow Rate

tivity. This reduces the power input term for the energy balance equation, $\sigma E_\theta{}^2$, since the increase in σ is more than offset by the decrease in E_θ. The reduction in the power input term causes a uniform reduction in temperature, though the temperature values do not seem to be very sensitive to variations in the electrical conductivity values.

The temperature profiles are not very sensitive to the values chosen for the thermal conductivity either. Figure 29 shows the results of varying the values of λ by 25%. An increase in thermal conductivity causes the temperature profile to flatten as might be expected, but does not lower the average temperature in spite of the fact that more energy is transferred through the torch wall. This is most likely because the reduction in the maximum hot spot temperature lowers the total radiated energy more than the temperature increase in the central region increases it.

The frequency of the applied electromagnetic field effects its penetrating ability. At higher frequencies, the power input is over a narrower band near the tube wall, resulting in a lower center region temperature but a higher temperature near the wall. This effect can be seen in Figure 30.

The results of variations in the plasma radius are not so easy to predict. An increase in radius requires a larger net power input to keep the same values of the applied magnetic field intensity at the plasma radius. The surface area for heat transfer to the wall also increases. The hot spot temperature remains approximately the same as seen in Figure 31, though the central temperatures drop with increasing radius since the

induced electric field decreases as the penetration distance increases.

A study of the effect of a radial mass flow was made since there is some experimental evidence[22] that indicates such a flow may exist. The results are shown in Figure 32. The hot spot temperature is not affected in magnitude or position. The center region temperatures are increased with an inward flow toward a sink in the center.

The most surprising result of these studies is the very low sensitivity of the temperature profiles to any of the inputs, including the magnetic field intensity.

CHAPTER VII

CONCLUSIONS AND RECOMMENDATIONS

Conclusions

The one-dimensional system of equations made up of the energy

balance equation, Maxwell's equations, and Ohm's law are adequate to

quantitatively describe the chordal average temperature inside an rf

plasma over a wide range of magnetic flux intensities but do not describe

the profile shape as well as might be desired. This is a possible result

of the complex turbulent flow patterns inside the torch which are not ac-

counted for in the analysis. There does not appear to be any reasonable

solution at present to this problem, though experimental and theoretical

temperature profiles would most certainly be in better agreement for ex-

perimental plasmas designed to minimize this effect. An effort was made

to simulate the effects of turbulence by increasing the thermal conduc-

tivity values and using the experimentally observed radius in place of

the torch radius in the numerical analysis. Agreement with experimentally

observed temperature profiles was improved.

The neglect of the radiation term in the energy balance equation

is not justified. The results of the numerical treatment and experiment

show that the temperatures encountered at the magnetic flux intensities

necessary to sustain a plasma are too high to neglect the effect of radia-

tion. The closed-form analytical approximations that neglect radiation

do yield interesting insights into the problem, most notably with regard

to the degree of coupling between the electrical and thermal conductivities and the resulting temperature predictions, but do not accurately predict the maximum temperatures encountered or the temperature profiles.

The numerical solutions are not highly sensitive to any of the experimentally controllable inputs or to the electrical or thermal conductivity values chosen. This lack of sensitivity was experimentally observed with respect to the magnetic flux intensity and conductivity values but equipment limitations prevented variations of the torch radius or rf driving frequency. The addition of tungsten seed significantly increased the electrical and thermal conductivities of the argon but lowered the temperatures of the plasma, as predicted by theory, by only about 1000°K for corresponding magnetic field intensities.

Recommendations

An experimental arrangement that minimizes the effect of turbulent flow would form a better basis for comparison with theory. Extending the experimental measurements to two dimensions would be a valuable addition to those numerical techniques which attempt to take into account the axial variation of the energy addition region. Utilizing gases with marked differences in transport properties would help establish the ability of the theory to handle the problem. A more productive effort might be made in the direction of simplifying the calculations necessary to determine the chordal average temperatures resulting from the many variables open to the experimenter. A modification of the existing closed form solutions that takes into account radiation would be a valuable ad-

dition. A detailed comparison with existing numerical solutions over a wide range of cases would lend credence to the results of this modified closed form solution.

APPENDIX A

COIL AND MAGNETIC FLUX GEOMETRY

The magnetic field intensity inside the work coil is a function of the work coil geometry and is proportional to the current in the work coil. Figure 33 is a full scale drawing of a cross section of the work coil and torch with the plane of observation noted.

The magnetic field intensity at any point z along the axis can be calculated from the work coil current, I, by

$$H = \sum_i \frac{a^2 I}{2(a^2 + x_i)^{\frac{3}{2}}} \tag{87}$$

where a is the work coil radius and x_i is the axial distance from point z to each coil position, as noted in Figure 33.

Defining

$$\gamma(z) = \sum_i \frac{a^2}{2(a^2 + x_i)} \tag{88}$$

Then

$$H(z) = I \; \gamma(z) \tag{89}$$

The calculated values of $\gamma(z)$ are shown in Figure 33. These values were experimentally verified by passing a known d.c. current through the coil and measuring the magnetic field intensity inside the coil with a
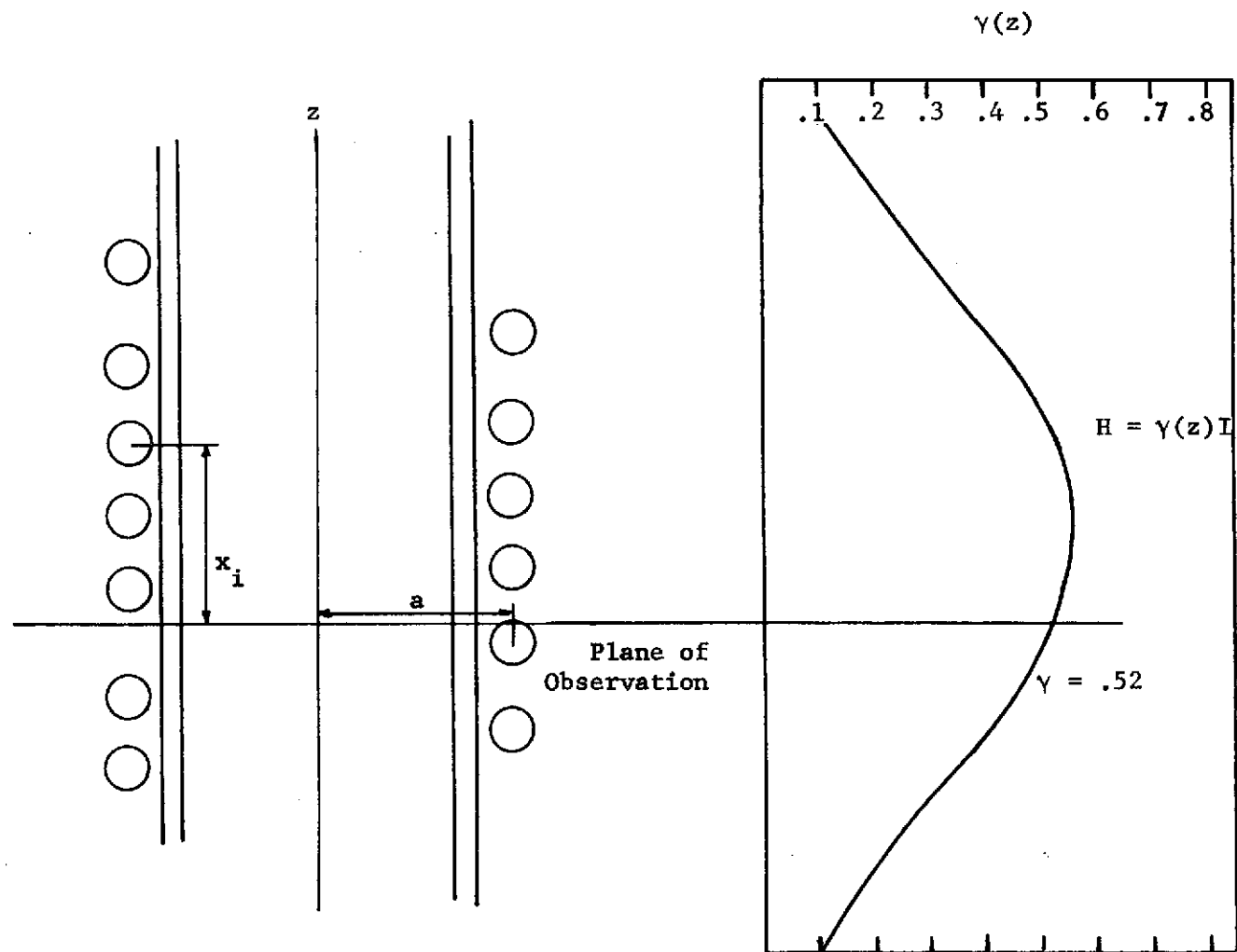
Figure 33.   Work Coil Geometry and Magnetic Field Intensity Distribution

Bell Model 640 Gaussmeter. Figure 34 is a plot of experimentally meas-

ured points taken at the observation plane used for the plasma tempera-

ture profiles and a line corresponding to the theoretically calculated

value of $Y = .52$ at that point. The agreement appears excellent.
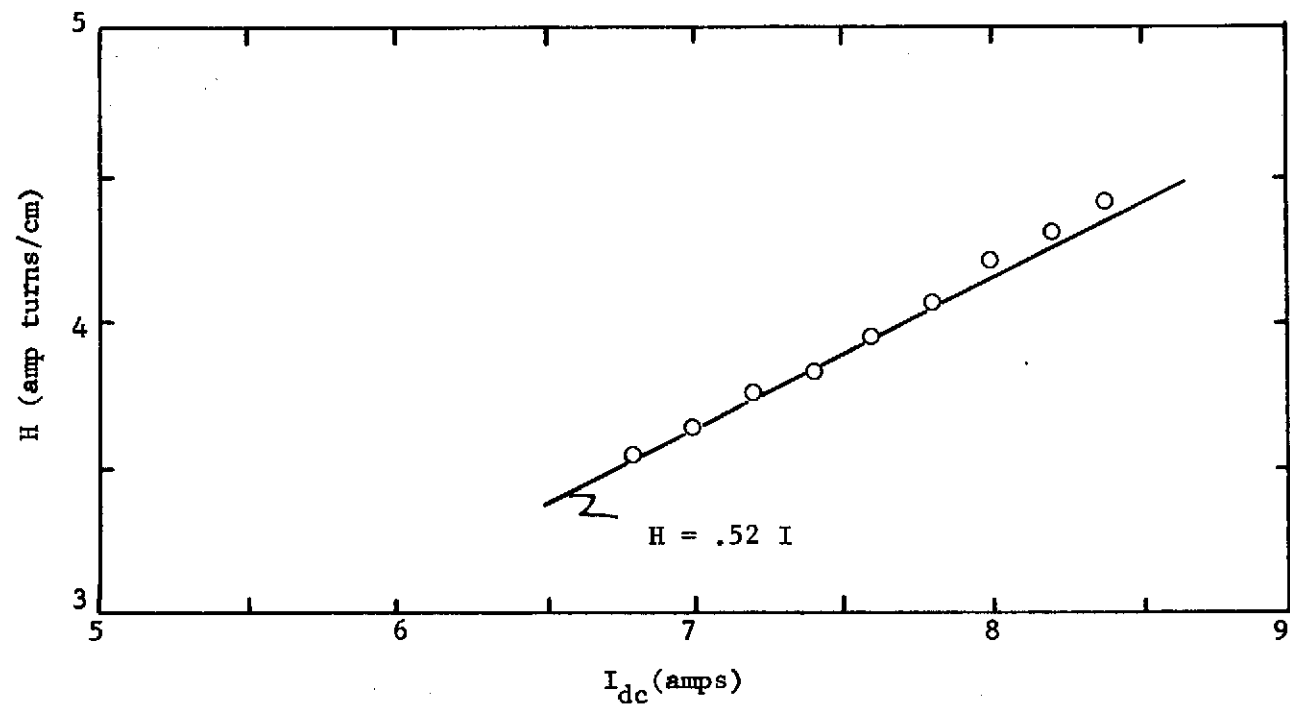
Figure 34. Experimental Measurements of Magnetic Field Intensity in Work Coil

APPENDIX B

PLASMA START-UP CHECK LIST

Pre-Start

Pad Input Switch	off.
Arc Welder	off
Main Water	off
Capacitor Drain Switch	down
New Filter Papers	check
Spectrometer	6328 Å
Torch Alignment	check
Argon Supply	check
Bypass Flow	clean
Torch Leaks	check
Visicorder Spatial Alignment	record
Spectrometer	4315 Å
Spatial Scan	centered
Ground Switch	on

Start

Capacitor Drain Switch	up
Pad Input Switch	on
Arc Welding Rod	clear
Coil Cooling Water	on
Interlock System	all off (left)

Pad Input Starter	on
Rectifier Switches	on (right to left)
Plate Voltage Delay	on
Screen Voltage Control	full c.c.w.
Grid Voltage Control	full c.c.w.
Grid and Screen Power Supply Circuit Breakers	on
RF Driver	full c.c.w.
Filament Voltage	full c.c.w.
Tube Blower Circuit Breaker	on
Aux. Blowers and d.c. Arc Circuit Breakers	on
Filament Circuit Breaker	on
1 kW Amp. Circuit Breaker	on
RF Driver--four switches	on 1 4 2 3
Grid Voltage	200 V
Screen Voltage	200 V
Filament Voltage	2 V
Plate Voltage	lower until zero light on
Plate High Voltage	on
Plate Voltage	2500 V
Grid Voltage	300 V
Screen Voltage	300 V
Filament Voltage	3.5 V
Grid Voltage	400 V
Screen Voltage	400 V
Filament Voltage	5 V

5 min

5 min

5 min	Grid Voltage	500 V
	Screen Voltage	700 V
	Filament Voltage	7 V
	Cascade Interlock Lights	check on
	Ready Light	check on
5 min	Filament Voltage	9.7 V
	Switching Network	
	Turnoff	on (right)
	Grid	on (right)
	Plate	on (right)
	Screen	on (right)
	RF Driver	c.w. until screen current noted, then full c.c.w.
	Plate Voltage	5000 V
	RF Driver	c.w. until screen current noted, then full c.c.w.
	Plate Voltage	7500 V
	RF Driver	c.w. until screen current noted, then full c.c.w.
	Argon Pressure	40 psi
	Argon Bypass Flow Rate	3"
	Torch Blowers	on
	Arc Welder	on
	RF Driver	c.w. until screen current 150 ma

Ignition

Draw Arc with Welding Rod to
Water Cooled Center Electrode

Immediately after Ignition

    Arc Welder   off

    RF Driver   c.w. until screen current 100 ma

    Ground Switch   off

    Duct in Place

Warm up Torch Slowly

Normal Shut Down

Simultaneously

    Switching Network Turnoff   off (left)

    RF Driver   full c.c.w.

Immediately

    Switching Network Screen   off (left)

                       Plate   off (left)

                       Grid   off (left)

                       Filament   off (left)

Plate Voltage   2000 V

Filament   0 V

Screen Voltage   0 V

Grid Voltage   0 V

Plate High Voltage   off

Delay   off

Rectifier Switches   off (left to right)

Pad Input Starter   stop

Argon Flow   off

Grid and Screen Supply Circuit Breakers   off

Filament Circuit Breaker	off
RF Driver--four switches	off 4 1 3 2
1 kW Amplifier Circuit Breaker	off
Torch Blowers	off
Water	1/2 flow
15 Min	
Aux. Blowers and d.c. Arc Circuit Blowers	off
Tube Blower Circuit Breaker	off
Water	off
Pad Input Switch	off
Main Water	off
Capacitor Drain	off

Unintentional Plasma Shut Down

Simultaneously

Switching Network Turnoff	off (left)
RF Driver	full c.c.w.

Immediately

Switching Network Screen	off (left)
Plate	off (left)
Grid	off (left)
Filament	off (left)

Re-Start

Plate Voltage	3000 V
Overcurrent Trips	reset
Filament	9.7 V

Ground Switch		on
Switching Network:		
	Turnoff	on (right)
	Grid	on (right)
	Plate	on (right)
	Screen	on (right)
RF Driver		c.w. until screen current noted, then full c.c.w.
Plate Voltage		5000 V
RF Driver		c.w. until screen current noted, then full c.c.w.
Plate Voltage		7500 V
RF Driver		c.w. until screen current noted, then full c.c.w.
Arc Welder		on
RF Driver		c.w. until screen current 150 ma

Follow Normal Ignition Procedure
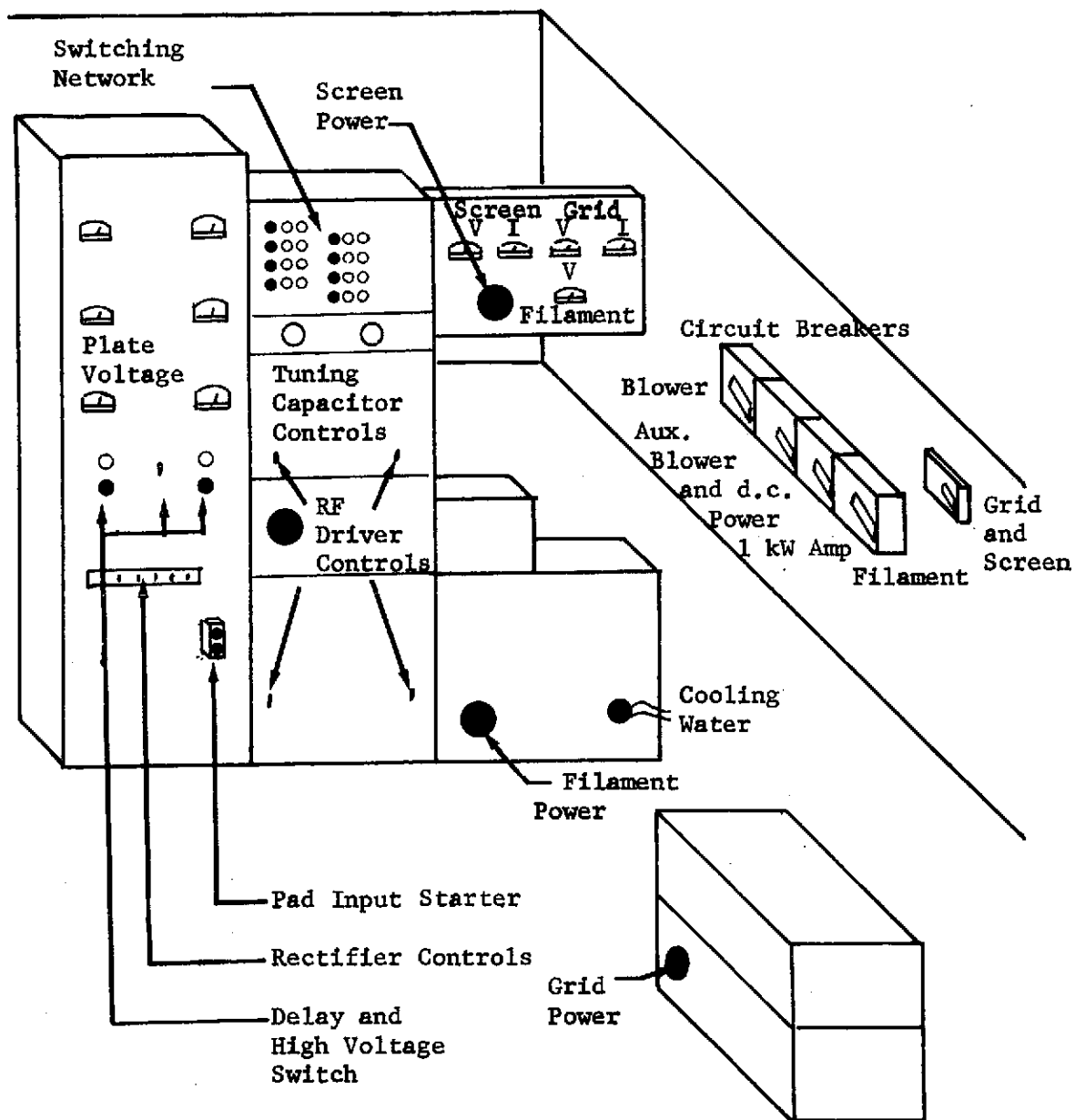
Figure 35. Plasma Generating Facility Lay-Out

APPENDIX C

MODIFIED ABEL INVERSION COMPUTER PROGRAM

```
      INTEGER CODE,Y,Y1
      INTEGER COUNT
      REAL IC,KAPPA
      REAL KOLD
      REAL NE
      DIMENSION IC(50),X(50,51),EC(50),KAPPA(50),B(50)
      DIMENSION T(50)
      DIMENSION OIC(26),RE(1),AC(26),BC(26),CC(26),DC(26),CCC(26)
      DIMENSION A(50,51),BX(50,51),C(50,51),D(50,51)
      DIMENSION TOLD(50),KOLD(50),ECO(50)
      DIMENSION XU(1),YU(1),YNR(26),OICN(26)
C  READ IN DATA
C  FIRST CARD CONTAINS RUN CODE,PLASMA RADIUS(CM),NUMBER OF ZONES
C  USED IN ANALYSIS (BETWEEN 4 AND 50), WAVELENGTH (ANGSTROMS), NUMBER OF
C  DATA POINTS FED IN (BETWEEN 4 AND 25)
C  FORMATED (I3,F10.2,I10,F10.1,I10)
C  IF THIS CARD IS BLANK PROGRAM ASSUMES END OF DATA SETS
   99 READ(5,800) CODE,R,N,WL,NDP
      N=40
      IF(CODE.EQ.0) GO TO 920
      WRITE(6,801)CODE,R,N,WL,NDP
      WRITE(1,800)CODE,R,N,WL,NDP
C  NEXT READ IN OBSERVED INTENSITY(WATTS/CM**3-SR) FOR EACH ZONE.THE
C  OUTSIDE ZONE IS Y=1 .ONE DATA POINT ON EACH CARD WITH THE ZONE NUMBER
C  AND THE INTENSITY AS(I3,1PE18.3)
C  THE PROGRAM ASSUMES THE INTENSITY IS
C  ZERO AT THE RADIUS OF THE PLASMA
      DO 50 Y=1,N
      TOLD(Y)=0.0
      KOLD(Y)=0.0
   50 CONTINUE
      KNOT=0
      COUNT=0
      WRITE(6,802)
      DO 100 K=1,NDP
```

```
      READ(5,803) Y,OIC(Y)
      WRITE(6,804)Y,OIC(Y)
      WRITE(1,816) Y,OIC(Y)
  100 CONTINUE
      DO 101 I=1,NDP
      C1=I-1
      C2=NDP
      YNR(I)=R*(C1/C2)
      OICN(I)=OIC(NDP-I+1)
  101 CONTINUE
      YNR(NDP+1)=R
      YNR(NDP+2)=R*(1+(1/C2))
      OICN(NDP+1)=0.0
      OICN(NDP+2)=0.0
      CALL COEFF(YNR,OICN,NDP+2,1,0,2,0,RE,PQ,AC,BC,CC,DC,CCC,XU,YU)
      WRITE(6,813)
      DO 102 Y=1,N
      C1=N
      C2=Y
      C3=R*((C1-C2)/(C1))
      CALL INTRP4(C3,C4,1)
      IC(Y)=C4
      WRITE(6,814) Y,C3,IC(Y)
      WRITE(1,814) Y,C3,IC(Y)
  102 CONTINUE
C CALCULATE GEOMETRIC MATRIX ARRAY
      X(N,N+1)=0.0
      DO 105 K=N,1,-1
      DO 105 I=K,1,-1
      X(K,K+1)=0.0
      Z2=0.0
      IF(I.EQ.K) GO TO 104
      I1=I+1
      DO 103 J=I1,K
      Z2=Z2+X(K,J)
```

```
    103 CONTINUE
    104 YY=I-1
        ZZ=K
        ZYZ=N
        X(K,1)=(R)*((1-YY/ZYZ)**2-(1-ZZ/ZYZ)**2)**0.5-Z2
    105 CONTINUE
C CALCULATE EMISSION COEFFICIENTS -ASSUME PLASMA OPTICALLY THIN
        EC(1)=(IC(1))/(2*X(1,1))
        IF(EC(1).LT.0.0) EC(1)=0.1
        DO 250 K=2,N
        SUM=0.0
        J1=K-1
        DO 210 J=1,J1
        SUM=SUM+X(K,J)*EC(J)*2.0
    210 CONTINUE
        EC(K)=(IC(K)-SUM)/(2*X(K,K))
        IF(EC(K).LT.0.0) EC(K)=0.0
    250 CONTINUE
C CALCULATE TEMPERATURE
    300 CONTINUE
        DO 350 K=N,1,-1
        GTH=10999.0
        GTL=4001.0
    310 GT=(GTH+GTL)/(2.0)
        NE=ARND(GT)
        GEC=ECEQ(GT,NE,WL)
        IF(GEC.GT.EC(K)) GTH=GT
        IF(GEC.LE.EC(K)) GTL=GT
        IF((GTH-GTL).GT.05.0)GO TO 310
        T(K)=(GTH+GTL)/(2.0)
    350 CONTINUE
C CALCULATE OPACITY
    400 CONTINUE
        DO 425 K=N,1,-1
        B(K)=BLKBDY(WL,T(K))
```

```
      KAPPA(K)=EC(K)/B(K)
  425 CONTINUE
  500 CONTINUE
      JJ=0
      J =0
      COUNT=COUNT+1
      DO 525 Y=1,N
      PCENT=(T(Y)-TOLD(Y))/(T(Y))
      PCENO=(KAPPA(Y)-KOLD(Y))/(KAPPA(Y))
      PCENE=(EC(Y)-ECO(Y))/(EC(Y))
      IF(PCENT.GE.0.005)J=1
      IF(PCENO.GE.0.005)JJ=1
      IF(PCENE.GE.0.005)J=1
      TOLD(Y)=T(Y)
      KOLD(Y)=KAPPA(Y)
      ECO(Y)=EC(Y)
  525 CONTINUE
      IF(J.EQ.0) GO TO 900
      IF(JJ.EQ.0) GO TO 900
      IF(COUNT.EQ.20) GO TO 900
C   CALCULATE OPTICAL ARRAYS
  600 CONTINUE
      KONT=KONT+1
      DO 620 Y=1,N
      DO 620 I=1,Y
      A(Y,I)=(1-EXP(-KAPPA(I)*X(Y,I)))/(KAPPA(I))
      BX(Y,I)=-KAPPA(I)*X(Y,I)
      C(Y,I)=0.0
      D(Y,I)=0.0
  620 CONTINUE
      C(1,1)=0.0
      D(1,1)=BX(1,1)
      DO 650 Y=2,N
      DO 650 I=1,Y
      IF(I.EQ.1) GO TO 630
      SUM=0.0
```

```
      I1=I-1
      DO 625 L=1,I1
      SUM=SUM+BX(Y,L)
  625 CONTINUE
      C(Y,I)=SUM
  630 CONTINUE
      SUM=0.0
      DO 635 L=1,Y
      SUM=SUM+BX(Y,L)
  635 CONTINUE
      IF(I.EQ.Y) GO TO 641
      I1=I+1
      DO 640 L=I1,Y
      SUM=SUM+BX(Y,L)
  640 CONTINUE
  641 D(Y,I)=SUM
  650 CONTINUE
C  CALCULATE NEW EMMISSION COEFFICIENTS
  700 CONTINUE
      EC(1)=(IC(1))/(A(1,1)+A(1,1)*EXP(BX(1,1)))
      IF(EC(1).LT.0.0) EC(1)=0.0
      DO 747 Y=2,N
      SUM=0.0
      Y1=Y-1
      DO 737 L=1,Y1
      SUM=SUM+(EC(L)*A(Y,L))*(EXP(D(Y,L))+EXP(C(Y,L)))
  737 CONTINUE
      EC(Y)=(IC(Y)-SUM)/(A(Y,Y)*(EXP(D(Y,Y))+EXP(C(Y,Y))))
      IF(EC(Y).LT.0.0) EC(Y)=0.0
  747 CONTINUE
      GO TO 300
  800 FORMAT(I3,F10.2,I10,F10.1,I10)
  801 FORMAT(1H1,20X,'ANALYSIS PROGRAM FOR ARGON PLASMA',////,
     1             30X,'RUN CODE IS',I4,/,
     2             30X,'PLASMA RADIUS IS',F6.3,1X,'CM.',/,
```

```
     3              30X,'THERE ARE',I3,1X,'ZONES USED IN THE ANALYSIS',/,
     4              30X,'THE CONTINUUM IS OBSERVED AT',F7.1,1X,'ANGSTROMS',
     5         /,   30X,'THERE WERE',I4,1X,'DATA POINTS')
  802 FORMAT(1H1,20X,'OBSERVED INTENSITY',///,15X,'ZONE',10X,
     1                'INTENSITY (WATTS/SR-CM**4)',//)
  803 FORMAT(I3,1PE18.3)
  804 FORMAT(15X,I4,10X,1PE9.3)
  809 FORMAT(1H1,30X,'CALCULATED PLASMA PARAMETERS',///,
     1 10X,'ZONE',5X,'OBSERVED INTENSITY',5X,'EMISSION COEFFICIENT',
     2 5X,'TEMPERATURE',5X,'ABSORPTION COEFFICIENT',5X,'BLACK BODY RAD'
     3 /,19X,        '(WATTS/CM**3-SR)  ',5X,'(WATTS/CM**4-SR)      ',
     4 5X,'DEG.KELVIN ',5X,'           (CM-1)',14X,'(WATTS/CM**3-SR)',//)
  810 FORMAT(10X,I3,5X,1PE14.3,7X,1PE17.3,9X,0PF9.1,10X,
     1    1PE12.3,10X,1PE12.3,/)
  813 FORMAT(10X,'ZONE',10X,'R',20X,'IC',///)
  814 FORMAT(10X,I3,F14.3,F20.3)
  815 FORMAT(I4,3F20.5)
  816 FORMAT(I3,F10.1)
  817 FORMAT (I20)
  900 CONTINUE
C WRITE OUT DATA
      WRITE(6,809)
      DO 910 Y=N,1,-1
      WRITE(6,810) Y,IC(Y),EC(Y),T(Y),KAPPA(Y),B(Y)
      WRITE(1,815) Y,        EC(Y),T(Y),KAPPA(Y)
  910 CONTINUE
      WRITE(6,817) KONT
      GO TO 99
  920 CONTINUE
      END
```

```fortran
      FUNCTION GAUNT(WL)
C  THIS FUNCTION CALCULATES THE GAUNT
.C  FACTOR AS A FUNCTION OF WAVELENGTH
.C  (WL-ANGSTROMS) EMPERICALLY BASED ON
C  DATA BY DIETER SCHLUTER-Z.ASTROPHYSIK
C  VOL 61 PAGE 67-1965-RANGE 3500-6500 A
      IF((WL.LT.3500.).OR.(WL.GT.6500.)) GO TO 3
      IF(WL.LT.4800.) GO TO 2
      IF(WL.LT.4900.) GO TO 1
      GAUNT=(0.5/600.)*(WL-4900.)+1.5
      RETURN
    1 GAUNT=(0.4/100.)*(4900. -WL)+1.5
      RETURN
    2 GAUNT=(0.75/1300.)*(WL-3500.)+1.15
      RETURN
    3 WRITE(6,4) WL
    4 FORMAT(1H1,1X,'WAVELENGTH OUT OF RANGE IN GAUNT',F10.2)
      GAUNT=2.0
      RETURN
      END
```

```
      FUNCTION BLKBDY(A,T)
C  THIS FUNCTION CALCULATES THE BLACKBODY
C  RADIATION IN(WATTS/SR-CM**3) FOR A
C  GIVEN WAVELENGTH(A-ANGSTROMS) AND A
C  GIVEN TEMPERATURE(T-DEG K).
      C1=5.951E12
      C2=143.86
      W=A/1000.0
      U=T/1000.0
      BLKBDY=(1/(EXP(C2/U/W)-1))*((2*C1)/(W**5))
      RETURN
      END
```

```
      FUNCTION ARND(T)
C   THIS FUNCTIONAL ROUTINE CALCULATES THE
C   ELECTRON AND ION NUMBER DENSITY IN CM-3
C   (WHICH ARE ASSUMED EQUAL) FOR ARGON GAS
C   AT ONE ATMOSPHERE AND WITHIN THE TEMPERATURE
C   RANGE OF 4000-14000 DEG K.  THIS PROGRAM
C   INTERPOLATES BETWEEN VALUES THAT ARE 1000 DEG K
C   APART ASSUMING AN N=A*T**(5/4)*EXP(B/T) DEPENDENCE
C   THE DATA POINTS ARE TAKEN FROM OLSEN.S GASCOMP
C   PROGRAM REPORTED ON IN ARL 70-0048 MARCH 1970
      DIMENSION DT(15),DN(15)
      IF((T.LT.4000.0).OR.(T.GE.14000.0)) GO TO 201
      DO 100 I=1,15
      DT(I)=I*1000.0
      DN(I)=0.0
  100 CONTINUE
      DN(4) = 1.27E10
      DN(5) = 1.32E12
      DN(6) = 2.94E13
      DN(7) = 2.72E14
      DN(8) = 1.45E15
      DN(9) = 5.34E15
      DN(10)= 1.51E16
      DN(11)= 3.46E16
      DN(12)= 6.62E16
      DN(13)= 1.08E17
      DN(14)= 1.50E17
      DO 101 I=4,13
      IF((T.GE.DT(I)).AND.(T.LT.DT(I+1))) GO TO 195
  101 CONTINUE
      GO TO 201
  195 A=DN(I)
      X=(ALOG(DN(I+1)/DN(I)))-(5.0/4.0)*(ALOG(DT(I+1)/DT(I)))
      B=(DT(I)*DT(I+1)*X)/(DT(I)-DT(I+1))
      A=(DN(I))/((DT(I)**(5.0/4.0))*(EXP(B/DT(I))))
```

```
      ARND=A*T**(5.0/4.0)*EXP(B/T)
      RETURN
  201 WRITE(5,202) T
  202 FORMAT(1H1,'TEMPERATURE OUT OF RANGE IN ARND T IS',F10.1)
      ARND=1.0E13
      RETURN
      END
```

```
      FUNCTION ECEQ(T,N,WL)
C  THIS FUNCTION CALCULATES THE CONTINUUM
C  EMISSION IN WATTS/SR-CM**4 OF ARGON
C  AS A FUNCTION OF TEMPERATURE(T-DEG.K),
C  NUMBER DENSITY OF IONS OR ELECTRONS
C  WHICH ARE ASSUMMED EQUAL(N-CM**-3),
C  AND WAVELENGTH(WL-ANGSTROMS).
      REAL K,N,NF
      H=4.14E-15
      K=8.616E-5
      C=3.0E18
      V=C/WL
      U2=5.519
      X=EXP(-(H*V)/(K*T))
      Y=(6.0*GAUNT(WL))/(U2)
      NF=N/1.0E5
      Z=(NF**2)/(SQRT(T)*WL**2)
      ECEQ=(1.65E-09*Z)*(Y*(1.0-X)+X)
      RETURN
      END
```

```
      SUBROUTINE LSQ(X,Y,NORDR,NY,B,CC,C,PQ)
      DIMENSION X(NY),Y(NY),B(NY),CC(NY,NY),C(NY)
      INTEGER P,Q,PQ
      PQ=0
      M=NORDR+1
      DO 10 Q=1,M
      B(Q)=0.
      DO 15 I=1,NY
      B(Q)=B(Q)+Y(I)*X(I)**(Q-1)
   15 CONTINUE
      DO 20 P=1,M
      CC(P,Q)=0.
      DO 25 I=1,NY
      CC(P,Q)=CC(P,Q)+X(I)**(P+Q-2)
   25 CONTINUE
   20 CONTINUE
   10 CONTINUE
      DO 30 Q=1,M
      DO 35 P=1,M
      L=Q+(P-1)*M
      C(L)=CC(P,Q)
   35 CONTINUE
   30 CONTINUE
      CALL SIMQ(C,B,M,KS)
      IF(KS.EQ.1) PQ=2
      RETURN
      END
```

```
      SUBROUTINE COEFF(X,Y,NY,IFIT,NORDR,IPLOT,IR,RE,PQ,
     $ A,B,C,D,CC,XU,YU)
C
      DIMENSION X(NY),Y(NY)
      DIMENSION A(NY),B(NY),C(NY),D(NY)
      DIMENSION CC(NY,NY)
      DIMENSION XU(NY),YU(NY),RE(NY)
      INTEGER PQ
      DATA EPS/.01/
      GO TO 77
      ENTRY INTRP4(XI,YI,IFIT)
C
      GO TO (31,32),IFIT
C
   31 DO 20 I=1,NYP
      K=I
      IF(XI.LT.X(I+1)) GO TO 21
   20 CONTINUE
   21 YI =   A(K)*XI**3+B(K)*XI**2+C(K)*XI+D(K)
      RETURN
C
   32 YI=0.
      DO 34 J=1,MM
      YI=YI+B(J)*XI**(J-1)
   34 CONTINUE
      RETURN
C
C *** CALCULATE FITTING COEFFICIENTS ***
C
   77 IF(IPLOT.EQ.5 .OR. IPLOT.EQ.8) GO TO 500
      IF(IPLOT.EQ.7) GO TO 200
C
      GO TO (41,42),IFIT
C
   41 NYP=NY-1
```

```
      DO 10 K=1,NYP
C   COMPUTE CONSTANTS
      X0=X(K-1)
      XK=X(K)
      X1=X(K+1)
      X2=X(K+2)
      Y0=Y(K-1)
      YK=Y(K)
      Y1=Y(K+1)
      Y2=Y(K+2)
      X0S=X0*X0
      XKS=XK*XK
      X1S=X1*X1
      X2S=X2*X2
      X0C=X0S*X0
      XKC=XKS*XK
      X1C=X1S*X1
      X2C=X2S*X2
      XM0=XK-X0
      XM1=XK-X1
      XM2=XK-X2
      YM0=YK-Y0
      YM1=YK-Y1
      YM2=YK-Y2
      XM0S=XKS-X0S
      XM1S=XKS-X1S
      XM2S=XKS-X2S
      XM0C=XKC-X0C
      XM1C=XKC-X1C

      XM2C=XKC-X2C
      IF(K.EQ.1) GO TO 11
      IF(K.EQ.NYP) GO TO 12
```

```
C   FOR INTERNAL PANELS   (K=2,NYP-1)
      A(K)=   ( (YM0*XM1-YM1*XM0)*(XM0S*XM2-XM2S*XM0)
     1         -(YM0*XM2-YM2*XM0)*(XM0S*XM1-XM1S*XM0) )
     2      / ( (XM0C*XM1-XM1C*XM0)*(XM0S*XM2-XM2S*XM0)
     3         -(XM0C*XM2-XM2C*XM0)*(XM0S*XM1-XM1S*XM0) )
      B(K)=   ( (YM0*XM2-YM2*XM0)-A(K)*(XM0C*XM2-XM2C*XM0) )
     1      / (XM0S*XM2-XM2S*XM0)
      C(K)=   ( YM0-A(K)*XM0C-B(K)*XM0S ) / (XM0)
      D(K)=   YK - A(K)*XKC - B(K)*XKS - C(K)*XK
      GO TO 10
C   FOR LEFTMOST PANEL      (K=1)
   11 A(K)=0.
      B(K)=   (YM1*XM2-YM2*XM1) / (XM1S*XM2-XM2S*XM1)
      C(K)=   (YM1-B(K)*XM1S)/(XM1)
      D(K)=   YK-B(K)*XKS-C(K)*XK
      GO TO 10
C   FOR RIGHTMOST PANEL    (K=NYP)
   12 A(K)=0.
      B(K)=   (YM0*XM1-YM1*XM0) / (XM0S*XM1-XM1S*XM0)
      C(K)=   (YM0-B(K)*XM0S)/(XM0)
      D(K)=   YK-B(K)*XKS-C(K)*XK
   10 CONTINUE
      RETURN
C
   42 MM=NORDR+1
      RETURN
C
C   LEAST SQUARES WITH 1/REL.ERR. WEIGHTING
  200 L=0
      MM=NORDR+1
  207 RMAX=0.
      DO 201 I=1,NY
  201 RMAX=AMAX1(RMAX,RE(I))
  210 DO 202 I=1,NY
```

```
      IF(RE(I).LT.EPS) RE(I)=EPS
      NUM=AMIN1(10.,RMAX/RE(I)+EPS)
      IF(NUM.LE.0) GO TO 202
      DO 203 J=1,NUM
      L=L+1
      XU(L)=X(I)
      YU(L)=Y(I)
  203 CONTINUE
  202 CONTINUE
      IF(IPLOT.EQ.8) GO TO 520
      IF(L.LE.30) GO TO 205
      RMAX=RMAX/1.4
      WRITE(6,299) L
  299 FORMAT(21H WIDE WEIGHTING RANGE,I5,14H    WTS REDUCED)
      L=0
      GO TO 210
  205 CALL LSQ(XU,YU,NORDR,L,B,CC,C,PQ)
      RETURN
C
C  LEAST SQUARES FIT TO HISTOGRAM DATA
C    WITH OR WITHOUT 1/REL.ERR. WEIGHTING
  500 MM=NORDR+1
      R=IR
      IF(IPLOT.EQ.8) GO TO 207
  520 LX=0
      NBR=0
      DO 1701 J=1,MM
      B(J)=0.
      DO 1711 I=1,NY
      NUM=1
      IF(IPLOT.EQ.8) NUM=AMIN1(10.,RMAX/RE(I)+EPS)
      IF(NUM.LE.0) GO TO 1711
      DO 503 LM=1,NUM
      B(J)=B(J)+((R+1.)*(X(I+1)**(J+IR)-X(I)**(J+IR))*Y(I))
     1       /((FLOAT(J)+R)*(X(I+1)**(IR+1)-X(I)**(IR+1)))
```

```
  503 CONTINUE
 1711 CONTINUE
      DO 1702 K=1,MM
      CC(J,K)=0.
      DO 1712 L=1,NY
      NUM=1
      IF(IPLOT.EQ.8) NUM=AMIN1(10.,RMAX/RE(I)+EPS)
      IF(NUM.LE.0) GO TO 1712
      DO 510 LM=1,NUM
      CC(J,K)=CC(J,K)+   ( (R+1.)**2*(X(I+1)**(J+IR)-X(I)**(J+IR))
     1              *(X(I+1)**(K+IR)-X(I)**(K+IR)) )
     2        / (  (FLOAT(J)+R)*(FLOAT(K)+R)*(X(I+1)**(IR+1)
     3              -X(I)**(IR+1))**2 )
  510 CONTINUE
 1712 CONTINUE
      NBR=NBR+NUM
      LX=J+(K-1)*MM
      C(LX)=CC(J,K)
 1702 CONTINUE
 1701 CONTINUE
      IF(NBR.LE.225) GO TO 1111
      RMAX=RMAX/1.4
      WRITE(6,299) NBR
      GO TO 520
C
 1111 CALL SIMQ(C,B,MM,IT)
      IF(IT.EQ.1) GO TO 999
      PQ=2
      WRITE(6,47)
   47 FORMAT( 24H *** SINGULAR MATRIX *** )
 9999 RETURN 0
  999 RETURN
      END
```

```
      SUBROUTINE SIMQ(A,B,N,KS)
      DIMENSION  A(1), B(1)
C         A - MATRIX OF COEFFICIENTS STORES THE ROWS OF AN NXN MATRIX
C             IN ONE COLUMN. THE N ELEMENTS OF THE FIRST ROW FORM THE
C             FIRST N ELEMENTS OF THE A MATRIX8 THE SECOND ROW FORMS
C             THE NEXT N ELEMENTS OF A ECT.
C         A - MATRIX OF COEFFICIENTS STORED COLUMNWISE. THESE ARE
C             DESTROYED IN THE COMPUTATION.  THE SIZE OF MATRIX A IS
C             N BY N.
C         B - VECTOR OF ORIGINAL CONSTANTS (LENGTH N).  THESE ARE
C             REPLACED BY FINAL SOLUTION VALUES, VECTOR X.
C         N - NUMBER OF EQUATIONS AND VARIABLES.
C         KS - OUTPUT DIGIT,
C              0 FOR A NORMAL SOLUTION,
C              1 FOR A SINGULAR SET OF EQUATIONS.
      TOL=0.0
      KS=0
      JJ=-N
      DO 65 J=1,N
      JY=J+1
      JJ=JJ+N+1
      BIGA=0.
      IT=JJ-J
      DO 30 I=J,N
      IJ=IT+I
      IF ( ABS(BIGA) -  ABS(A(IJ))) 20,30,20
   20 BIGA=A(IJ)
      IMAX=I
   30 CONTINUE
      IF ( ABS(BIGA) - TOL) 35,35,40
   35 KS=1
      RETURN
   40 I1=J+N*(J-2)
      IT=IMAX-J
```

```
        DO 50 K=J,N
        I1=I1+N
        I2=I1+IT
        SAVE=A(I1)
        A(I1)=A(I2)
        A(I2)=SAVE
  50    A(I1)=A(I1)/BIGA
        SAVE=B(IMAX)
        B(IMAX)=B(J)
        B(J)=SAVE/BIGA
        IF(J-N)55,70,55
  55    IQS=N*(J-1)
        DO 65 IX=JY,N
        IXJ=IQS+IX
        IT=J-IX
        DO 60 JX=JY,N
        IXJX=N*(JX-1)+IX
        JJX=IXJX+IT
  60    A(IXJX)=A(IXJX)-(A(IXJ)*A(JJX))
  65    B(IX)=B(IX)-(B(J)*A(IXJ))
  70    NY=N-1
        IT=N*N
        DO 80 J=1,NY
        IA=IT-J
        IB=N-J
        IC=N
        DO 80 K=1,J
        B(IB)=B(IB)-A(IA)*B(IC)
        IA=IA-N
  80    IC=IC-1
        RETURN
        END
```

BIBLIOGRAPHY

1. W. Hittorf, "Uber die Elektrizitaets-leitung der Gase," <u>Ann. Physik</u> <u>21</u>, 90-139 (1884).

2. G. I. Babat, "Electrodeless Discharges and Some Allied Problems," <u>J. Inst. Elec. Engrs. (London)</u> <u>94</u>, 27-37 (1947).

3. T. B. Reed, "Induction Coupled Plasma Torch," <u>J. Appl. Phys.</u> <u>32</u>, 821-824 (1961).

4. V. M. Goldfarb and S. V. Dresvin, "Optical Investigation of the Distribution of Temperature and Electron Density in an Argon Plasma," <u>Taplofiz. Vys. Temp.</u> <u>3</u>, 333-339 (1965).

5. P. D. Scholz and T. D. Anderson, "Local Thermodynamic Equilibrium in an RF Argon Plasma," <u>J. Quant. Spectrosc. Radiat. Trans.</u> <u>8</u>, 1411-1418 (1968).

6. R. E. Rovinskii, V. A. Gruzdev, T. M. Gutenmakher, and A. P. Sobolev, "Determination of Temperature in a Stationary High Frequency Induction Discharge," <u>Teplofiz. Vys. Temp.</u> <u>5</u>, 557-561 (1967).

7. H. W. Eckert, "The Induction Arc; A State-of-the Art Review," Aerospace Corp. TR-0073(3220-20)-2, Air Force SAMSO-TR-72-227 (1972).

8. A. D. Stokes, "Electrical Conduction and Radiant Heat Transfer in Induction Heating," Paper presented Interntl. Conf. on Gas Discharges, London, September 1970, <u>IEEE Publ.</u> No. 70, p 182.

9. H. W. Eckert, "Analytical Treatment of Radiation and Conduction Losses in Thermal Induction Plasmas," <u>J. Appl. Phys.</u> <u>41</u>, 1529-1537 (1970).

10. H. W. Eckert, "Analysis of Thermal Induction Plasmas Between Coaxial Cylinders," <u>J. Appl. Phys.</u> 43, 46-52 (1972).

11. D. C. Pridmore-Brown, "A Numerical Study of the Inductive Electrodeless Discharge," <u>J. Appl. Phys.</u> <u>41</u>, 3621-3625 (1970).

12. H. W. Eckert and D C. Pridmore-Brown, "Temperature Profiles in Argon Induction Plasmas: Theory and Experiment," <u>J. Appl. Phys.</u> <u>42</u>, 5051-5054 (1971).

BIBLIOGRAPHY (Continued)

13. H. Maecker, "Uber die Charkteristiken Zylindrischer Bogen," Z. Physik. 157, 1 (1959).

14. H. Maecker, "Messung und Auswertung von Bogencharakteristiken (Ar, N_2)," Z. Physik. 158, 392 (1960).

15. E. H. Holt and R. E. Haskell, Foundations of Plasma Dynamics, Macmillan Company, New York, 1965.

16. G. H. Brown, C. N. Hoyerland, and R. A. Bierworth, Theory and Application of Radio-Frequency Heating, D. Van Nostrand Company, New York, 1967.

17. M. P. Freeman and J. D. Chase, "Energy-Transfer Mechanism and Typical Operating Characteristics for the Thermal RF Plasma Generator," J. Appl. Phys. 39, 180-190 (1968).

18. H. W. Eckert, "Analysis of Thermal Induction Plasmas Dominated by Radial Convection Losses," J. Appl. Phys. 41, 1520-1528 (1970).

19. R. E. Rovinskii and A. P. Sobolev, "Calculation of the Parameters of an Induced High-Frequency, High Pressure Discharge," Teplofiz. Vys. Temp. 7, 203, 207 (1969).

20. V. A. Gruzdev, R. E. Rovinskii, and A. P. Sobolev, "An Approximate Solution for the Steady-State, Inductive-Type, High Frequency Discharge in a Closed Volume," Zh. Prikl. Mech. Tekh. Fiz. 1, 143-150 (1967).

21. R. C. Miller and R. J. Ayen, "Temperature Profiles and Energy Balances for an Inductively Coupled Plasma Torch," J. Appl. Phys. 40, 5260-5273 (1969).

22. J. D. Chase, "Magnetic Pinch Effect in the Thermal RF Induction Plasma," J. Appl. Phys. 40, 318-325 (1969).

23. J. D. Chase, "Theoretical and Experimental Investigation of Pressure and Flow in Induction Plasma," J. Appl. Phys. 42, 4870-4879 (1971).

24. D. Keefer, University of Florida, Gainesville, Florida, private communications.

25. J. Sprouse, Arnold Research Organization, Arnold Air Force Base, Tullahoma, Tennessee, private communications.

26. H. W. Eckert, "Measurement of the Magnetic Field Distribution in a Thermal Induction Plasma," J. Appl. Phys. 42, 3108-3113 (1971).

BIBLIOGRAPHY (Continued)

27. R. S. Devoto, "Transport Coefficients of High Pressure Argon in a
     Magnetic Field," Aerospace Research Laboratories Tech. Report
     ARL 71-0075, April, 1971.

28. J. M. Yos, "Transport Coefficients of Argon," AVCO/RAD Tech. Report
     RAD-TR-65-7, 1965.

29. G. L. Cann, "Theoretical Calculations of Argon Transport Coeffi-
     cients," Guggenheim Aeronautical Laboratory Tech. Memo. 61 (1961).

30. A. B. Cambel, Plasma Physics and Magnetofluidmechanics, McGraw-
     Hill Book Company, Inc., New York, 1963.

31. H. W. Emmons, "Arc Measurement of High-Temperature Gas Transport
     Properties," Phys. Fluids 10, 1125-1136 (1967).

32. S. C. Lin, E. L. Resler, and A. Kantrowitz, "Electrical Conductivity
     of Highly Ionized Argon Produced by Shock Waves," J. Appl. Phys. 26,
     95-109 (1955).

33. J. Lau, "Electrical Conductivity of Inter Gases-Seed Combination in
     Shock Tubes," Can. J. Phys. 42, 154B (1964).

34. H. W. Drawin and P. Felenbok, Data for Plasmas in Local Thermody-
     namics Equilibrium, Gauthier-Villars, Paris, 1965.

35. H. N. Olsen, "The Electric Arc as a Light Source for Quantitative
     Spectroscopy," Quant. Spectrosc. Radiat. Transfer 3, 305-333 (1963).

36. D. D. Laun, "Second Spectrum of Tungsten (W II)," J. Research NBS
     68A (1964).

37. R. J. Rosa, Magnetohydrodynamic Energy Conversion, McGraw-Hill Book
     Company, Inc., New York, 1968.

38. L. P. Kudrin, "Estimation of the Conductivity of a Low Temperature
     (UF) Plasma of High Density," Sov. Atomic Energy 22, 332-338 (1967).

39. I. Amdur and E. A. Mason, "Properties of Gases at Very High Temper-
     atures," Phys. Fluids 1, 370-380 (1958).

40. C. F. Knopp and A. B. Cambel, "Experimental Determination of the
     Thermal Conductivity of Atmospheric Argon Plasma," Phys. Fluids 9,
     989-997 (1966).

41. K. P. Horn, H. Wong, and D. Bershader, "Radiative Behavior of Shock
     Heated Argon Plasma Flows," J. Plasma Physics 1, 157-170 (1967).

BIBLIOGRAPHY (Continued)

42. A. D. Stokes, "Electrical Conduction and Radiant Heat Transfer in Induction Discharges," International Conference on Gas Discharges, London 1970, IEEE Publication No. 70, 182-186.

43. D. L. Evans and R. S. Tankin, "Experimental Measurement of the Emission and Absorption of Radiation by an Argon Plasma," ARL 67-0157, July, 1967.

44. P. W. Schreiber, A. M. Hunter, II, and K. R. Benedetto, "Total Radiation Source Strength of Argon Plasmas," ARL-70-0137, 21-48, August, 1970.

45. H. E. Petschek, P. H. Rose, H. S. Glick, A. Kane, and A. Kantrowitz, "Spectroscopic Studies of Highly Ionized Argon Produced by Shock Waves," J. Appl. Phys. 26, 83 (1955).

46. P. J. Marteney, A. E. Mensing, and N. L. Krassella, "Experimental Investigation of the Spectral Emission Characteristics of Argon-Tungsten and Argon-Uranium Induction Heated Plasmas," United Aircraft Research Laboratories Report No. 9-910092-11, 1968.

47. H. W. Eckert, "A Dual Magnetic Probe System for Phase Measurements in Thermal Induction Plasmas," J. Appl. Phys. 43, 2707-2713 (1972).

48. E. S. Trekhov, A. F. Fomenko, and Yu. M. Koshev, "Parameters of Stationary Inductive Discharges at Atmospheric Pressures," Teplofiz. Vys. Temp. 7, 860-865 (1969).

49. R. A. Benns, "Generation of Induction Heated, Seeded Hydrogen Plasmas at One Atmosphere Pressure," Ph.D. Thesis, Georgia Institute of Technology, August, 1972.

50. L. Tonks and I. Langmuir, "Theory of the Arc Plasma," Phys. Rev. 34, 876 (1929).

51. M. A. Heald and C. B. Wharton, Plasma Diagnostics with Microwaves, John Wiley and Sons, Inc., New York, 1965.

52. B. S. Malone and W. H. Corcoran, "Transition Probability Measurements in the Blue-Near U.V. Spectrum of Argon I," J. Quant. Spectrosc. Radiat. Transfer 6, 443-449 (1966).

53. B. D. Adcock and W. E. G. Plumtree, "On Excitation Temperature Measurements in a Plasma-Jet, and Transition Probabilities for Argon Lines," J. Quant. Spectrosc. Radiat. Transfer 4, 29-39 (1964).

54. H. N. Olsen, "Measurement of Argon Transition Probabilities Using the Thermal Arc Plasma as a Radiation Source," J. Quant. Spectrosc. Radiat. Transfer 3, 59-76 (1963).

BIBLIOGRAPHY (Continued)

55. H. A. Kramers, "On the Theory of X-Ray Absorption and of the Con-
     tinuous X-Ray Spectrum," Phil. Mag. J. Sci.-Suppl. 6 46, 836-871
     (1923).

56. W. J. Karzas and R. Latter, "Electron Radiative Transitions in a
     Coulomb Field," Astrophys. J. Suppl. 6, 55, 167-212 (1961).

57. A. Unsold, "Uber das kontinuierliche Spektrum der Hg-Hochdrucklampe,
     des Unterwasserfunkens und ahnlicher Gasentladunger," Ann. Phys.
     Lpz. Suppl. 5 33, 607 (1938).

58. L. M. Biberman and G. E. Norman, "On the Calculation of Photoioniz-
     ation Absorption," Opt. Spectry. 8, 230-232 (1960).

59. L. M. Biberman, G. E. Norman, and K. N.Ulyanov, "On the Calculation
     of Photoionization Absorption in Atomic Gases," Opt. Spectry. 10,
     297-299 (1961)

60. W. Bander, "Radiation from High Pressure Plasmas," J. Appl. Phys.
     39, 148-152 (1968).

61. D. Schluter, "Der kontinuierliche Absorptionskoeffizient des Argons,"
     Z. Astrophysik. 56, 43-52 (1962).

62. D. Schluter, "Die Berechnung der Ubergangswahrscheinlichkeiten von
     Seriengrenzkontinua mit Anwendung auf die schweren Edelgase,"
     Z. Astrophysik. 61, 67-76 (1965).

63. H. R. Griem, Plasma Spectroscopy, McGraw-Hill Book Co., New York,
     1964.

64. J. B. Shumaker and C. H. Popense, "A Study of Equilibrium in Argon
     Arcs," J. of Research of the NBS-A Phys. and Chem. 76A, 71-76 (1972).

65. H. N. Olsen, "The Electric Arc as a Light Source for Quantitative
     Spectroscopy," Quant. Spectrosc. Radiat. Transfer 3, 305-333 (1963).